

# Iridium Communications Satellite Constellation Data for Study of Earth's Magnetic Field

Brian Anderson<sup>1</sup>, Regupathi Angappan<sup>2</sup>, Ankit Barik<sup>2</sup>, Sarah K Vines<sup>1</sup>, Sabine Stanley<sup>2</sup>, Pietro N Bernasconi<sup>1</sup>, Haje Korth<sup>1</sup>, and Robin J Barnes<sup>1</sup>

<sup>1</sup>The Johns Hopkins University Applied Physics Laboratory

<sup>2</sup>The Johns Hopkins University

November 23, 2022

## Abstract

Characterization of Earth's magnetic field is key to understanding the dynamics of core flows and the dynamo. Satellite measurements of the magnetic field normally use precise magnetometers on a few spacecraft to acquire data over the entire globe over periods of months to years. The advent of commercial satellite constellations of tens to hundreds of satellites may offer complementary observations, even with low-precision magnetometers, providing rapid global coverage. Here we assess whether the magnetic field data from the Iridium Communications constellation of 66 low Earth orbiting satellites can be used to determine the geometry of Earth's main field. The Iridium satellites are in near polar, 86° inclination, 780 km altitude, circular orbits, with 11 satellites in each of six orbit planes evenly spaced in longitude. We use data from the first-generation Iridium satellites, launched in the late 1990s, and acquired for scientific analysis beginning in January 2010. Although digitized with 30 nT resolution, the uncertainties in the data are random errors so that the statistics of 300,000 samples/day allow determination of the average magnetic field in 9° latitude by 9° longitude bins to about 3 nT. The data reduction, inter-calibration, quiet interval selection, and uncertainty assessment are described. Time series of spherical harmonic coefficients are used to identify artifacts and derive maps of corrected residuals at the average Iridium orbit altitude. From 2010 to 2015 the evolution of the field agrees on average between Iridium and the CHAOS 7.4 model to within 30 nT standard deviation, or  $\sim 5$  nT/yr.

1 **Iridium Communications Satellite Constellation Data for Study of Earth's Magnetic Field**

2

3 Brian J. Anderson<sup>1</sup>, Regupathi Angappan<sup>2</sup>, Ankit Barik<sup>2</sup>, Sarah K. Vines<sup>1</sup>, Sabine Stanley<sup>2</sup>,

4 Pietro N. Bernasconi<sup>1</sup>, Haje Korth<sup>1</sup>, and Robin J. Barnes<sup>1</sup>

5

6 1. The Johns Hopkins University Applied Physics Laboratory, Laurel, MD.

7 2. Department of Earth and Planetary Sciences, The Johns Hopkins University, Baltimore, MD.

8

9

10 Submitted to *Geochemistry, Geophysics, Geosystems (G3)* 4 November 2020

11 Revised: 14 April 2021

12 **Key points**

13 Iridium satellite avionics magnetometers provide global coverage in measurement of Earth's  
14 magnetic field.

15 Coverage from 86° S to 86° N latitude with ~2° longitude/latitude resolution is achieved in two  
16 hours.

17 Uncertainties as low as 3 nT in the global mapped fields are achieved for each of 262  
18 geomagnetically quiet days from 2010 through 2015.

19

20 **Abstract**

21 Characterization of Earth's magnetic field is key to understanding the dynamics of core flows  
22 and the dynamo. Satellite measurements of the magnetic field normally use precise  
23 magnetometers on a few spacecraft to acquire data over the entire globe over periods of months  
24 to years. The advent of commercial satellite constellations of tens to hundreds of satellites may  
25 offer complementary observations, even with low-precision magnetometers, providing rapid  
26 global coverage. Here we assess whether the magnetic field data from the Iridium  
27 Communications constellation of 66 low Earth orbiting satellites can be used to determine the  
28 geometry of Earth's main field. The Iridium satellites are in near polar,  $86^\circ$  inclination, 780 km  
29 altitude, circular orbits, with 11 satellites in each of six orbit planes evenly spaced in longitude.  
30 We use data from the first-generation Iridium satellites, launched in the late 1990s, and acquired  
31 for scientific analysis beginning in January 2010. Although digitized with 30 nT resolution, the  
32 uncertainties in the data are random errors so that the statistics of 300,000 samples/day allow  
33 determination of the average magnetic field in  $9^\circ$  latitude by  $9^\circ$  longitude bins to about 3 nT. The  
34 data reduction, inter-calibration, quiet interval selection, and uncertainty assessment are  
35 described. Time series of spherical harmonic coefficients are used to identify artifacts and derive  
36 maps of corrected residuals at the average Iridium orbit altitude. From 2010 to 2015 the  
37 evolution of the field agrees on average between Iridium and the CHAOS 7.4 model to within 30  
38 nT standard deviation, or  $\sim 5$  nT/yr.

39

40 **Plain Language Summary**

41 The shape of Earth’s magnetic field is used for navigation, resource exploration, and space  
42 hazard predictions. Changes in the field provide clues to motions of the molten iron core 1800  
43 miles (~3000 km) deep. In recent years the magnetic poles have moved rapidly, making it  
44 especially important to track the field. Advances in satellite and launch technologies have  
45 enabled launches of satellites in greater numbers than ever before to near-Earth space. The 66  
46 Iridium Communications satellites, launched originally in the late 1990s and recently replaced  
47 with the Iridium NEXT constellation, have operated continuously since 1997 and are planned to  
48 continue to 2030 or beyond. Each original and NEXT Iridium satellite is equipped with a  
49 magnetometer as part of the satellite systems. We developed techniques to analyze magnetic  
50 field data from these satellites to detect small changes in Earth’s magnetic field. The large  
51 number of Iridium satellites and their orbits allow global coverage of Earth in as little as two  
52 hours and we show that these data can be used to track changes in Earth’s magnetic field more  
53 than ten times faster than ever before. This offers numerous practical and scientific benefits to  
54 understand the interior workings of our home planet.

55

- 56 **Index Terms** (up to five):  
57 All from 1500 GEOMAGNETISM AND PALEOMAGNETISM  
58 1541 Satellite magnetics: main field, crustal field, external field  
59 1545 Spatial variations: all harmonics and anomalies  
60 1555 Time variations: diurnal to decadal  
61 1594 Instruments and techniques  
62
- 63 **Keywords** (up to six): Geomagnetism, Iridium Communications Inc., satellite constellation,  
64 space magnetometry, geodynamo, magnetic field  
65

## 66 **1. Introduction**

67           The magnetic field of the Earth yields clues to the dynamics of the present-day core  
68 dynamo and its history through magnetization in the crust (cf. *Aubert et al.*, 2010). The internally  
69 generated magnetic field of the Earth arises predominantly from the dynamo in the outer core,  
70 and the structure and intensity of the field above the core is given by a potential field  
71 extrapolated from the core-mantle boundary (CMB) ~3000 km below the surface (cf. *Roberts*  
72 *and King*, 2013). The dynamo field typically varies by ~1% per decade and includes wave-like  
73 features at middle-to-low latitudes extending and propagating in longitude (cf. *Finlay et al.*,  
74 2010a). Sub-annual variations have also been observed and identified as geomagnetic jerks that  
75 exhibit rapid changes in the first and second time derivatives in the secular variation at a fixed  
76 observatory (*Mandea et al.*, 2010; *Brown et al.*, 2013; *Finlay et al.*, 2016). While the mantle is  
77 not a dominant source of magnetic field, induction of currents in the mantle on time scales of  
78 hours to days in response to correspondingly abrupt changes in the external magnetospheric  
79 currents (e.g. magnetopause and ring currents) may be present, though this has not yet been  
80 extensively documented (*Civet et al.*, 2015). Crustal fields are ‘permanent’ on geologic time  
81 scales shorter than crustal formation and circulation (tectonic) and are useful as magnetic imprint  
82 markers. These crustal fields are best resolved in satellite observations at the lowest attainable  
83 orbit altitudes (~300 to 400 km) as the depth is comparatively shallow (<10 km) and the  
84 horizontal length scales are small (1 to 500 km).

85           Precise characterization of the main magnetic field, actively generated internally by the  
86 dynamo together with contributions from remanent magnetization of the crust, is important for  
87 many government, commercial, and scientific users (cf. *Mandea and Purucker*, 2018) motivating  
88 continuous maintenance of the World Magnetic Model (WMM) by the National Centers for

89 Environmental Information (NCEI) (*Chulliat et al., 2020*). The interaction of the magnetized  
90 solar wind with the Earth's magnetic field produces various current systems and the resulting  
91 magnetic signals on the ground and at satellites in low-Earth orbit (LEO, cf. *Milan et al., 2017*)  
92 must be considered for precise study of the internally generated field (cf. *Baumjohann and*  
93 *Nakamura 2009; Raeder et al., 2017; Olson and Stolle, 2017*). In addition, the dynamical  
94 interaction of neutral thermospheric winds with plasma populations in the ionosphere drives  
95 currents, and hence magnetic fields, that must be considered in analyses of ground and LEO  
96 magnetometer observations (e.g., *Yamazaki and Maute, 2017*). The range of spatial distributions  
97 and temporal variations of external sources complicates studies of the main field and makes  
98 precise characterization of the global field a challenging inversion problem (cf. *Sabaka et al.,*  
99 *2018*).

100 Variations in the magnetic field of the Earth arise from changes in the fluid outer core (cf.  
101 *Hulot et al., 2010b*). Recently the magnetic pole motions have accelerated such that linear  
102 extrapolation for the field secular variation is not sufficient to meet operation requirements for  
103 main field models and intermediate model releases have been necessary (cf. *Mandea and*  
104 *Purucker, 2018; Witze, 2019*). Scientific interest in sub-decadal time scales of main field  
105 variations is growing as well. Processes occurring at these time scales relate to the nature and  
106 characteristics of geomagnetic jerks, their spatial scales, global distribution, and prevalence to  
107 inform and constrain the core fluid dynamics from which they arise (*Bloxham et al., 2002;*  
108 *Mandea et al., 2010; Brown et al., 2013*). Similarly, waves in the magnetic field have also been  
109 inferred (*Hori et al., 2015; Buffet et al., 2016; Aubert and Finlay, 2019*) and diagnosing the  
110 wavelengths and group speeds are key to determining their origins. There is therefore

111 considerable practical and fundamental scientific interest in augmenting present capabilities to  
112 measure Earth's field on sub-decadal and even sub-annual time scales.

113         To date the most accurate and reliable results for the main field have been obtained using  
114 combinations of data from globally distributed ground magnetic observatories and precision  
115 magnetic field measurements from satellites in LEO. The first precise LEO magnetic mapping  
116 mission was MAGSAT, conducted in 1979 and 1980 (*Langel et al.*, 1982). After a hiatus of  
117 nearly two decades, this was followed by missions using precise magnetic mapping  
118 instrumentation including the Oersted satellite launched in early 1999, the CHAMP satellite  
119 launched in July of 2000, and SAC-C launched in November 2000 (cf. *Olsen et al.*, 2010). Most  
120 recently the set of three Swarm satellites were launched in November 2013 (*Olsen et al.*, 2013).  
121 The Swarm mission conducts multi-point precision magnetic field mapping, and they remain  
122 operational with an expected lifetime to at least 2024. Recent derivations of the main field from  
123 Swarm yield high-resolution maps of the crustal field and magnetic potential representations of  
124 the core field, and can resolve time scales as short as about six months (*Finlay et al.*, 2016).

125         The central challenge of precise global magnetic mapping from LEO is that the satellite  
126 observations are obtained along one or two orbital planes in inertial space. Separating internal,  
127 ionospheric, and magnetospheric induction sources requires accounting for each of these  
128 contributions. Because of orbital precession, polar LEO orbits span all local times in  
129 approximately six months depending on the precise inclination. This coverage makes global  
130 mapping somewhat challenging for time scales shorter than about six months without convolving  
131 local time period signals with seasonal variations. Notwithstanding these challenges, powerful  
132 inversion techniques have been developed to simultaneously account for all of these

133 contributions (cf. *Sabaka et al.*, 2018). These state-of-the-art techniques have yielded remarkable  
134 advances including unprecedented characterization of the ocean induction fields.

135         Nonetheless, the inversions remain under-determined and are subject to substantial  
136 covariance among the large number of parameters ( $>10,000$ ) used in the fits. Such inversions  
137 always benefit from additional observations and it is therefore of interest to explore avenues to  
138 augment the available database. The development and launches of commercial satellite  
139 constellations into LEO for communications began in the late 1990s and offer an opportunity for  
140 unprecedented orbital coverage over the Earth. While these constellations were not designed to  
141 support science-grade magnetic field measurements, the satellites in these constellations that  
142 carry commercial magnetometers may still offer real benefit for Earth's main field science. In  
143 this paper, we consider whether magnetic field data acquired from the Iridium Communications  
144 satellite constellation might provide another set of observational constraints for main field  
145 characterization. This constellation consists of 66 satellites in the communication network and  
146 additional on-orbit spares, all in near polar ( $86^\circ$  inclination), 780 km altitude orbits. The Iridium  
147 Communications satellites launched in 1997-1998 (Block 1) and replaced by the Iridium NEXT  
148 constellation (2017-2019) carry engineering magnetometers to support satellite operations.  
149 Moreover, the Iridium orbits are distributed over six orbit planes, 11 satellites in each plane,  
150 spaced evenly in longitude by  $30^\circ$ . Thus, the constellation provides dense global coverage of all  
151 latitudes and longitudes in as short a time as two hours.

152         Magnetometer data from the Block 1 Iridium satellites were first used for science  
153 analysis to study the Birkeland field-aligned currents which generate magnetic signals above the  
154 ionosphere as great as  $\sim 2000$  nT (*Anderson et al.*, 2000; *Waters et al.*, 2001) and more recently  
155 for the Active Magnetosphere and Planetary Electrodynamics Response Experiment (AMPERE)

156 under which the data transmission to the ground was increased 10 to 100-fold to allow  
157 measurement of the large-scale Birkeland currents every ten minutes (*Clausen et al.*, 2012;  
158 *Anderson et al.*, 2014; *Waters et al.*, 2020).

159 Although the data from the body-mounted Iridium magnetometers are of substantially  
160 lower quality than acquired from precision instruments, non-science magnetometer data can be  
161 calibrated using orbital data to contribute to Earth main field studies (cf. *Alken et al.*, 2020). For  
162 satellite constellations in particular, the continuous global coverage of all local times and number  
163 of observations warrants an assessment of the potential utility of these data for the  
164 characterization of Earth's magnetic field. The comparatively high altitude and low resolution  
165 imply that the data are unlikely to contribute to understanding of the crustal field, but the crustal  
166 field has been found to be largely static and has been extensively analyzed (cf. *Langlais et al.*,  
167 2010; *Olsen et al.*, 2017). The Iridium data therefore are most applicable for specifying the  
168 external field and in studies of the dynamics of the field originating from the core. Motivated by  
169 the prospects for such unprecedented global coverage in magnetic field observations, we use  
170 magnetic field data from the Iridium Communications constellation originally acquired and  
171 processed for AMPERE to assess whether useful, independent information on Earth's main field  
172 can be extracted. The AMPERE data from Block 1 give one sample every 19.44 seconds ( $\sim 1.2^\circ$   
173 along track spacing) and the constellation's configuration achieves global sampling with  $\sim 2.25^\circ$   
174 longitude separation mapping the globe every two hours.

175 In this paper, we present an initial analysis and data reduction of the Block 1, original,  
176 Iridium magnetometer data from January 2010 through November 2015 to identify artifacts and  
177 erroneous signals in the data and to quantify the characteristics of the core field that might be  
178 resolved using these observations. **Section 2** provides a detailed description of the magnetic field

179 data and processing developed for AMPERE, as well as the modification of the standard  
180 AMPERE data processing for main field studies. **Section 3** discusses the selection of  
181 geomagnetically quiet intervals for analysis. **Section 4** presents the analysis of these data for  
182 Earth's field together with initial global maps. Detailed analyses yielding time series of spherical  
183 harmonics for January 2010 through November 2015 are given in **Section 5**. The results are  
184 summarized and opportunities for applications are discussed in **Section 6**.

185

## 186 **2. Opportunity of Iridium Magnetic Field Observations**

187         The satellites constituting the Iridium Communications network are illustrated in **Figure**  
188 **1**. The 66 satellites in Iridium network orbits are distributed over six orbit planes, with 11  
189 satellites in each plane. The orbit planes are evenly spaced in longitude by  $30^\circ$  and the satellites  
190 within each plane are also evenly spaced along the orbit track, corresponding to 9-minute ( $33^\circ$   
191 orbit angle) separations in  $\sim 100$ -minute period orbits. Additional satellites in each orbit plane  
192 serve as on-orbit spares.

193         The first generation of Iridium satellites, denoted as Block 1, were launched starting in  
194 1997 and continued to operate until 2019, after launch of the constellation of Iridium NEXT  
195 satellites was completed. The avionics systems of both the Block 1 and NEXT Iridium satellites  
196 include a vector magnetometer. Each of the Block 1 Iridium satellites carried an Ithaco IM-103  
197 vector fluxgate magnetometer as part of the attitude control system. The magnetometers had  
198 intrinsic noise below  $0.1 \text{ nT}/\sqrt{\text{Hz}}$  at 1 Hz, absolute accuracy of 0.5% of full scale, and linearity to  
199 1 part in  $10^4$ . They were read out every 90 ms with 30-nT digitization onboard for closed-loop  
200 attitude control. The flight software system was initially configured only to support downlink  
201 rates for engineering monitoring,  $\sim 200$  s between samples corresponding to  $\sim 12^\circ$  in latitude.

202           Although the Iridium avionics magnetometers have digitization, sampling cadence, and  
203 performance substantially coarser than typical science instrumentation (cf. *Acuna et al.*, 2002),  
204 they provide resolution sufficient to detect signals of Earth’s Birkeland currents that are typically  
205 ~300 nT and up to 2000 nT, with a signal to noise ratio of about 10 (*Anderson et al.*, 2000). It is  
206 worth noting that the original detection and studies of Earth’s Birkeland currents were conducted  
207 using the attitude magnetometer on the Triad satellite (cf. *Iijima and Potemra*, 1976), so the  
208 application of utility magnetometers for science has been well demonstrated. However, the  
209 coverage afforded by the Iridium Communications constellation enables a dramatic advance in  
210 understanding the dynamics of Birkeland currents.

211           To take advantage of the global-scale, continuous coverage provided by the Iridium  
212 constellation configuration, the AMPERE dataset was developed (*Anderson et al.*, 2000; 2014;  
213 *Waters et al.*, 2001). This required new flight software to be implemented on the Iridium Block 1  
214 satellites to downlink magnetic field samples at 19.44 s (standard rate) or 2.16 s (high rate)  
215 intervals from every satellite in the communications network. Test data were acquired starting in  
216 October 2009, and complete AMPERE data were collected beginning 1 January 2010 and have  
217 continued to the present.

218           Processing to produce AMPERE data was developed to ingest, merge, and correct  
219 magnetometer data and attitude estimates from each individual satellite to yield time series and  
220 gridded maps of de-trended, inter-calibrated magnetic field perturbations reflecting signatures of  
221 field-aligned, Birkeland, currents flowing between the ionosphere and magnetosphere (cf.  
222 *Waters et al.*, 2020 for details on inversion techniques for AMPERE). Available AMPERE data  
223 spans January 2010 through September 2017. The NEXT magnetometer data are being calibrated

224 and processing for science products is in process. The present analysis uses AMPERE data from  
225 the Iridium Block 1 satellites from 2010 through 2015.

226         The global coverage of the magnetic field observations from the Iridium  
227 Communications constellation is dramatically different from prior LEO observations of Earth's  
228 magnetic field (cf. *Olsen et al.*, 2010, 2013). In the nine minutes between successive Iridium  
229 satellite passage over a given geographic latitude, the Earth rotates  $2.3^\circ$ . In two hours, the Earth  
230 rotates  $30^\circ$ , so that all longitudes pass under one of the Iridium constellation orbit planes. The  
231 sampling interval of 19.44 s corresponds to an along track distance of  $1.16^\circ$  around the orbit,  
232 corresponding to the approximate maximum latitude spacing in the near-polar orbits at the  
233 equator. Thus, in as little as two hours the observations blanket the Earth with magnetic field  
234 samples spaced by  $2.3^\circ$  in longitude and  $1.2^\circ$  in latitude between  $86.4^\circ$  S and  $86.4^\circ$  N. This  
235 coverage also spans all local times with 2-hour spacing so that the external current sources are  
236 simultaneously tracked and their effects effectively averaged in local time at every geographic  
237 longitude over one day.

238         The motivation to increase the magnetic field data returned from the Iridium satellites  
239 was to track and study the dynamics of Birkeland currents reflecting the solar wind-  
240 magnetosphere interaction (cf. *Milan et al.*, 2017; *Coxon et al.*, 2018). During development of  
241 AMPERE science data processing, discrepancies between geographically registered magnetic  
242 field data and the IGRF-11 main field model (*Finlay et al.*, 2010b) were noted but not analyzed  
243 in detail since the objective for AMPERE was to remove main field signals to extract the  
244 Birkeland current signatures. The simple expedient of a one-quarter orbit period high-pass filter  
245 was used to remove remaining residuals (cf. *Anderson et al.*, 2001). Discrepancies between polar  
246 cap filtered observations during geomagnetic active times, however, indicate that this approach is

247 not ideal (cf. *Knipp et al.*, 2014) and motivated re-examination of the main field signals in the  
248 AMPERE data. The extensive coverage of the data allowed examination of consistency in  
249 patterns in departures from IGRF-11 over days, months, and years. There was a surprisingly  
250 consistent evolution of the global patterns given the low expectations for the instrumentation  
251 stability and accuracy. The results described here were motivated to determine the extent to  
252 which these data may be used to provide a novel means of monitoring changes in the core-  
253 generated field.

254

### 255 **3. AMPERE Data Processing and Science Products Overview**

256 The AMPERE data processing flow is presented to set the context for its application to  
257 main field characterization. It is useful to consider some examples of AMPERE results from  
258 geomagnetically active and quiet conditions to illustrate the character of the Iridium Block 1 data  
259 and the data processing and calibration processes applied to these data. One key aspect of the  
260 rapid coverage over the entire Earth that Iridium provides is the opportunity to identify data  
261 intervals for conditions with the lowest possible contributions from magnetospheric and  
262 ionospheric currents driven by interaction with the solar wind.

263 On the Iridium Block 1 satellites the magnetic field data were used as one input to the  
264 attitude determination process and were calibrated using uploaded tables to enable this on-board  
265 closed-loop process. The target attitude knowledge accuracy was  $\sim 0.1^\circ$ , sufficient to maintain the  
266 inter-satellite communication links upon which the network depended. To specify the scale of the  
267 uncertainty that the attitude accuracy implies, we note that a  $0.1^\circ$  attitude error corresponds to an  
268 error in the magnetic field measurement of 80 nT perpendicular to the field direction at the  
269 altitude of the Iridium satellites. The accuracies needed for auroral science are higher than those

270 required for on-board operations, so post-processing calibrations were used to improve the  
271 estimates of the observed field for AMPERE science (*Anderson et al.*, 2000). The attitude and  
272 measurement accuracies for study of Earth’s magnetic field and the variations in the core-  
273 generated field are substantially more stringent than the requirements for AMPERE,  
274 necessitating additional processing and analysis to identify artifacts in the data and determine  
275 signals most reliably attributed to the main field.

276         It turns out that the errors in the data are randomly distributed and it is only because the  
277 constellation provides a large number of observations that one can determine the mean values to  
278 greater precision than the uncertainty of the individual samples. Below we adopt a grid in  
279 latitude and longitude with bins extending  $9^\circ$  in longitude and  $9^\circ$  in latitude for a total of 800  
280 bins. In one day, the 66 Iridium satellites returned, on an average, 4,440 samples from each space  
281 vehicle (SV) for a total of 293,000 measurements distributed over all latitudes and longitudes, so  
282 the number of samples in each  $9^\circ \times 9^\circ$  bin is  $\sim 360$ . The statistical error in the mean of  
283 measurements with uncertainties of 80 nT is therefore a factor of 20 lower, or  $\sim 4$  nT. This  
284 estimate illustrates how the quantity of data returned and the dense coverage provided by the  
285 constellation compensate both for the attitude knowledge accuracy and the coarse digitization.  
286 This initial estimate is borne out in the analysis and statistics presented below.

287         The magnetometer post-processing calibration requires determination of 12 different  
288 parameters related to the orientations of the three sensing axes (six angles), three offsets or zero  
289 levels, and three gain adjustment factors (cf. *Plaschke et al.*, 2018 and references therein). For  
290 non-spinning spacecraft in LEO, approaches have been developed to co-estimate a non-linear  
291 solution for these parameters together with core model coefficients (cf. *Alken et al.*, 2020). For  
292 AMPERE, we adopted a simpler, linear approach to deriving calibrated perturbations relative to

293 a reference model from the reported observations. This was used to derive the perturbation inputs  
 294 to the science product processing described in detail by *Waters et al. (2020)*.

295 The AMPERE pre-processing proceeds as follows. First, we write  $\mathbf{B}_{\text{SC}}(t)$  to denote the  
 296 data returned by the magnetometer in spacecraft coordinates (SC) at the time  $t$ , converted to  
 297 engineering units using a preliminary scale factor. Spacecraft coordinates are defined as +X in  
 298 the body direction that is nominally ram facing, +Z as the body direction nominally nadir, and  
 299 +Y in the body direction nominally in the orbit normal direction. The spacecraft and  
 300 magnetometer coordinates are identical to within mounting and internal magnetometer  
 301 orientation designs. Departures of the body orientation from these nominal directions are  
 302 provided in the attitude data in terms of roll, pitch, and yaw angles and these angles are used in  
 303 transforming between body (magnetometer) coordinates and geophysical systems. The scale  
 304 factors for Block 1 analysis are those applied on-board the satellite at the time of acquisition. The  
 305 reference model for Earth’s main field in geographic coordinates is written as  $\mathbf{B}_{\text{model-GEO}}$ . In this  
 306 paper, the reference model is IGRF-11 evaluated at the satellite location of each measurement  
 307 with a constant secular variation (*Finlay et al., 2010b*), but we refer to this with the general term  
 308 ‘model’ since the analysis can use any reference model. The next step in the analysis is to  
 309 evaluate the reference model at the location and date-time of each magnetometer sample,  
 310 denoted  $\mathbf{B}_{\text{model-GEO}}(\mathbf{r}(t), t)$ , where  $\mathbf{r}(t)$  is the location of the satellite at the time  $t$ . Using the  
 311 spacecraft attitude, denoted as a four-element quaternion,  $\mathbf{q}(t)$ , we construct a rotation matrix  
 312 from GEO coordinates into the SC frame, denoted  $\underline{\mathbf{A}}_{\text{GEO-SC}}(\mathbf{q}(t))$ . We then transform the  
 313 reference model into the SC frame

$$314 \quad \mathbf{B}_{\text{model-SC}}(\mathbf{r}(t), \mathbf{q}(t), t) = \underline{\mathbf{A}}_{\text{GEO-SC}}(\mathbf{q}(t)) \cdot \mathbf{B}_{\text{model-GEO}}(\mathbf{r}(t), t), \quad (1)$$

315 and calculate the residual between the observed field and the model in the SC frame

316 
$$\Delta \mathbf{B}_{\text{SC}}(t) = \mathbf{B}_{\text{SC}}(t) - \mathbf{B}_{\text{model-SC}}(\mathbf{r}(t), \mathbf{q}(t), t). \quad (2)$$

317 Note that because the magnetometer and spacecraft coordinates are identical, an additional  
 318 rotation from the SC frame into the magnetometer frame is not needed. The calibration is then  
 319 derived by fitting each component of  $\Delta \mathbf{B}_{\text{SC}}(t)$  to the model field using linear regression. We use  
 320 an entire day of data to determine best fits to  $\Delta \mathbf{B}_{\text{SC}}(t)$  in the form

321 
$$\Delta \mathbf{B}_{\text{SC-fit}}(t) = \mathbf{B}_0 + \underline{\mathbf{M}} \cdot \mathbf{B}_{\text{model-SC}}(\mathbf{r}(t), \mathbf{q}(t), t) \quad (3)$$

322 where the offset vector,  $\mathbf{B}_0$ , and matrix,  $\underline{\mathbf{M}}$ , are constants for each day. We do not require that  
 323 these values be the same between different days. The fit can be obtained in closed form since it is  
 324 a simple linear fit, so it is a fast calculation, which is not an insignificant consideration when  
 325 processing data from up to 75 satellites. The residual magnetic field signal that cannot be  
 326 expressed in terms of linear correlations to the reference model is then

327 
$$\delta \mathbf{B}_{\text{SC}}(t) = \Delta \mathbf{B}_{\text{SC}}(t) - \Delta \mathbf{B}_{\text{SC-fit}}(t). \quad (4)$$

328 To see how this relates to a calibration applied to the  $\mathbf{B}_{\text{SC}}(t)$  to obtain a best estimate for a  
 329 calibrated  $\mathbf{B}_{\text{SC}}'(t)$ , we expand equation (4) to

330 
$$\delta \mathbf{B}_{\text{SC}}(t) = \mathbf{B}_{\text{SC}}(t) - \{ \mathbf{B}_0 + (\underline{\mathbf{I}} + \underline{\mathbf{M}}) \cdot \mathbf{B}_{\text{model-SC}}(\mathbf{r}(t), \mathbf{q}(t), t) \}, \quad (5)$$

331 where  $\underline{\mathbf{I}}$  is the identity matrix. Given that the residual,  $\delta \mathbf{B}_{\text{SC}}(t)$  has minimum standard deviation  
 332 for this form of the calibration, the conversion from  $\mathbf{B}_{\text{SC}}(t)$  to calibrated data  $\mathbf{B}_{\text{SC}}'(t)$  is given by

333 
$$\mathbf{B}_{\text{SC}}'(t) = (\underline{\mathbf{I}} + \underline{\mathbf{M}})^{-1} \cdot (\mathbf{B}_{\text{SC}}(t) - \mathbf{B}_0). \quad (6)$$

334 Written this way, it is clear that  $\mathbf{B}_0$  is the offset vector and  $(\underline{\mathbf{I}} + \underline{\mathbf{M}})^{-1}$  is the calibration matrix. The  
 335 matrix elements can be expressed in terms of transformations to orthogonalize the sensing axes,

336 rotate from the effective magnetometer frame into the spacecraft frame, and to apply gain  
337 corrections to each axis to yield a true vector (cf. *Plaschke et al.*, 2019). Note however that any  
338 signals related to sensor or electronics cross-talk between axes is not distinguished from  
339 orthogonality corrections so the interpretation of the calibration matrix is to some extent  
340 ambiguous. Because it is more efficient and hence faster, while preserving the information given  
341 by a non-linear inversion for the orthogonalization parameters that determine the matrix, we  
342 leave the calibration in the matrix form since our only interest is in transforming to the best  
343 estimate true vector field measurement.

344 Results showing the sequence in processing from  $\mathbf{B}_{SC}$  to  $\Delta\mathbf{B}_{SC}$  to  $\delta\mathbf{B}_{SC}$  for 24 May 2010  
345 and Iridium Satellite Vehicle 30, denoted SV030, are shown in **Figure 2** for the entire day. To  
346 more clearly see features of the data at each step in the processing, a subset of the data is shown  
347 in **Figure 3** for the first four hours of the day. **Figures 2** and **3** also show the filtered  $\delta\mathbf{B}_{SC}$  that  
348 are used as the inputs to subsequent AMPERE science processing. Comparing the  $\mathbf{B}_{SC}$  data with  
349 the residuals,  $\Delta\mathbf{B}_{SC}$ , there are clear orbit period signals with amplitudes of about 1 to 2% of the  
350 original signal. The calibration reduces the residuals to less than about 100 to 200 nT amplitude,  
351 making the Birkeland current signatures much more prominent as spikes in the  $\delta\mathbf{B}_{SC}$  time series  
352 (denoted as  $\delta\mathbf{B}$ ), especially in the cross-track or Y component. Signals having periods roughly  
353 half to one quarter of the orbit period remain in the  $\delta\mathbf{B}_{SC}$  time series, and with a source for these  
354 signals not initially identified. To extract the Birkeland current signals more clearly, we therefore  
355 applied a 25-minute period high pass filter to  $\delta\mathbf{B}_{SC}$ . The filtered result is shown in the bottom  
356 row as  $\delta\mathbf{B}_{filtered}$ . The filtering reduced the baseline residuals by about a factor of two without  
357 obviously distorting the Birkeland current signals. This allowed production of the first version of

358 AMPERE science products (*Waters et al.*, 2001, 2020), which have been applied to a range of  
359 questions in auroral and magnetospheric science (cf. *Coxon et al.*, 2018).

360 During active times when the auroral zones expand equatorward, as far as 40° co-latitude,  
361 the 25-minute period can be comparable to the time it takes a polar orbiting satellite to traverse  
362 the auroral zone. Substantial discrepancies between  $\delta\mathbf{B}_{\text{filtered}}$  data from near-conjunctions of  
363 Iridium satellites do occur (*Knipp et al.*, 2014) that turn out to be due to distortions from this  
364 filter. Revisions to the processing are in development to eliminate the filtering step to mitigate  
365 this distortion. The data used here for study of the Earth's field are the  $\delta\mathbf{B}_{\text{SC}}$  before this filtering.

366 The AMPERE products provide an important measure of geomagnetic disturbance and  
367 are used here to identify periods of particularly quiet conditions. It is therefore useful to discuss  
368 the AMPERE processing to illustrate the relationship between quiet conditions and the input data  
369 for the main field analysis. Examples of AMPERE products from two 10-minute intervals during  
370 a geomagnetically active period on 29 May 2010 are shown in **Figure 4**, for 03:30-03:40 UT  
371 (top) and 12:00-12:10 UT (bottom). These data products and tools to generate graphics used here  
372 are available via the AMPERE web page (<http://ampere.jhuapl.edu>). This moderate geomagnetic  
373 storm was driven by an interplanetary magnetic cloud with a southward interplanetary magnetic  
374 field (IMF) of  $-13$  nT. The auroral electrojet index, AE, reached over 1500 nT and the minimum  
375 equatorial storm disturbance index,  $D_{\text{st}}$ , was near  $-60$  nT. The horizontal filtered  $\delta\mathbf{B}$ , denoted  
376  $\delta\mathbf{B}_{\perp}$ , is shown in the left panel by colored arrows. The center panels show the orthogonal  
377 function fit to  $\delta\mathbf{B}$ , labeled  $\delta\mathbf{B}_{\perp\text{-fit}}$ , as described in *Waters et al.* (2020). The anti-sunward  
378 magnetic perturbations in the dawn and dusk sectors associated with the Birkeland currents are  
379 clear, and the basic Region 1/Region 2 current polarities are evident (cf. *Iijima and Potemra*,  
380 1976). Currents in the polar cap at latitudes  $>80^{\circ}$  (in the 12:00 – 12:10 UT interval) are not

381 considered reliable, as they result from discrepancies in the  $\delta\mathbf{B}_\perp$  near the orbit plane crossing  
 382 point. Measurements near the orbit plane crossing point can exacerbate errors in the  $\delta\mathbf{B}_\perp$  owing  
 383 to the small separations between tracks, resulting in spurious filamentary currents. Consistent  
 384 with the bottom rows of **Figures 2** and **3**, the  $\delta\mathbf{B}_\perp$  equatorward of the Birkeland currents are  
 385 below  $\sim 100$  nT in magnitude.

386 The total Birkeland current,  $I_{\text{Tot}}$ , is a convenient measure of the intensity of this high-  
 387 latitude externally-driven current system and is readily calculated from the AMPERE current  
 388 density distributions. As described in *Anderson et al. (2014)*, this calculation is done by setting a  
 389 minimum current density magnitude,  $J_{r,\text{min}} = 0.16 \mu\text{A}/\text{m}^2$ , and then separately integrating the  
 390 upward and downward  $J_r$  whose magnitudes exceed  $J_{r,\text{min}}$  to obtain  $I_{\text{Up},h}$  and  $I_{\text{Down},h}$ , where ‘h’ is  
 391 either N or S to indicate the polar hemisphere being integrated. The threshold magnitude  $J_{r,\text{min}}$   
 392 was determined from the noise level in  $J_r$  during very quiet geomagnetic conditions and reflects  
 393 the end-to-end noise in the data and AMPERE analysis process. The thresholding minimizes  
 394 contributions from lower latitude noise spread over large areas which would otherwise be a  
 395 significant contribution and thereby allows one to evaluate the integrals for  $I_{\text{Up},h}$  and  $I_{\text{Down},h}$   
 396 without imposing arbitrary latitude boundaries. The total current flowing in the Birkeland system  
 397 is defined as

$$398 \quad I_{\text{Tot},h} = \frac{1}{2}(I_{\text{Up},h} - I_{\text{Down},h}), \quad (7)$$

399 and the net current as

$$400 \quad I_{\text{Net},h} = I_{\text{Up},h} + I_{\text{Down},h}. \quad (8)$$

401 The  $I_{\text{Up},N}$  and  $I_{\text{Down},N}$  for the 3:30-3:40 UT interval were 6.08 million Amperes (MA) and -6.12  
 402 MA, respectively, yielding an  $I_{\text{Net},N}$  of  $-0.04$  MA. For the 12:00-12:10 UT interval  $I_{\text{Up},N}$  and

403  $I_{\text{Down},N}$  were 9.25 MA and -8.83 MA, and  $I_{\text{Net},N}$  was +0.42 MA, about 5% of  $I_{\text{Tot},N}$ . The small  
404  $I_{\text{Net},N}$  values are taken in the AMPERE results as uncertainties in  $I_{\text{Tot},N}$ . Inter-hemispheric  
405 currents that have been reported at low latitudes (Lühr *et al.*, 2019) range up to 10s of nA/m<sup>2</sup> and  
406 occur well equatorward of the auroral zones. Inter-hemispheric currents in the auroral zone  
407 Birkeland currents are thought to range between 0.1 and 0.4  $\mu\text{A}/\text{m}^2$ , (Lyatskaya *et al.*, 2014)  
408 comparable to the variability we find in  $I_{\text{Net},h}$ .

409

#### 410 **4. Quiet Day Selection**

411 As illustrated in Figure 4, the coverage of the Iridium constellation allows us to impose  
412 strict limits on geomagnetic activity to select intervals as free of external signals as possible. To  
413 illustrate how intervals of quiet geomagnetic activity were identified and quantified, **Figure 5**  
414 shows the IMF observed by the Advanced Composition Explorer (ACE) spacecraft at the Sun-  
415 Earth Lagrange point 1 (L1) together with three sets of geomagnetic disturbance measures for an  
416 eight day interval in 2010, from May 22<sup>nd</sup> through the 29<sup>th</sup>, which includes the time intervals  
417 shown in **Figure 4**. The three components of the IMF in solar ecliptic (SE) coordinates are  
418 shown in **Figure 5a** color coded as light blue, turquoise, and magenta for  $B_{X,\text{IMF}}$ ,  $B_{Y,\text{IMF}}$ , and  
419  $B_{Z,\text{IMF}}$ , respectively. The IMF magnitude ( $B_{\text{IMF}}$ ) and the negative of the magnitude ( $-B_{\text{IMF}}$ ) are  
420 shown in thick and thin black traces, respectively. The magnetic cloud that was responsible for  
421 the geomagnetic storm on the 2010 May 29 first arrived at L1 around 1800 UT on 2010 May 28  
422 with peak negative  $B_{Z,\text{IMF}}$  occurring between 0300 to 1200 UT on the 2010 May 29.

423 The second, third, and fourth panels of **Figure 5** show the measures of geomagnetic  
424 disturbance used in this study for selection of “quiet” periods. Both the AE and H-index datasets  
425 are available from the Geomagnetic Data Service of the Kyoto World Data Center for

426 Geomagnetism, Kyoto, Japan, (<http://wdc.kugi.kyoto-u.ac.jp/wdc/Sec3.html>). The AE index  
427 indicates high-latitude magnetic perturbations generally resulting from auroral electrojets, while  
428 the SymH and AsyH indices provide a proxy for equatorial magnetic perturbations related to  
429 enhancements in the Earth's ring current. The 24-hour running averages of  $I_{Tot,N}$ ,  $I_{Tot,S}$ , AE,  
430 SymH, and AsyH were used to construct a composite measure of geomagnetic activity. The IMF  
431 data are shown here for context to illustrate that the active periods correspond to strongly  
432 southward IMF as expected, but these data are not needed for the quiet condition determination.  
433 The three 24-hour intervals highlighted by light yellow rectangles in Figure 5b-d indicate a set of  
434 quiet intervals selected for analysis of the main field.

435 To select quiet 24-hour periods, we first constructed normalized quantities from the  
436 disturbance measures shown in Figure 5. The running 24-hour average of a quantity,  $g$ , is  
437 denoted by angle brackets,  $\langle g \rangle$ . We calculated a total current from the 24-hour averages

$$438 \quad I_{Tot} = \langle I_{Tot,N} \rangle + \langle I_{Tot,S} \rangle. \quad (9)$$

439 Using both  $\langle I_{Tot,N} \rangle$  and  $\langle I_{Tot,S} \rangle$  rather than just one hemisphere has the advantage of muting  
440 seasonal influence on the Birkeland currents driven by polar ionospheric illumination variations.  
441 We also used both SymH and AsyH since these indices represent different sets of external  
442 currents: SymH primarily represents the symmetric ring current and symmetric magnetospheric  
443 compressions, while AsyH reflects the storm-time asymmetric ring current, at times with  
444 substantial contribution of from the cross-tail current. We therefore calculated

$$445 \quad H = |\langle \text{SymH} \rangle| + |\langle \text{AsyH} \rangle|, \quad (10)$$

446 to capture all of these effects. We then normalize the  $I_{Tot}$ ,  $\langle \text{AE} \rangle$ , and  $H$  values by constructing z-  
447 distributions for each using one month of data to define the distributions. For example, from a

448 month of  $I_{\text{Tot}}$  values we evaluated the average,  $m_{I_{\text{Tot}}}$ , and the standard deviation,  $\sigma_{I_{\text{Tot}}}$ , and  
449 calculated a normalized value as

$$450 \quad V_{I_{\text{Tot}}} = (I_{\text{Tot}} - m_{I_{\text{Tot}}}) / \sigma_{I_{\text{Tot}}}, \quad (11)$$

451 known as the z-score. This was similarly done for  $\langle \text{AE} \rangle$  and  $H$  to obtain  $V_{\text{AE}}$  and  $V_H$ ,  
452 respectively. We then took the average of these three normalized disturbance parameters to  
453 derive a single composite disturbance parameter,  $Q$ ,

$$454 \quad Q = (V_{I_{\text{Tot}}} + V_{\text{AE}} + V_H) / 3, \quad (12)$$

455 which is positive (negative) for conditions that are more (less) disturbed than the average taking  
456 into account Birkeland currents, auroral electrojets, and ring current-tail-compression dynamics.

457 The time series for  $Q$  were then used to determine quiet 24-hour intervals. We then  
458 identified the quietest 7 periods in each month. This was done by finding the minimum  $Q$ ,  
459 logging it, removing all  $Q$ -values within this period, and then searching for a new minimum  $Q$  in  
460 the remaining data until 7 non-overlapping 24-hour periods were identified and logged. To  
461 ensure that there is at least some quiet data from every month, we also selected the three quietest  
462 periods in each month. Then, because not all months were equally quiet, we collected from the  
463 remaining periods, the 12 second quietest ones for each quarter of the year centered on solstice  
464 or equinox months (i.e., Nov-Jan, Feb-Apr, May-Jul, Aug-Oct). Thereafter we selected the  
465 quietest 4 from these 12. Altogether, the above selection criteria yielded 262 quiet 24-hour  
466 periods for January 2010 through November 2015. As of this writing, 8 months of Iridium Block  
467 1 magnetometer data during this span are not currently available. Hence, data for August and  
468 September 2013, June and July 2014, and November 2014 through February 2015 are not  
469 included in the analysis. For quarters with missing months, the number of additional quiet

470 periods were reduced to 2 periods if only two months were available or 1 period if only one  
471 month was available. No quarter was devoid of data. The three quiet periods occurring during the  
472 interval marked in **Figure 5** by the yellow boxes were 2010-05-22/12:00 – 2010-05-23/12:00;  
473 2010-05-23/21:00 – 2010-05-24/21:00; and 2010-05-27/03:00 – 2010-05-28/03:00. **Table S1** in  
474 the Supporting Information lists all 262 intervals together with parameters used to derive the z-  
475 scores and the final values for  $Q$  for each interval.

476 It is instructive to contrast these quiet periods with the moderate storm time interval  
477 shown in **Figure 4**. The examples of **Figure 6**, in the same format as **Figure 4**, are for 2010 May  
478 23 at 02:00-02:10 UT (top) during the quietest interval of the 8-day span shown in **Figure 5** and  
479 for 2010 May 27 at 12:00-12:10 UT (bottom) during the least quiet of the three identified quiet  
480 periods. The first interval exhibits a cluster of perturbations near noon around 80°N magnetic  
481 latitude, typical of Birkeland currents during northward IMF (cf. *Anderson et al.*, 2008), but  
482 there are no systematic signals equatorward of ~70°N magnetic latitude. The relatively small  
483 signals, <100 nT, at lower latitudes are typical for uncorrectable, that is, unidentified, noise and  
484 variations consistent with vehicle attitude uncertainty. For the case of 2010 May 27 at 12:00-  
485 12:10 UT, there are evident R1/2 currents poleward of ~67°N, at significantly higher latitudes  
486 than the active time currents in **Figure 4** but with signals below ~300 nT, which are less than  
487 ~1/5<sup>th</sup> of the more active time signals. This 2010 May 27 interval in **Figure 6** represents the most  
488 active conditions included in the quiet interval database, while the 2010 May 23 case in **Figure 6**  
489 is more typical of the quiet conditions for the database.

490

## 491 **5. Data Pre-Processing for Earth's Main Field**

492           The first step in pre-processing the calibrated Iridium data for study of Earth's main field  
493 is to transform the data into geographic coordinates and assess whether the data seem to be  
494 ordered by geographic location. The second step is to examine the distributions of the residuals  
495 to assess whether the errors appear to be random, and to evaluate their averages in suitable  
496 latitude-longitude ranges and estimate the errors in the means for each bin. The first indication  
497 that the Iridium constellation data may record useful information on Earth's main magnetic field  
498 was the presence of consistent patterns when plotting the residuals transformed to spherical  
499 geographic coordinates,  $\delta B_r$  (radial),  $\delta B_\theta$  (polar angle positive southward), and  $\delta B_\phi$  (azimuthal  
500 positive eastward), and registered in geographic latitude and longitude. Two examples of the  
501 residuals obtained from the two nearly consecutive quiet intervals shown in **Figure 5** are shown  
502 in **Figure 7**. The plot shows all of the samples from every satellite, totaling ~290,000 points,  
503 plotted as colored dots for 2010-05-22/12:00 – 2010-05-23/12:00 on the left and 2010-05-  
504 23/21:00 – 2010-05-24/21:00 on the right. One significant point to note is that the distributions  
505 of  $\delta B$  in **Figure 7** are not a random mixture of positive and negative values but appear to be  
506 organized into coherent regions. For example, the  $\delta B_r$  pattern for both quiet periods show several  
507 broad, 60°-wide longitude bands of positive values, one from -90° to -30° E and 0° to 30° N  
508 latitude, another from 0° to 90° E and -45° to 0° N, and a third from about 120° to 180° E and 0°  
509 to 60° N. The  $\delta B_\theta$  distributions show a broad positive band in the southern hemisphere and a  
510 region of northward (negative) field from -90° to 0° E and 20° to 60° N. In addition, these  
511 general patterns are consistent between the two quiet periods. The signals that are the least  
512 consistent between the two days are at high latitudes, poleward of 70° N in  $\delta B_\phi$  in the northern  
513 hemisphere, arising from the Birkeland current signals (cf. **Figure 6**).

514 Results from two additional consecutive quiet periods from November 2015 are shown in  
515 **Figure 8**. These intervals from 2015-11-21/06:00 – 2015-11-22/ 06:00 and 2015-11-22/06:00 –  
516 2015-11-23/06:00 exhibit larger residuals with very clear patterns consistent between the two  
517 days, but ones that are quite different from the patterns shown in **Figure 7**. In  $\delta B_r$  distributions  
518 there are three regions of positive residuals, one between  $40^\circ - 70^\circ$  N and  $-180^\circ$  to  $-90^\circ$  E, a  
519 second centered on  $-45^\circ$  E and  $10^\circ$  N spanning about  $40^\circ$  in longitude and latitude, and a third  
520 roughly ‘U’-shaped region from  $30^\circ$  E to  $180^\circ$  E with a strongest band at about  $50^\circ$  S spanning  
521  $60^\circ$  to  $120^\circ$  E. In the equatorial zone,  $30^\circ$  S to  $30^\circ$  N, the  $\delta B_r$  has a roughly 3-wave structure with  
522 longitude. The  $\delta B_\theta$  distributions show intense positive residuals at high southern latitudes,  
523 poleward of  $60^\circ$  S from  $30^\circ$  E to  $120^\circ$  E, a broad zone of moderately positive residuals  
524 from  $-180^\circ$  E to  $0^\circ$  E south of about  $30^\circ$  N, and an arc of negative  $\delta B_\theta$  from  $\sim 70^\circ$  N at  $-180^\circ$  E  
525 extending across  $0^\circ$  E at  $60^\circ$  N and to  $20^\circ$  S at  $90^\circ$  E. The slightly sinusoidal shaped high-latitude  
526 Birkeland current signatures are most evident in the southern polar region in  $\delta B_\phi$  poleward of  $60^\circ$   
527 S, but  $\delta B_\phi$  also exhibits a roughly wave-like pattern of residuals across all longitudes extending  
528 from about  $30^\circ$  S to  $30^\circ$  N. The peaks in the equatorial  $\delta B_\phi$  residuals correspond roughly to  
529 midpoints between extrema in a similar 3-wave pattern in the  $\delta B_r$ . As with the pair of quiet  
530 intervals from May 2010, these two periods in November 2015 illustrate a highly coherent  
531 pattern in the  $\delta \mathbf{B}$  when registered in geographic latitude and longitude, as well as a remarkable  
532 consistency between the two periods. The magnitudes of the residuals are substantially greater in  
533 November 2015 than they were in May 2010, indicating that the secular variation extrapolation  
534 from 1 January 2010 used in the IGRF-11 model may be departing more substantially in the later  
535 years. The remarkable feature of these examples is that these global maps were obtained in just a  
536 single day of observations and yield highly consistent results.

537 To assess the statistical uncertainties and confidence of the mean perturbations in the  
538 geographical patterns found in **Figures 7 and 8**, we first divided the observations into 20 latitude  
539 and 40 longitude bins, each  $9^\circ$  in latitude by  $9^\circ$  in longitude. The bin size is a trade-off between  
540 maximizing the statistics in each bin, which favors larger bins, and retaining enough spatial  
541 resolution to resolve wavelengths at least as short as the distance from the core to the satellite  
542 altitude. For Iridium altitude, the core is about 3800 km below the satellites, and this wavelength  
543 corresponds to an azimuthal order of  $\sim 12$  at the equator. The  $9^\circ \times 9^\circ$  bin size allows a harmonic  
544 decomposition up to degree and order 20. Given the average number of samples obtained in one  
545 day by the 66 Iridium Block 1 satellites, a typical number of  $\sim 360$  samples comprise each  
546 latitude-longitude bin. All of the  $\delta B$  measurements within each bin are averaged for each quiet  
547 period. Because the Iridium satellites are in near polar orbits, the number of samples in each bin  
548 is nearly uniform with latitude even though the area of the bins decreases toward the poles. The  
549 bin averages for the 2010 May 22-23 and 2010 May 23-24 quiet intervals are shown in **Figure 9**.  
550 Similarly, averages for 2015 November 21-22 and 2015 November 22-23 are shown in **Figure**  
551 **10**. For both sets of quiet periods, the bin averages reveal that the patterns from the individual  
552 observations throughout the satellite orbits are consistently present in the means. The  
553 perturbation regions are also more clearly evident, and there is consistency, even in relatively  
554 small-scale features (i.e., below  $20^\circ$  in latitude and longitude), between successive days.

555 To assess the residual distributions relative to the means we examined the distribution of  
556 all residuals for individual quiet periods. As an example of this assessment, the distributions for  
557 all measurements of  $\delta B_r$ ,  $\delta B_\theta$ , and  $\delta B_\phi$  are shown for a quiet interval from 2015 November 21 –  
558 22 in **Figure 11**. The Gaussian fit to each distribution very closely follows the actual data  
559 distribution, indicating that the data are primarily normally distributed. Similar Gaussian

560 distributions are obtained when considering the averaged data within each latitude-longitude bin.  
 561 The normal character of the distributions is consistent with a random error due to the attitude  
 562 determination uncertainty of  $\sim 80$  nT. The standard deviations for each latitude-longitude bin for  
 563 2010 -05-22 /12:00 –2010-05-23/12:00 and for 2015-11-21/06:00 – 2015-11-22/06:00 are shown  
 564 in **Figure 12**. The standard deviations within each bin range from about 40 nT to 100 nT with the  
 565 highest values in the polar latitudes (i.e., higher than  $\pm 60^\circ$ ), corresponding to the auroral zones  
 566 and so reflecting the variability of the natural signals there.

567 For potential use in specifying the main field, the standard deviation of measurements in  
 568 each bin is less important than the uncertainty of the mean. With about 350 points in each bin,  
 569 the standard error in the mean is roughly a factor of 18 smaller than the standard deviation. Maps  
 570 of the standard errors in the mean are shown in **Figure 13** for the same two intervals and in the  
 571 same format. The standard errors are generally below 3 nT for the May 2010 case and between 3  
 572 and 5 nT for the November 2015 case shown in **Figure 12**. The increase in the standard errors is  
 573 primarily due to the fact that there were somewhat fewer satellites operating in fine attitude  
 574 control mode as the Block 1 satellites were experiencing degraded performance of some  
 575 subsystems, and hence there were somewhat fewer magnetic field measurements in the analysis.  
 576

## 577 **6. Spherical Harmonic Fitting**

578 To examine the temporal behavior of the patterns in the residuals we constructed  
 579 spherical harmonic representations of each quiet period and investigated the time dependence of  
 580 the harmonic coefficients. The spherical harmonic functions  $Y_{lm}(\theta, \phi)$  are orthonormal basis  
 581 functions on a spherical surface which means the following:

$$582 \int_0^{2\pi} d\phi \int_0^\pi \sin(\theta) d\theta Y_{l_1 m_1} Y_{l_2 m_2}^* = \delta_{l_1 l_2} \delta_{m_1 m_2} \quad (13)$$

583 where \* denotes the complex conjugate and  $\delta_{ij}$  is the Kronecker delta function. Expressing  $Y_{lm}$  in  
 584 terms of the associated Legendre function,  $P_{lm}(x)$ ,

$$585 \quad Y_{lm}(\theta, \phi) = a_{lm} P_{lm}(\cos \theta) e^{im\phi} \quad (14)$$

586 where the  $a_{lm}$  are the normalization coefficients, one can also write

$$587 \quad \int_0^{2\pi} d\phi \int_0^\pi \sin(\theta) d\theta a_{l_1 m_1} P_{l_1 m_1}(\cos \theta) \cos(m_1 \phi) a_{l_2 m_2} P_{l_2 m_2}(\cos \theta) \cos(m_2 \phi) = \delta_{l_1 l_2} \delta_{m_1 m_2} \quad (15a)$$

$$588 \quad \int_0^{2\pi} d\phi \int_0^\pi \sin(\theta) d\theta a_{l_1 m_1} P_{l_1 m_1}(\cos \theta) \sin(m_1 \phi) a_{l_2 m_2} P_{l_2 m_2}(\cos \theta) \sin(m_2 \phi) = \delta_{l_1 l_2} \delta_{m_1 m_2} \quad (15b)$$

589 which explicitly separates the sine and cosine terms. Here we use the convention that  $m = 0$  to  $l$

590 (rather than  $m = -l$  to  $l$ ), so the normalization coefficients are

$$591 \quad a_{l0} = \sqrt{\frac{(2l+1)}{4\pi}} \text{ for } m = 0 \quad (16a)$$

$$592 \quad a_{lm} = \sqrt{\frac{(2l+1)(l-m)!}{2\pi(l+m)!}} \text{ for } m > 0. \quad (16b)$$

593 The convenience of equation 15 is that it allows one to calculate the coefficients contributing to

594 the patterns of the residuals directly from convolution integrals. Given the maps for  $\delta B_r(\theta, \phi, t_i)$ ,

595  $\delta B_\theta(\theta, \phi, t_i)$ , and  $\delta B_\phi(\theta, \phi, t_i)$  for each quiet interval, denoted  $t_i$ , the harmonic coefficients for each

596 pattern are given by

$$597 \quad \mathbf{c}_{lm}(t_i) = \int_0^{2\pi} d\phi \int_0^\pi \sin(\theta) d\theta \delta \mathbf{B}(\theta, \phi, t_i) a_{lm} P_{lm}(\cos \theta) \cos(m\phi) \quad (17a)$$

$$598 \quad \mathbf{s}_{lm}(t_i) = \int_0^{2\pi} d\phi \int_0^\pi \sin(\theta) d\theta \delta \mathbf{B}(\theta, \phi, t_i) a_{lm} P_{lm}(\cos \theta) \sin(m\phi). \quad (17b)$$

599 These integrals were evaluated by summing the average  $\delta\mathbf{B}$  in each  $9^\circ$  by  $9^\circ$  bin multiplied by  
600 the spherical harmonic evaluated at the bin center latitude and longitude and multiplied by the  
601 bin solid angle. The integrals are evaluated using a discrete sum which was checked with a unity  
602 argument in the integrand which yielded  $4\pi$  to within 0.1%. The coefficient values are mostly  
603 below 10 nT and all below  $\sim 50$  nT, so the errors in the coefficients are typically less than 0.01  
604 nT and all less than 0.05 nT. The convolution also assumes that all of the data are from the same  
605 spherical shell, which is not strictly true. The Iridium satellites are in slightly eccentric orbits: the  
606 maximum and minimum altitudes differ from the mean by 9 km, a difference in geocentric  
607 distance of 0.13%. For the low degree coefficients for which the amplitudes reach 50 nT, this  
608 leads to errors not larger than  $\sim 0.2$  nT. For  $l = 13$ , the maximum error from the spherical shell  
609 approximation increases to 1.9% but the coefficients are all below 5 nT so the errors in the  
610 results are below 0.1 nT. The bin angular sizes allow for evaluation of coefficients up to degree  
611 and order 20, but the time series in the coefficients above degree 13 did not exhibit systematic  
612 trends above the noise level in the results over the five years analyzed here.

613         The coefficients given by these convolution integrals are the coefficients of the expansion  
614 of the patterns in each component in terms of spherical harmonics and must be distinguished  
615 from the conventional Gauss coefficients that are used to express the Earth's field in IGRF,  
616 WMM, and other main field models. Neither a radial dependence nor constraints that the  
617 coefficients in Equation 17a-b correspond to physical solutions for Earth's field are implied. For  
618 instance, there is no constraint that the  $\mathbf{c}_{00}(t_i)$  be zero, which allows for identification of spurious  
619 signals in the results. The  $\mathbf{c}_{lm}(t_i)$  and  $\mathbf{s}_{lm}(t_i)$  are a convenient way to represent the patterns for each  
620 quiet period and allow us to examine the time variation of the coefficients to identify systematic  
621 behavior of different angular and temporal scales. From the time series of the coefficients,

622 artifacts in the dataset can be pinpointed and removed from the  $\mathbf{c}_{lm}(t_i)$  and  $\mathbf{s}_{lm}(t_i)$ . Revised maps  
623 of field perturbations, from which unphysical artifacts are subtracted can also be reconstructed.

624 As an example, the time series of  $\mathbf{c}_{lm}(t_i)$  and  $\mathbf{s}_{lm}(t_i)$  for  $l = 2$  over the entire span of the  
625 quiet interval data are shown in **Figure 14**. The figure also shows the  $c_{r,00}$  time series with gray  
626 lines and open circles. Because  $c_{r,00}$  corresponds to a magnetic charge it is clearly unphysical and  
627 we use the time series of  $c_{r,00}$  as one indicator of artifacts in the signals. One of the most striking  
628 features of the time series are annual and shorter period ( $\sim 8$  months) variations in the coefficient  
629 amplitudes, primarily in the  $m = 0$  coefficients. The annual signal is most clear in the  $c_{\phi,20}$  (black  
630 dots and lines in **Figure 14f**). (Note that hereinafter we omit the ‘ $(t_i)$ ’ for simplicity although the  
631 time series is always implied.) The shorter period, 8-month signal, is clearest in  $c_{r,20}$  (black dots  
632 and lines in **Figure 14b**). We note that the  $\mathbf{s}_{20}$  are identically zero by definition. Other non-zero  
633 coefficients indicate variations at similar periods, for example  $c_{0,20}$ ,  $s_{r,21}$ ,  $s_{0,21}$ , and  $c_{\phi,22}$ . Other  
634 coefficients show very little of these periodicities and exhibit slower trends, indicative of  
635 departures from secular variation, for example in  $c_{r,22}$ ,  $s_{r,21}$ ,  $s_{r,22}$ ,  $c_{\phi,21}$ , and  $s_{\phi,22}$ . The amplitudes of  
636 the slow variations and of the periodic signals are all on the order of  $\sim 10$  to  $80$  nT, down to  
637 levels below the magnetometer digitization of  $30$  nT, consistent with the several nT statistical  
638 errors of the means of the average field in each latitude-longitude bin.

639 The 12-month period suggests a variation in magnetometer response with season, that is,  
640 with mean solar exposure around the orbit. The  $86^\circ$  inclination orbits have an 8-month local time  
641 precession period, so that this is the periodicity in the local time of orbital ascending/descending  
642 node. The 8-month period variation in  $c_{r,20}$  suggests that there is a bias in the magnetometer  
643 response with the solar illumination history around the orbit and this is confirmed by a very  
644 similar signal in  $c_{r,00}$ . A possible contribution to this bias is the temperature calibration for the

645 magnetometers, which was applied in Iridium pre-processing on board the satellites. However,  
646 we found no systematic variation of the  $\delta B_{SC}$  with magnetometer temperature, consistent with  
647 the correct application of this calibration. Nonetheless, a response with the annual and precession  
648 periods is evident in many coefficients and might be related to temperature gradients at the  
649 magnetometer or other dynamic thermal characteristics of the vehicles. With the data available at  
650 this time it is not possible to fully diagnose what causes these signals, but the correlation with the  
651 8-month orbit and 12-month seasonal periods imply that these signals are most likely artifacts,  
652 and in an abundance of caution we treat them as such. That artifacts are present in the data was  
653 clear as the  $c_{q,00}$  were not identically zero. Particularly for  $c_{r,00}$ , the  $c_{00}$  have amplitudes and  
654 periods comparable to those of **Figure 12**.

655         The presence of a monopole signal may seem alarming at first, although one must  
656 remember that the convolution approach applies no physical constraints on the coefficients. In  
657 fact, the  $l = 0$  terms are useful diagnostics. The  $c_{r,00}$  signals are attributed to offsets in  $\delta B_{r,SC}$ :  
658 since the spacecraft fly maintaining a nadir orientation, the r-component is always radial and  
659 hence an error in the zero level will appear in  $c_{r,00}$ . It is worth noting that the calibration approach  
660 which identifies the zero levels from the time series data can give a spurious baseline since the  
661 convolution integral of Equation 16 for  $l = 0$  is essentially a mean, weighted by the solid angle  
662 since  $Y_{00}$  is a constant. Hence, the time series analysis for the offsets and  $c_{r,00}$  are actually  
663 different, and this accounts for the residual artifact in  $c_{r,00}$  arising from time variations in the zero  
664 level around the orbit. If the instrument zero levels were constant, the time series offset would be  
665 correct and the convolution results would be zero. This information therefore serves as a  
666 diagnostic of these orbit variation artifacts.

667           The  $c_{r,00}$  and any other signals at 12- or 8-month periods and their harmonics are  
668 considered as artifacts and were removed as follows. Great care was used in preparing the time  
669 series of the  $c_{lm}$  and  $s_{lm}$  for spectral analysis with the objective to notch filter only the frequencies  
670 of the orbital period artifacts and then reconstruct the time series without disturbing the slower  
671 trends or introducing distortions from windowing. The first step was to detrend the time series by  
672 fitting them with a 5<sup>th</sup> order polynomial fit and then subtracting this fit. This same fit was added  
673 back in to preserve these non-periodic trends after removing the periodic signal artifacts. The  
674 second step was to construct longer time series from the detrended  $c_{lm}$  and  $s_{lm}$  by reflecting the  
675 original time series about the first and last time sample. We denote the span of the original time  
676 series as  $T_{data}$ . This yielded a pseudo time series that is three times longer than the original but  
677 which could be windowed, notch filtered, and inverted back to a time series without applying  
678 any windowing distortion to the original time series in the center third of the new pseudo time  
679 series. The mirroring ensures that the extension of the original time series did not introduce  
680 discontinuities that would have generated artificial harmonic series in the Fourier transforms. An  
681 example of this mirrored pseudo time series is shown in the top red trace of **Figure 15**, for  $c_{r,20}$ .

682           The first step in the Fourier analysis was the application of the fast Fourier transform  
683 (FFT) window shown by the gray trace in the top of **Figure 15**. The ends of the window are half-  
684 cosines extending  $0.8T_{data}$  from the ends. The center of the window is constant at 1 from  $-0.2T_{data}$   
685 to  $1.2T_{data}$ . The data multiplied by this window function are shown by the blue trace in **Figure**  
686 **15**. This windowed time series was then converted into a continuous, evenly sampled time series  
687 by interpolating to a 3-hour spaced time series, corresponding to the smallest time increment in  
688 the original quiet interval selection (cf. **Section 4** above). The resulting windowed and  
689 oversampled data was then transformed using an FFT. To produce the “notch” filter, the Fourier

690 coefficients nearest the 12-month and 8-month periods and their harmonics (up to the sixth  
691 harmonic), along with one frequency bin above and below those nearest bins, were set to zero.  
692 The notched transform was then inverted to obtain the filtered residual signal shown by the light  
693 green trace in **Figure 15**. The fraction of frequency bins notched in this way was less than 10%  
694 of the number of frequencies, so that the fraction of true signal removed was not larger than 10%  
695 even though the contamination signal is much larger than this. In addition, the notched Fourier  
696 coefficients were extracted and transformed to the time domain to construct a time series of this  
697 artifact signal. The thick, black trace labeled ‘Notch filt.’ in **Figure 15** shows the time series of  
698 the signal that was removed. The signal in the  $c_{r,20}$  at the 8- and 12-month periods and harmonics  
699 is a large fraction of the original signal, but for the majority of the  $c_{lm}$  and  $s_{lm}$  the notch filtered  
700 signal is much smaller.

701         After notch filtering to remove artifacts related to orbital dynamics, the filtered residual  
702  $c_{lm}$  and  $s_{lm}$  were compared to the filtered residual  $c_{r,00}$ . To do this comparison, the same filtering  
703 process was first applied to the  $c_{r,00}$ , and where the residual signals in the filtered  $c_{r,00}$  were  
704 considered to be erroneous as well. We then evaluated and subtracted from the filtered  $c_{lm}$  and  
705  $s_{lm}$  the linear correlation between the filtered  $c_{r,00}$  and the filtered  $c_{lm}$  and  $s_{lm}$ , where the slope of  
706 the linear fit is denoted by ‘ $k$ ’ in **Figure 15**. This subtracted signal for  $c_{r,20}$  is shown by the  
707 orange trace overlaid on the light green filter residual signal in **Figure 15**. This resulting signal  
708 shows that a substantial fraction even of the filtered signal in this case was highly correlated with  
709 the filtered  $c_{r,00}$ . The total correction, arising from the sum of the notch filter signal with the  
710 correlated  $c_{r,00}$  signal, is shown by the thin black trace **Figure 15**, labeled ‘Net correction’. The  
711 final corrected time series of  $c_{r,20}$  with this correction subtracted is shown in the bottom dark  
712 green trace, labeled as ‘Corrected  $c_{r,20}$ ’.

713 The corrected  $\mathbf{c}_{lm}$  and  $\mathbf{s}_{lm}$ , resampled at the dates of the original data and to which the  
714 long-term trends have been added back in (removed before frequency analysis and notch  
715 filtering), are denoted by a prime as  $\mathbf{c}'_{lm}$  and  $\mathbf{s}'_{lm}$ . The  $\mathbf{c}'_{lm}$  and  $\mathbf{s}'_{lm}$  for  $l = 2$  are shown in **Figure**  
716 **16** using the same format as **Figure 14**. The most prominent features of these corrected time  
717 series are now the slow trends evident in the power (**Figure 16a**), with the largest slow variation  
718 in  $s_{r,2l}'$ , and also present in most of the coefficient time series. The noisiest time series are  $c_{\theta,2l}'$   
719 and  $s_{\theta,2l}'$  which exhibit  $\sim 40$  nT and  $\sim 20$  nT peak-to-peak variations, respectively, between just a  
720 few samples. These variations are likely spurious but not corrected with the process  
721 implemented, as these signals did not display any clear periodicities and so were not clearly  
722 attributable to any particular source. The other time series have peak-to-peak noise levels of  
723 between 5 nT and 20 nT which we consider the limit of the present Iridium Block 1 data and the  
724 processing described here. The long-term trends appear to be well resolved and the rapid  
725 variations between successive quiet periods could be mitigated with modest low pass filtering to  
726 resolve variations on time scales as short as one or two months.

727 To assess how much artifact signals contribute to the patterns of the  $\delta\mathbf{B}$  shown in **Figures**  
728 **7 – 10**, we used the  $\mathbf{c}'_{lm}$  and  $\mathbf{s}'_{lm}$  up through  $l = 13$  to reconstruct the  $\delta\mathbf{B}$  maps. The results of the  
729 reconstructed  $\delta\mathbf{B}$  maps from the  $\mathbf{c}_{lm}$  and  $\mathbf{s}_{lm}$ , before artifact correction, are shown in the left hand  
730 columns of **Figure 17** and **Figure 18** for 2010-05-23/21:00 – 2010-05-24/21:00 and 2015-11-  
731 21/06:00 – 2015-11-22/06:00, respectively. The reconstructed  $\delta\mathbf{B}$  maps agree very closely with  
732 the maps of the binned averages (**Figure 9** right hand column and **Figure 10** left hand column).  
733 The reconstructed  $\delta\mathbf{B}$  maps from the  $\mathbf{c}'_{lm}$  and  $\mathbf{s}'_{lm}$ , after artifact correction, are shown in the center  
734 columns of **Figures 17** and **18**. In both cases the filtered coefficient results retain the patterns in  
735 the original binned data with relatively small changes. For example, for the 2010 May 23 – 24

736 case near  $10^\circ$  to  $30^\circ$  N latitude there is a positive  $\delta B_r$  signal across all longitudes which is not  
737 discernible in the filtered map. Thus, the obvious periodicities in some of the  $\mathbf{c}_{lm}$  and  $\mathbf{s}_{lm}$  were not  
738 significant contributors to the original coherence in the geographically registered residuals  
739 relative to IGRF-11.

740 To check whether the Iridium results are consistent with independent models, we  
741 subtracted the IGRF-11 model from the CHAOS 7.4 model (*Finlay et al.*, 2020;  
742 <https://doi.org/10.5281/zenodo.3352398>), both at 780 km altitude. These results are shown in the  
743 right hand columns of **Figure 17** and **Figure 18**. Considering the November 2015 case first, all  
744 three components of the field have similar patterns in the Iridium and CHAOS 7.4 residuals. The  
745 linear regression coefficient for  $\delta B_r$  between the corrected Iridium and CHAOS 7.4 residuals is  
746 0.82. The standard deviations of the Iridium residuals are 52 nT, 31 nT, and 36 nT for  $r$ ,  $\theta$ , and  $\phi$ ,  
747 respectively, while for the CHAOS7.4 residuals the standard deviations are 59 nT, 36 nT, and 40  
748 nT, for  $r$ ,  $\theta$ , and  $\phi$ , respectively. For May 2010, the correspondence between the corrected  
749 Iridium residuals and the CHAOS 7.4 residuals is not as strong. The linear regression coefficient  
750 for  $\delta B_r$  is lower, 0.41, and the standard deviations in  $\delta \mathbf{B}$  are also different: for the corrected  
751 Iridium residuals they are 34 nT, 24 nT, and 19 nT, for  $r$ ,  $\theta$ , and  $\phi$ , respectively, whereas for the  
752 CHAOS 7.4 residuals they are 17 nT, 11 nT, and 10 nT,  $r$ ,  $\theta$ , and  $\phi$ , respectively. To compare the  
753 change from May 2010 to November 2015 we took the difference in residuals, the November  
754 2015 residuals minus those from May 2010. The statistics of the changes in  $\delta \mathbf{B}$  residuals are  
755 similar, with standard deviations in  $r$ ,  $\theta$ , and  $\phi$ , respectively, of 43 nT, 29 nT, and 33 nT from  
756 Iridium and 46 nT, 27 nT, and 32 nT for CHAOS7.4. The Iridium and CHAOS 7.4 changes in  
757  $\delta \mathbf{B}$  are well correlated with linear regression coefficients of 0.89, 0.48, and 0.78 for  $r$ ,  $\theta$ , and  $\phi$ ,  
758 respectively. The standard deviations in the Iridium residuals minus the CHAOS 7.4 residuals

759 are 21, 29, and 22 nT, in  $r$ ,  $\theta$ , and  $\phi$ , respectively. Over the 5.5-year baseline, this suggests that  
760 the annual variations agree on average to  $\sim 5$  nT/yr at the 1-sigma level.

761 To compare the evolution of residual patterns over the six-year interval analyzed, **Figure**  
762 **19** shows maps of the  $\delta B_r$ , corresponding to the top center and right panels of **Figures 17** and **18**,  
763 for six dates close to 1 August separated by one year. The correlation between the  $\delta B_r$  patterns is  
764 generally high and increases over time although there are some systematic differences. Both  
765 Iridium and CHAOS have prominent positive  $\delta B_r$  features near  $-60^\circ$  lon. near the equator and  
766 near  $+60^\circ$  lon. and  $-45^\circ$  lat., although this feature is not initially as strong in the CHAOS-derived  
767 maps as in the Iridium residuals. These two positive  $\delta B_r$  features are separated by a band of  
768 negative  $\delta B_r$  extending from  $-20^\circ$  lon. and  $-60^\circ$  lat. to the equator and  $0^\circ$  lon. in the CHAOS  
769 maps for all years, but they are nearly contiguous positive  $\delta B_r$  regions in the Iridium results until  
770 2014. Both patterns show the development of a positive  $\delta B_r$  feature between  $-180^\circ$  and  $-120^\circ$  lon.  
771 between  $50^\circ$  and  $80^\circ$  lat., although it is a bit narrower in latitude in the Iridium results. This  
772 feature is present in all of the CHAOS maps but not initially in the Iridium results. The  
773 prominent negative  $\delta B_r$  feature near  $100^\circ$  lon. and extending between  $-20^\circ$  and  $+45^\circ$  lat. develops  
774 in both sets of residuals. Initially, the Iridium results have a double peaked  $\delta B_r$  feature centered  
775 near  $145^\circ$  lon. between the equator and  $70^\circ$  lat. which is not present in the CHAOS residuals but  
776 by August 2014 this feature in the Iridium patterns has merged with the positive  $\delta B_r$  region at  
777 more southern latitudes to form a shape similar to the CHAOS residuals in the southeastern  
778 positive  $\delta B_r$  feature. The results for  $\delta B_\theta$  and  $\delta B_\phi$  are presented in **Figures S1** and **S2** in the  
779 Supporting Information and exhibit essentially the same high degree of correspondence.

780

## 781 **7. Discussion and Conclusions**

782           Analysis of magnetometer data from the Iridium Communications Block 1 satellites  
783 revealed coherent signatures and distributions in the departures of the calibrated observations  
784 relative to the IGRF-11 model when registered in geographic coordinates. Although there are  
785 substantial standard deviations (up to  $\sim 80$  nT) in the localized latitude-longitude ranges used for  
786 the field mapping analysis ( $9^\circ$  latitude by  $9^\circ$  longitude solid angle bins), the values are consistent  
787 with uncertainties in the Iridium Block 1 attitude determination system. The magnetic field  
788 residuals form Gaussian distributions consistent with a random error in the data. The large  
789 number of measurements in each solid angle bin afforded by the constellation in one day ( $\sim 350$   
790 independent measurements) therefore imply standard errors in the mean of 2 to 4 nT, possibly  
791 low enough to yield information about Earth's main magnetic field. This level of sensitivity is  
792 sufficient for detecting secular variations and geomagnetic jerks related to variations in the  
793 magnetic field at the Earth's core-mantle boundary. The Iridium Block 1 constellation data  
794 therefore offer the promise of revealing the global behavior of Earth's field on time scales  
795 shorter than ever before resolved.

796           The global coverage allows a tight constraint on geomagnetically quiet periods, yielding  
797 262 very quiet 24-hour intervals from the full dataset used for this study, spanning from January  
798 2010 through November 2015. To study the time behavior of the magnetic field patterns, the  
799 patterns from the quiet dataset were convolved with spherical harmonic orthogonal functions to  
800 directly calculate the cosine and sine harmonic function coefficients. The time series of these  
801 coefficients were then used to assess the time dependence of each component of the signal. This  
802 revealed both gradual variations in the field, indicative of a discrepancy in the predicted and  
803 actual secular variation of the field as well as a gradual acceleration of the field relative to a

804 secular variation, and shorter period variations matching annual and orbit local time precession  
805 periods. The precession and seasonal signals are attributed to artifacts in the magnetic field data  
806 arising from thermal gradients or other unidentified magnetic contaminations. Fourier analysis of  
807 the spherical harmonic coefficients allowed quantification and removal of these signals, as well  
808 as identification of components proportional to unphysical magnetic signals (i.e., the monopole  
809 term in the harmonic expansion). After removal of all of these artifacts, the patterns in the  
810 magnetic maps retained the basic features initially found in the original, registered data,  
811 indicating that these basic patterns are not readily associated with artificial signals. Because of  
812 the global nature of the observations, it is difficult to attribute the persistent geographically fixed  
813 patterns to external current systems.

814         The resultant reconstructed maps of perturbations over the 262 quiet intervals are a  
815 potential resource for study of the dynamics of Earth's magnetic field. The series of maps are  
816 essentially time series of magnetic field residuals at 800 virtual geomagnetic observatories (cf.  
817 *Mandea and Olsen, 2006; Olsen and Mandea, 2007*) albeit at an irregularly spaced set of quiet  
818 days. These time series represent what we consider to be the best data product of the Block 1  
819 Iridium magnetic field data for core field science. There are various potential values of this novel  
820 data product. First, it is an independent estimation of Earth's field that does not use the  
821 regularization techniques employed in other studies. Second, it provides global maps of the field  
822 on much shorter time scales than previously possible. Third, it can augment standard techniques  
823 for co-estimating the field as an additional regularization constraint, thereby potentially  
824 enhancing standard techniques for deriving the changes in Earth's core field.

825         There are of course limitations with this dataset owing to the fact that the Iridium Block 1  
826 instrumentation and spacecraft were never designed for high-precision science applications. Very

827 importantly, the approach as described here does not provide an estimate of the field intensity but  
828 yields only the shape of the field relative to the mean intensity of the model field used for the  
829 calibration step in the analysis. A co-estimation analysis might potentially overcome this  
830 limitation, but the stability of the magnetometer calibration is a major challenge as the  
831 magnetometers are not thermally stable or precisely calibrated instruments. Moreover, on-board  
832 calibrations were changed throughout the lifetime of the Block 1 satellites to update operational  
833 performance, but these calibration records are not complete. The corrections applied in this  
834 analysis subsume these calibration updates and do not provide a record of calibration stability.  
835 Additionally, artifact analysis performed in this study suggests that orbit variations in the  
836 temperature and/or thermal environment remained after the application of the pre-flight  
837 temperature calibration. However, analysis of the residual correlation with temperature indicated  
838 that there was no remaining signature of temperature dependence, and so the thermal  
839 environment behavior possibly contributing to artifacts in the dataset may be due to some other  
840 effect such as a temperature gradient. As seen in comparisons between the original, binned  
841 magnetic field residuals and the corrected, reconstructed residuals, the consistency of the  
842 patterns, independent of the set of satellites in different local times, points to a real, natural  
843 source for the coherency in the patterns rather than artifacts in the analysis.

844         Even with these substantial limitations in mind, the global nature of the observations and  
845 persistent consistency of the patterns suggest that future analyses with these data may prove  
846 valuable. First, the residual maps derived here can be compared against other main field  
847 estimates such as WMM, IGRF-2015, or CHAOS-6 and later generations of the CHAOS model.  
848 Comparison of the residuals from these models vis-à-vis IGRF-11 may provide insight into  
849 whether the present derived data products afford new useful information. Independent of these

850 comparisons, the short cadence and global coverage of the data product lends itself naturally to  
851 the study of the more rapid variations of the core-generated field, such as geomagnetic jerks. The  
852 dataset is particularly attractive for this application as it provides the first opportunity to  
853 characterize the global distribution of jerk signals to assess their temporal and spatial signatures  
854 independently.

855 Iridium NEXT data being collected for the continuation of the AMPERE dataset are  
856 presently in the calibration development phase, but the higher precision of the attitude sensors on  
857 the NEXT satellites suggest that the uncertainty due to attitude knowledge errors may be  
858 substantially lower. An assessment of the Iridium NEXT data for potential application to the  
859 continued study of the geomagnetic field is therefore future work that may be of great utility.

860

861 *Acknowledgements:* The collection and processing of data for AMPERE was supported by the  
862 National Science Foundation under grants ATM-0739864 and ATM-1420184 to The Johns  
863 Hopkins University Applied Physics Laboratory (JHU/APL). B. J. Anderson is grateful for  
864 support for this work from JHU/APL Sabbatical Fellowship program for analysis support in  
865 coordination with the Department of Earth and Planetary Sciences of The Johns Hopkins  
866 University. The data and data products used for this study are posted via the AMPERE facility  
867 server via <http://ampere.jhuapl.edu> and include the Iridium residuals relative to IGRF-11 as well  
868 as the vector magnetic residuals corresponding to the 800 virtual geomagnetic observatories for  
869 each of the 262 24-hour quiet intervals generated for the study. This research project (or part of  
870 this research project) was conducted using computational resources (and/or scientific computing  
871 services) at the Maryland Advanced Research Computing Center (MARCC).

872

873 **References**

- 874 Acuña, M. H (2002), Space-based magnetometers, *Rev. Sci. Instr.*, **73**, 3717-3736,  
875 doi:10.1063/1.1510570.
- 876 Alken, P., N. Olsen, and C. C. Finlay (2020), Co-estimation of geomagnetic field and in-orbit  
877 fluxgate magnetometer calibration parameters, *Planets and Space*, **72:49**,  
878 doi:10.1186/s40623-020-01163-9.
- 879 Anderson, B. J., K. Takahashi, B. A. Toth (2000), Sensing global Birkeland currents with  
880 Iridium® engineering magnetometer data, *Geophys. Res. Lett.*, **27**, 4045-4048.
- 881 Anderson, B. J., H. Korth, C. L. Waters, D. L. Green, and P. Stauning (2008), Statistical  
882 Birkeland current distributions from magnetic field observations by the Iridium constellation,  
883 *Annales Geophys.*, **26**, 671-687, doi:10.5194/angeo-26-671-2008.
- 884 Anderson, B. J., H. Korth, C. L. Waters, D. L. Green, V. G. Merkin, R. J. Barnes, and L. P.  
885 Dyrud (2014), Development of large-scale Birkeland currents determined from the Active  
886 Magnetosphere and Planetary Electrodynamics Response Experiment, *Geophys. Res. Lett.*,  
887 **41**, 3017-3025, doi:10.1002/2014GL059941.
- 888 Anderson, B. J., C. N. Olson, H. Korth, R. J. Barnes, C. L. Waters, and S. K Vines (2018),  
889 Temporal and spatial development of global Birkeland currents, *J. Geophys. Res. Space*  
890 *Physics*, **123**, JGRA54317, doi:10.1029/2018JA025254.
- 891 Aubert, J. and C. C. Finlay (2019), Geomagnetic jerks and rapid hydromagnetic waves focusing  
892 at Earth's core surface, *Nature Geo. Sci.*, **12**, 393–398, doi:10.1038/s41561-019-0355-1.
- 893 Aubert J., J. A. Tarduno, and C. L. Johnson (2010), Observations and Models of the Long-Term  
894 Evolution of Earth's Magnetic Field, *Space Sci. Rev.*, **155**, 337-370, doi:10.1007/s11214-010-  
895 9684-5.

896 Baumjohann, W. and R. Nakamura (2009), Magnetospheric contributions to the terrestrial  
897 magnetic field, in *Treatise on Geophysics*, ed. by M. Kono, G. Schubert, Elsevier,  
898 Amsterdam, pp. 77–92.

899 Bloxham, J., Zatman, S., & Dumberry, M. (2002). The origin of geomagnetic jerks. *Nature*,  
900 420(6911), 65–68. doi:10.1038/nature01134.

901 Brown, W. J., J. E. Mound, and P. W. Livermore (2013), Jerks abound: An analysis of  
902 geomagnetic observatory data from 1957 to 2008. *Phys. Earth Planet. Inter.* **223**, 62–76,  
903 doi:10.1016/j.pepi.2013.06.001.

904 Buffet, B., N. Knezek, and R. Holme (2016), Evidence for MAC waves at the top of Earth’s core  
905 and implications for variations in length of day, *Geophys. J. Int.*, **204**, 1789–1800,  
906 doi:10.1093/gji/ggv552.

907 Chulliat, A., W. Brown, P. Alken, C. Beggan, M. Nair, G. Cox, A. Woods, S. Macmillan, B.  
908 Meyer, and M. Panizza, The US/UK World Magnetic Model for 2020-2025: Technical  
909 Report, National Centers for Environmental Information, NOAA, doi:10.25923/ytk1-yx35,  
910 2020.

911 Civet, F., E. Thébault, O. Verhoeven, B. Langlais, and D. Saturnino (2015), Electrical  
912 conductivity of the Earth’s mantle from the first Swarm magnetic field measurements,  
913 *Geophys. Res. Lett.*, **42**, 3338–3346, doi:10.1002/2015GL063397.

914 Clausen, L. B. N., J. B. H. Baker, J. M. Ruohoniemi, S. E. Milan, and B. J. Anderson (2012),  
915 Dynamics of the region 1 Birkeland current oval derived from the Active Magnetosphere and  
916 Planetary Electrodynamics Response Experiment (AMPERE), *J. Geophys. Res.*, **117**,  
917 A06233, doi:10.1029/2012JA017666.

918 Coxon, J. C., S. E. Milan, and B. J. Anderson (2018), A Review of Birkeland Current Research  
919 using AMPERE, in *Electric Currents in Geospace and Beyond, Geophysical Monograph*  
920 *235*, eds. A. Keiling, O. Marghitu, and M. Wheatland, American Geophysical Union, John  
921 Wiley & Sons, Inc., ISBN:978-1-119-32449-2.

922 Finlay C. C., M. Dumberry, A. Chulliat, and M. A. Pais (2010a), Short Timescale Core  
923 Dynamics: Theory and Observations, *Space Sci. Rev.*, **155**, 177-218, doi:10.1007/s11214-  
924 010-9691-6.

925 Finlay, C. C., S. Maus, C. D. Beggan, et al. (2010b), International Geomagnetic Reference Field:  
926 the eleventh generation, *Geophys. J.*, **183**, 1216-1230, doi: 10.1111/j.1365-  
927 246X.2010.04804.x.

928 Finlay C. C., N. Olsen, S. Kotsiaros, N. Gillet, and L. Tøffner-Clausen (2016), Recent  
929 geomagnetic secular variation from Swarm and ground observatories as estimated in the  
930 CHAOS-6 geomagnetic field model, *Earth, Planets and Space*, 68:112, doi:10.1186/s40623-  
931 016-0486-1.

932 Finlay, C.C., C. Kloss, N. Olsen, M. Hammer, L. Toeffner-Clausen, A. Grayver, and A.  
933 Kuvshinov (2020), The CHAOS-7 geomagnetic field model and observed changes in the  
934 South Atlantic Anomaly, *Earth Planets and Space*, **72**, doi:10.1186/s40623-020-01252-9.

935 Hori, K., C. A. Jones, and R. J. Teed (2015), Slow magnetic Rossby waves in the Earth's core,  
936 *Geophys. Res. Lett.*, **42**, 6622–6629, doi:10.1002/2015GL064733.

937 Hulot, G., C.C. Finlay, C. G. Constable, N. Olsen, and M. Manda (2010), The Magnetic Field  
938 of Planet Earth, *Space Sci. Rev.*, **152**: 159–222, doi:10.1007/s11214-010-9644-0.

939 Iijima, T., and T. A. Potemra (1976), The amplitude distribution of field-aligned currents at  
940 northern high latitudes observed by Triad, *J. Geophys. Res.*, **81**, 2165-2174.

941 Knipp, D. J., T. Matsuo, L. Kilcommons, A. Richmond, B. Anderson, H. Korth, R. Redmon, B.  
942 Mero, and N. Parrish (2014), Comparison of magnetic perturbation data from LEO satellite  
943 constellations: Statistics of DMSP and AMPERE, *Space Weather*, **12**, 2-23,  
944 doi:10.1002/2013SW000987.

945 Langel, R., G. Ousley, J. Berbert, J. Murphy, and M. Settle (1982), The MAGSAT mission,  
946 *Geophys. Res. Lett.*, **9**, 243-245, doi:10.1029/GL009i004p00243.

947 Langlais, B., V. Lesur, M. E. Purucker, J. E. Connerney, and M. Madnea (2010), Crustal  
948 Magnetic Fields of Terrestrial Planets, *Space Sci. Rev.*, **152**, 223-249, doi:10.1007/s11214-  
949 009-9557-y.

950 Lühr, H., G. N. Kervalishvili, C. Stolle, J. Rauberg, and I. Michaelis, (2019), Average  
951 characteristics of low-latitude interhemispheric and F region dynamo currents deduced from  
952 the swarm satellite constellation, *J. Geophys. Res.: Space Phys.*, **124**,  
953 doi:10.1029/2019JA027419.

954 Lyatskaya, S., G. V. Khazanov, and E. Zesta (2014), Interhemispheric field-aligned currents:  
955 Simulation results, *J. Geophys. Res.: Space Phys.*, **119**, 5600–5612,  
956 doi:10.1002/2013JA019558.

957 Manda, M., R. Holme, A. Pais, K. Pinheiro, A. Jackson, and G. Verbanac (2010), Geomagnetic  
958 jerks: Rapid core field variations and core dynamics, *Space Sci. Rev.*, **155**, 147–175,  
959 doi:10.1007/s11214-010-9663-x.

960 Manda, M., and M. Purucker (2018), The Varying Core Magnetic Field from a Space Weather  
961 Perspective, *Space Sci. Rev.*, **214**:11, doi:10.1007/s11214-017-0443-8.

962 Milan, S. E., L. B. N. Clausen, J. C. Coxon, J. A. Carter, M.-T. Walach, K. Laundal, N.  
963 Østgaard, P. Tenfjord, J. Reistad, K. Snekvik, H. Korth, and B. J. Anderson (2017),

964 Overview of Solar Wind–Magnetosphere–Ionosphere–Atmosphere Coupling and the  
965 Generation of Magnetospheric Currents, *Space Sci. Rev.*, **206**, 547–573, doi:10.1007/s11214-  
966 017-0333-0.

967 Manda, M. and N. Olsen (2006), A new approach to directly determine the secular variation from  
968 magnetic satellite observations, *Geophys. Res. Lett.* **33**, 1–5, doi:10.1029/2006GL026616.

969 Olsen, N. and M. Manda (2007), Investigation of a secular variation impulse using satellite data: The  
970 2003 geomagnetic jerk. *Earth Planet. Sci. Lett.*, **255**, 94–105, doi: 10.1016/j.epsl.2006.12.008.

971 Olsen, N., D. Ravat, C. C. Finlay and L. K. Kother (2017), LCS-1: a high-resolution global  
972 model of the lithospheric magnetic field derived from CHAMP and Swarm satellite  
973 observations, *Geophys. J. Int.*, **211**, 1461-1477, doi:10.1093/gji/ggx381.

974 Olsen, N., G. Hulot, and T. J. Sabaka (2010), Measuring the Earth’s Magnetic Field from Space:  
975 Concepts of Past, Present and Future Missions, *Space Sci. Rev.*, **155**, 65–93,  
976 doi:10.1007/s11214-010-9676-5.

977 Olsen, N., et al. (2013), The Swarm Satellite Constellation Application and Research Facility  
978 (SCARF) and Swarm data products, *Earth Planets Space*, **65**, 1189–1200,  
979 doi:10.5047/eps.2013.07.001.

980 Olsen N., C. C. Finlay , S. Kotsiaros, and L. Tøffner-Clausen (2016), A model of Earth’s  
981 magnetic field derived from 2 years of Swarm satellite constellation data, *Earth, Planets and*  
982 *Space*, 68:124, doi:10.1186/s40623-016-0488-z.

983 Olsen, N. and C. Stolle (2017), Magnetic Signatures of Ionospheric and Magnetospheric Current  
984 Systems During Geomagnetic Quiet Conditions - An Overview, *Space Sci. Rev.*, **206**, 5–25,  
985 doi:10.1007/s11214-016-0279-7.

986 Plaschke, F., H.-U. Auster, D. Fischer, K.-H. Fronacon, W. Magnes, I. Richter, D.  
987 Constantinescu, and Y. Nartita (2019), Advanced calibration of magnetometers on spin-

988 stabilized spacecraft based on parameter decoupling, *Geosci. Instrum. Method. Data Syst.*, **8**,  
989 63–76, 2019, <https://doi.org/10.5194/gi-8-63-2019>.

990 Raeder, J., W.D. Cramer, K. Germaschewski, and J. Jensen (2017), Using OpenGGCM to  
991 Compute and Separate Magnetosphere Magnetic Perturbations Measured on Board Low  
992 Earth Orbiting Satellites, *Space Sci. Rev.*, **206**, 601–620, doi:10.1007/s11214-016-0304-x.

993 Roberts, P. H. and E. M. King (2013), On the genesis of the Earth's magnetism, *Rep. Prog.*  
994 *Phys.*, **76**, eid:096801 (55pp), doi:10.1088/0034-4885/76/9/096801.

995 Sabaka T. J., L. Tøffner-Clausen, N. Olsen, and C. C. Finlay (2018), A comprehensive model of  
996 Earth's magnetic field determined from 4 years of Swarm satellite observations, *Earth,*  
997 *Planets and Space* 70:130, doi:10.1186/s40623-018-0896-3.

998 Waters, C. L., B. J. Anderson, and K. Liou (2001), Estimation of global field aligned currents  
999 using Iridium magnetometer data, *Geophys. Res. Lett.*, **28**, 2165-2168,  
1000 doi:10.1029/2000GL012725.

1001 Waters, C. L., B. J. Anderson, D. L. Green, H. Korth, R. J. Barnes and H. Vanhamäki (2020),  
1002 Science Data Products for AMPERE, in *Ionospheric Multi-Spacecraft Analysis Tools, ISSI*  
1003 *Scientific Report Series 17*, M. W. Dunlop and H. Lühr (eds.), pp. 141-165, doi:10.1007/978-  
1004 3-030-26732-2\_7.

1005 Witze, A. (2019), Earth's magnetic field is acting up and geologists don't know why, *Nature*,  
1006 **565**, 143-144, doi:10.1038/d41586-019-00007-1.

1007 Yamazaki, Y. and A. Maute (2017), Sq and EEJ - A Review on the Daily Variation of the  
1008 Geomagnetic Field Caused by Ionospheric Dynamo Currents, *Space Sci. Rev.*, **206**, 299–405,  
1009 doi:10.1007/s11214-016-0282-z.

## Figures



**Figure 1.** Schematic depiction of Block 1 Iridium Communications satellite communications network configuration in low Earth orbit (LEO) at 780 km altitude and  $86^\circ$  inclination. The satellites are configured in six orbit planes with 11 satellites in each plane constituting the communication network from which magnetometer data were acquired for AMPERE beginning 1 Jan 2010. The light blue solid lines are the orbit planes and the yellow dashed lines depict the radio links between orbit planes.

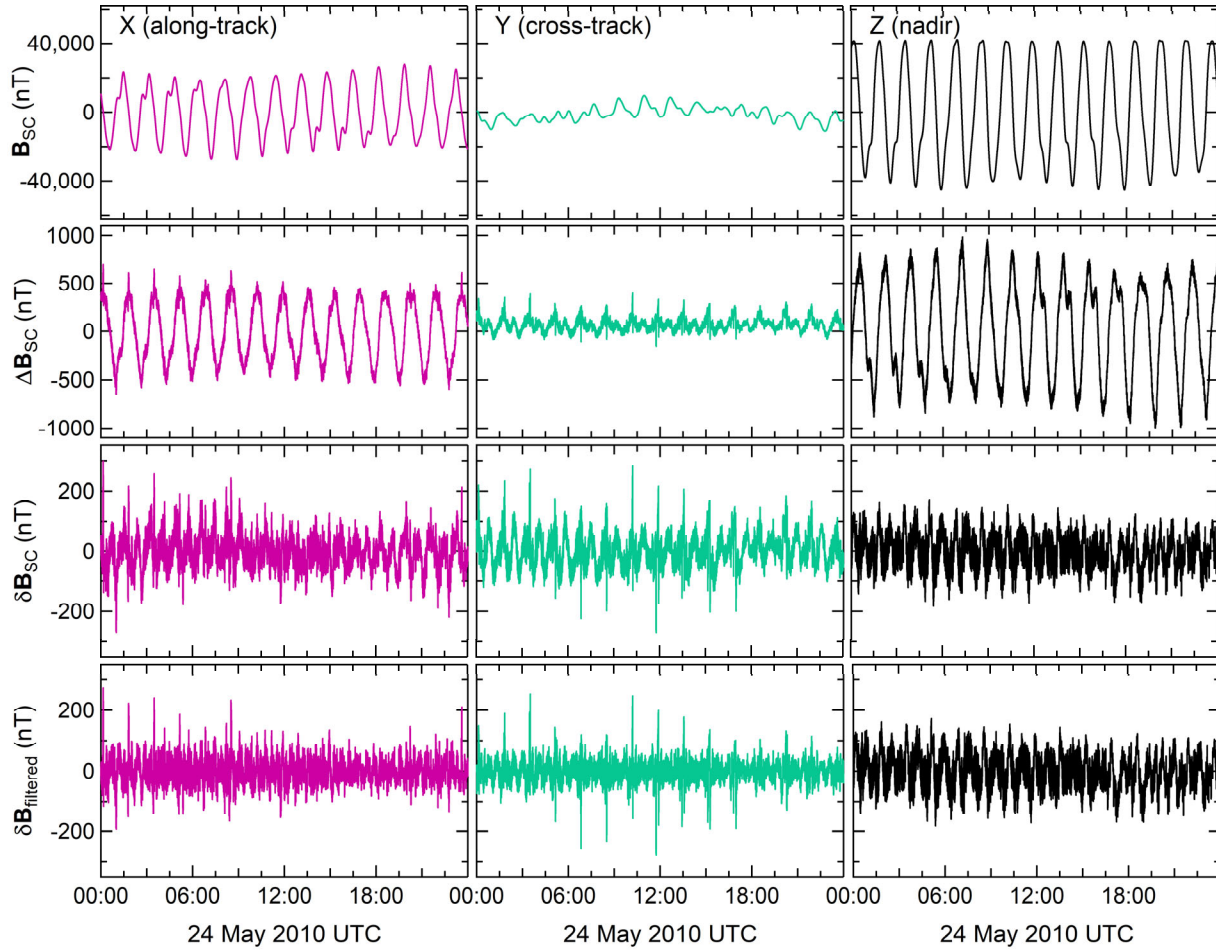


**Figure 2.** One day of data from Iridium Satellite Vehicle 30 (denoted SV030) in satellite body coordinates showing results at four stages of data processing. From left to right: the columns show the magnetic field components in the X-axis (along track in the ram direction, parallel to the satellite velocity,  $\mathbf{v}$ , in magenta); Y-axis (cross track in the  $\mathbf{v} \times \mathbf{r}$  direction, in turquoise); and Z-axis (nadir,  $-\mathbf{r}$  direction, in black). From top to bottom, the rows show: magnetometer readings converted to engineering units,  $\mathbf{B}_{SC}$ ; magnetic field residual after subtracting the IGRF-2010 model with secular variations ( $\mathbf{B}_{IGRF}$ ),  $\Delta\mathbf{B}$ ; residual corrected for offsets, misalignment, and orientation using multi-linear regression between  $\Delta\mathbf{B}$  and  $\mathbf{B}_{IGRF}$ ,  $\delta\mathbf{B}$ ; and the corrected residual after applying a high-pass filter with a cut-off period of 25 minutes ( $\sim 1/4$  of an orbit period),  $\delta\mathbf{B}_{filtered}$ .

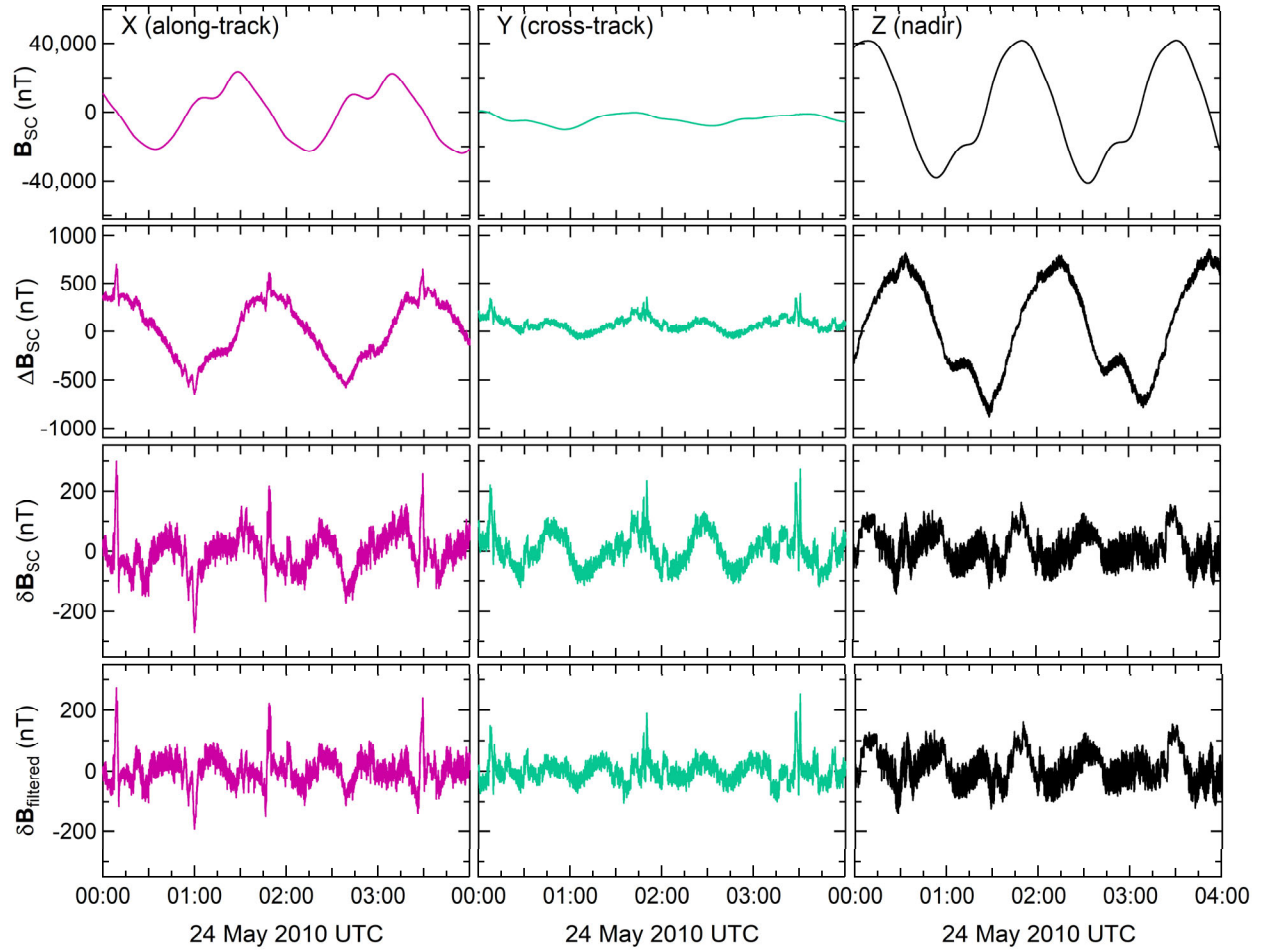


**Figure 3.** Magnetic field data from Iridium Satellite Vehicle 30 (SV030) for the first four hours of 24 May 2010 in the same format as **Figure 2**, showing slightly more than two orbits of data. The residual signals in  $\delta\mathbf{B}$  show signals occurring over roughly an orbit period and twice an orbit period, most clearly in the along-track and cross-track components. Short-period spikes in the along and cross-track components most evident in the  $\delta\mathbf{B}_{\text{filtered}}$  time series at  $\sim 00:08$  UT,  $\sim 01:00$  UT,  $\sim 01:45$  UT, and  $\sim 03:25$  UT are due to Birkeland currents.

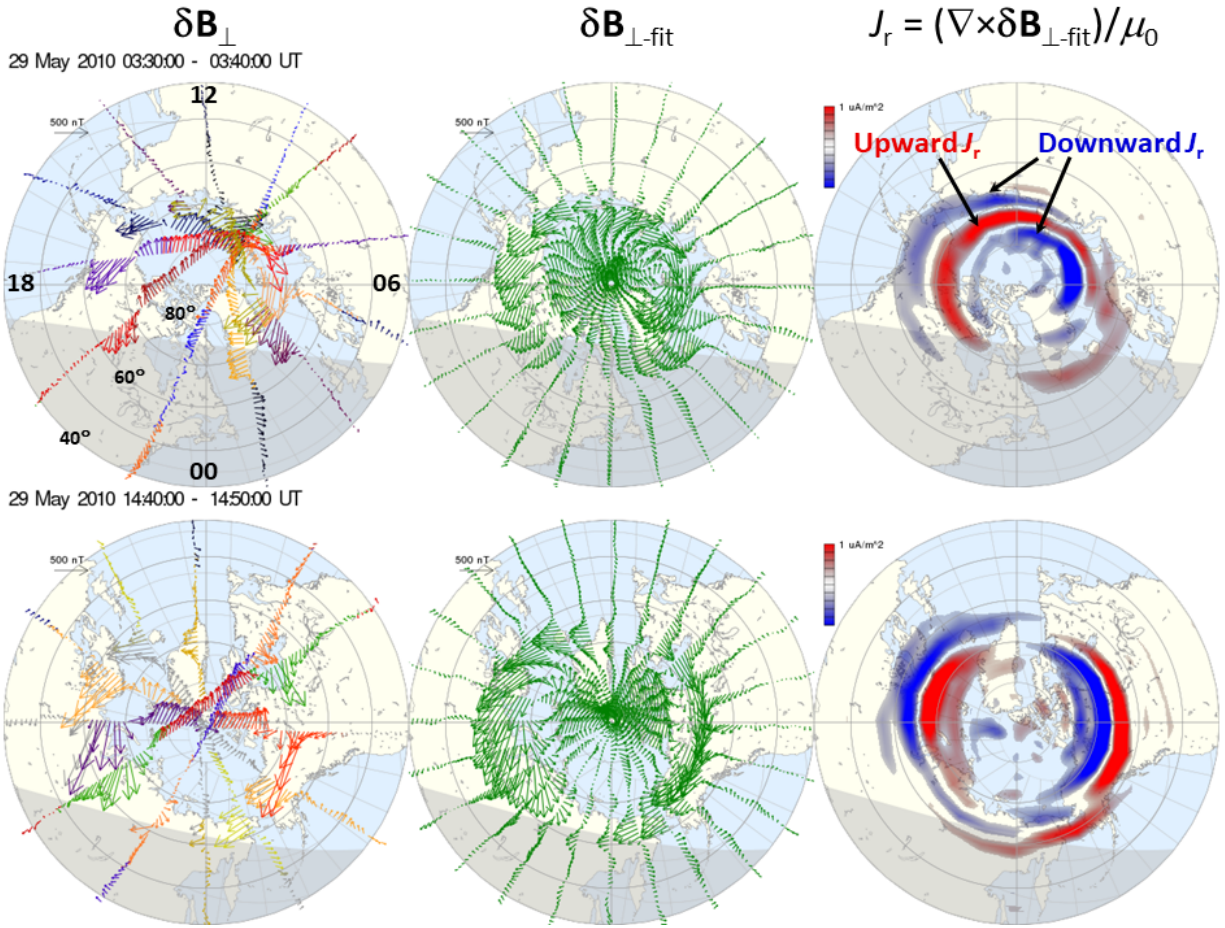


**Figure 4.** Example 10-minute intervals of AMPERE processing steps and products from two intervals during geomagnetic activity on 29 May 2010, 03:30-03:40 UT (top) and 12:00-12:10 UT (bottom). Panels show the view looking down from above the north magnetic pole to 40° magnetic latitude, with magnetic noon at the top and dusk to the left. (Left) horizontal magnetic perturbations ( $\delta\mathbf{B}_{\perp}$ ) along each orbit track, with arrows colored differently for different satellites in the direction of  $\delta\mathbf{B}_{\perp}$  and scaled by 500 nT; (middle) continuous fit to the  $\delta\mathbf{B}_{\perp}$  data ( $\delta\mathbf{B}_{\perp\text{-fit}}$ ) using harmonic functions customized to be normalized over the latitude range shown and evaluated at every hour in local time and degree in latitude; (right) radial electric current density,  $J_r$ , calculated as  $\nabla \times \delta\mathbf{B}_{\perp\text{-fit}} / \mu_0$ , where red is upward (positive)  $J_r$ , blue is downward (negative)  $J_r$ , and the color saturation is set to 1  $\mu\text{A}/\text{m}^2$ .

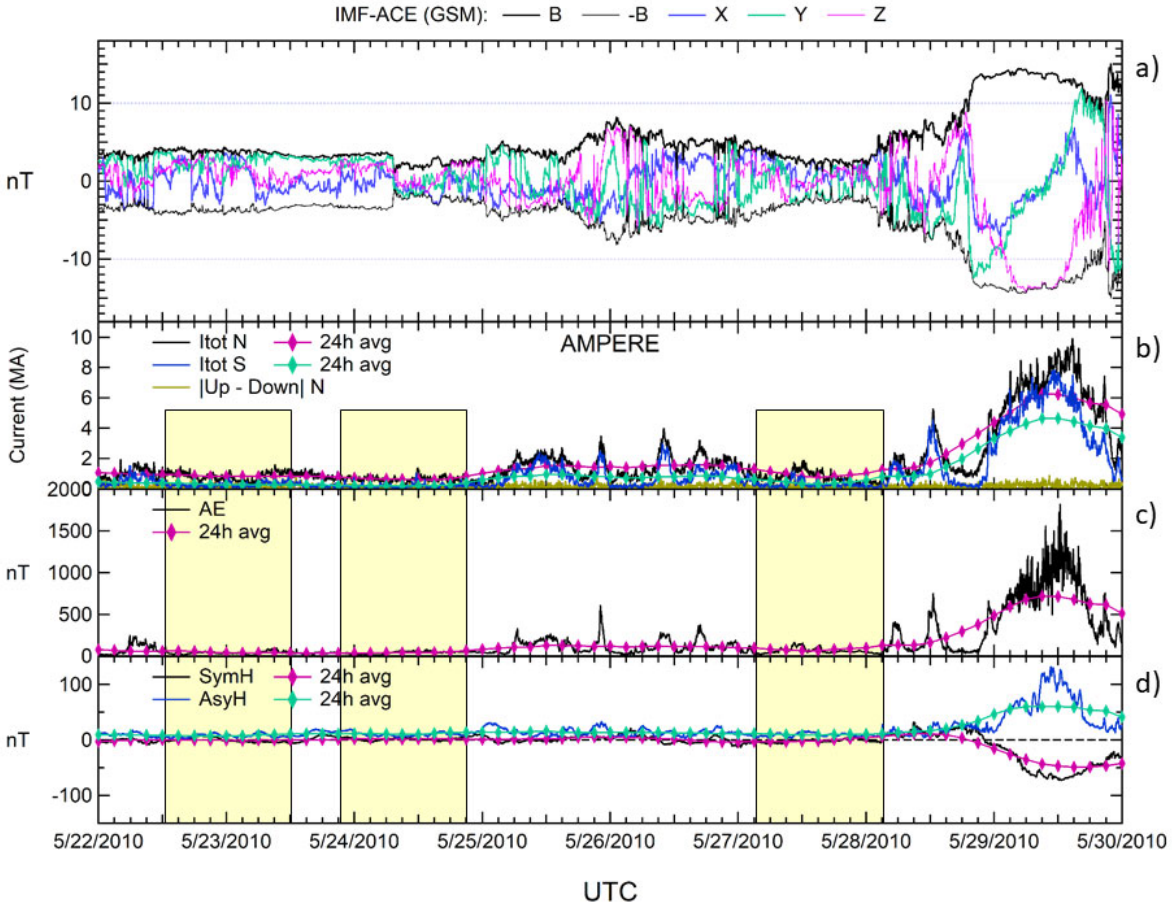


**Figure 5.** Eight-day interval of the parameters and sliding 24-hour averages used to identify geomagnetically quiet intervals, together with the interplanetary magnetic field (IMF) observed by the Advanced Composition Explorer (ACE) spacecraft at the Earth-Sun Lagrange point 1 (L1). From top to bottom the panels show: (a) IMF data; (b) total Birkeland currents ( $I_{tot}$ ) in the northern (black) and southern (blue) hemisphere and their running 24-hour averages together with the net current (magenta, torquoise, and gold lines, respectively); (c) auroral electrojet (AE) index (black) and its running 24-hour average (magenta); (d) symmetric (SymH) and asymmetric (AsyH) H-indices (black and blue, respectively) and their 24-hour running averages (magenta and turquoise, respectively). Three of the quiet periods occurred during this interval and are indicated by the yellow boxes in the bottom three panels: 2010-05-22/12:00 – 2010-05-23/12:00; 2010-05-23/21:00 – 2010-05-24/21:00; and 2010-05-27/03:00 – 2010-05-28/03:00.

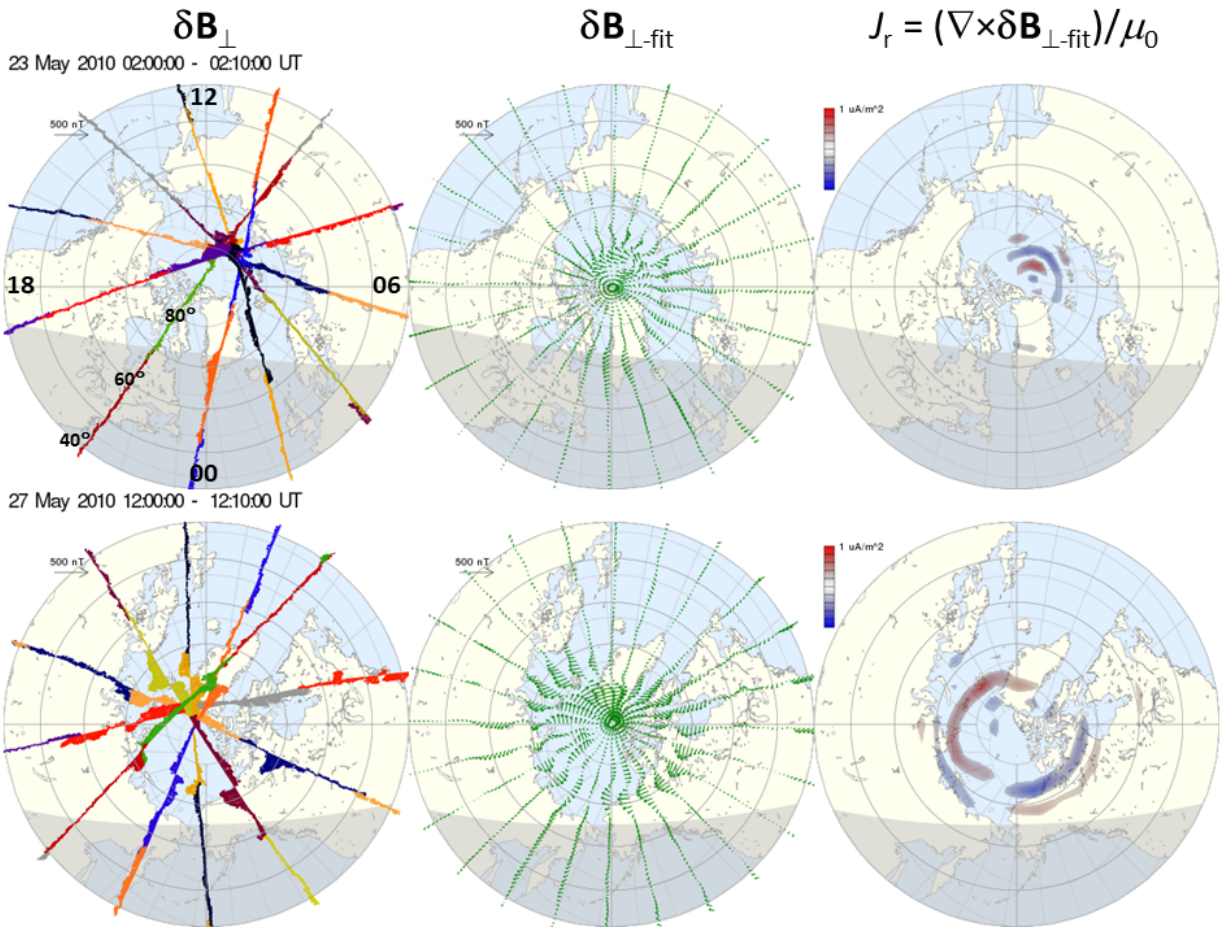


**Figure 6.** Example 10-minute intervals of AMPERE products in the same format as **Figure 4** from 23 May 2010 at 02:00-02:10 UT (top) during the quietest 24-hour period in **Figure 5** and 27 May 2010 at 12:00-12:10 UT (bottom) during the most active interval during the third quiet 24-hour period in **Figure 5**.

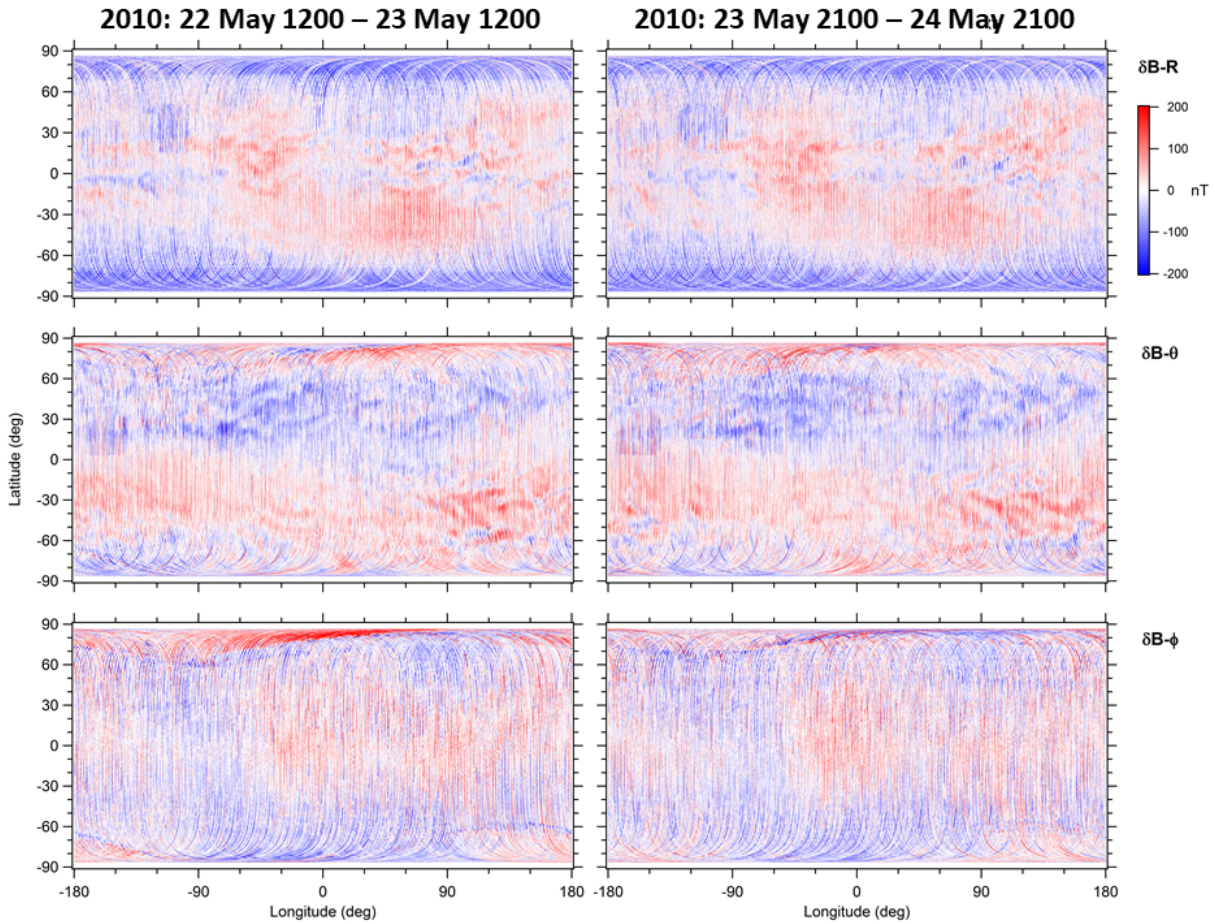


**Figure 7.** Calibrated magnetic field residuals from all Iridium Block 1 satellites in geographic spherical coordinates versus geographic latitude and longitude for 2010-05-22/12:00 – 2010-05-23/12:00 on the left and 2010-05-23/21:00 – 2010-05-24/21:00 on the right. The panels show all of the samples from every satellite,  $\sim 290,000$  points, plotted as colored dots. From top to bottom the panels show  $\delta B_r$ ,  $\delta B_\theta$ , and  $\delta B_\phi$ , all using the same color scale.

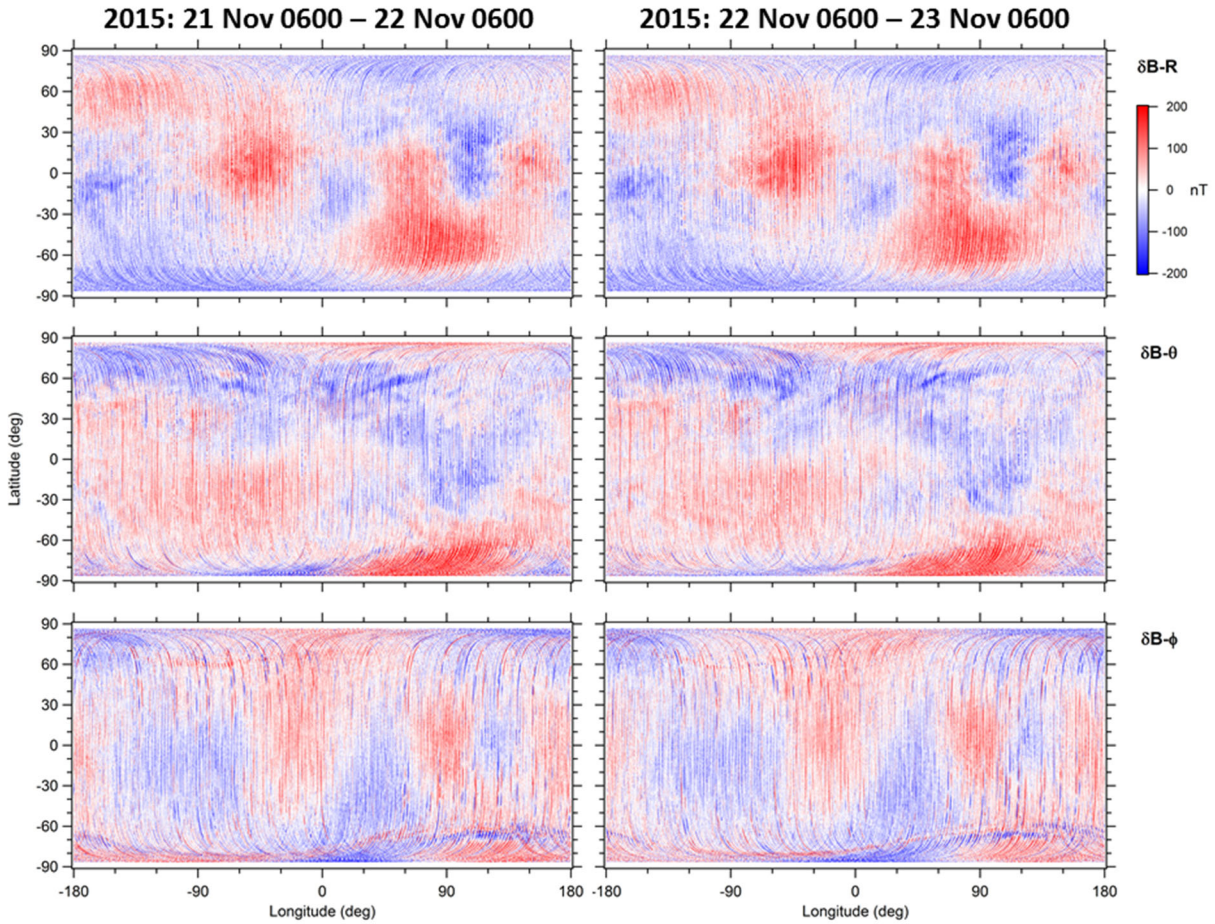


**Figure 8.** Calibrated magnetic field residuals from all Iridium Block 1 satellites in the same format as **Figure 7** for 2015-11-21/06:00 – 2015-11-22/06:00 on the left and 2015-11-22/06:00 – 2015-11-23/06:00 on the right. As for Figure 7, but more evident here owing to the larger residual magnitudes, the dots are small enough that the white space between tracks of points are predominantly blank spaces between tracks of samples.

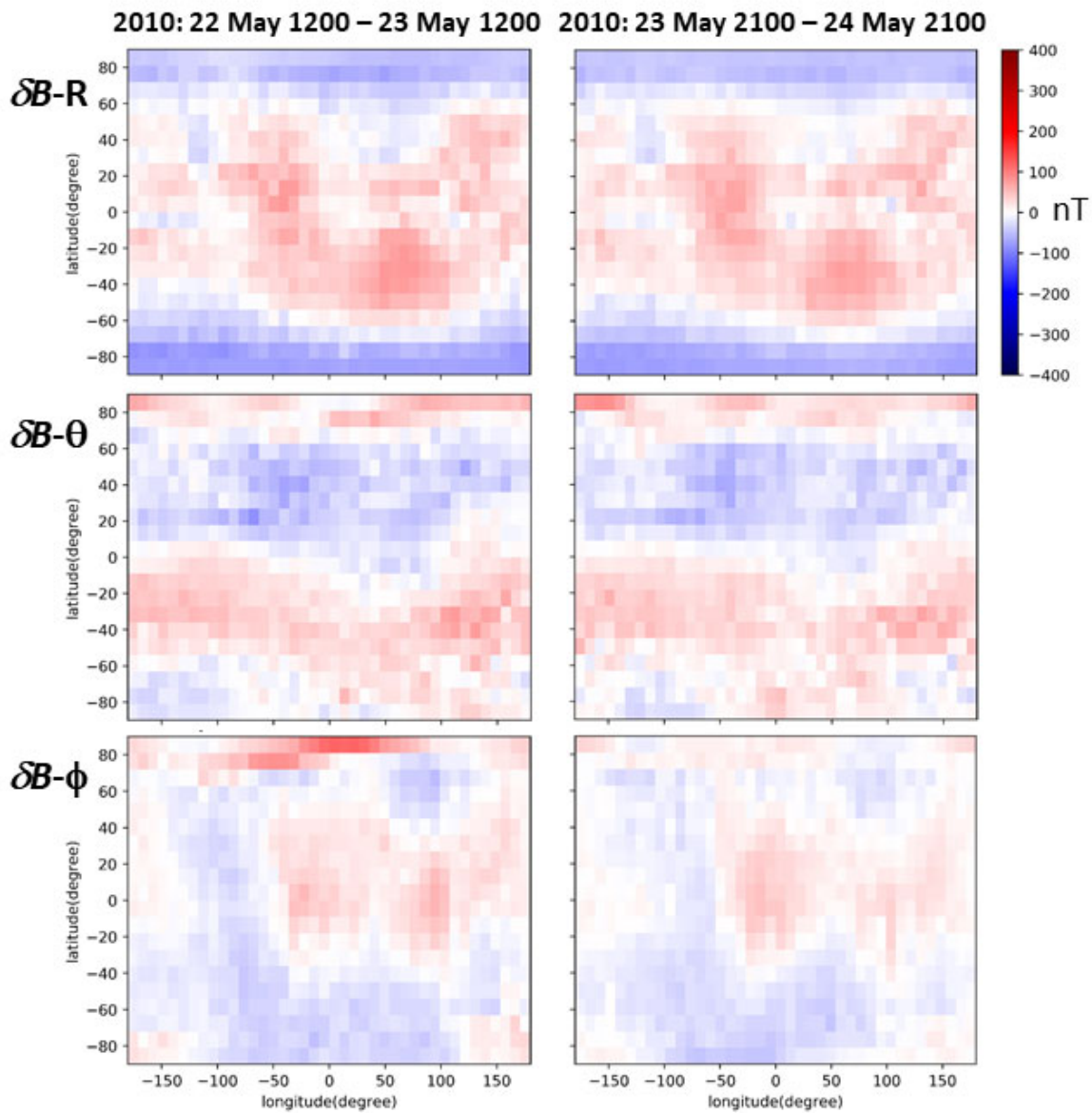


**Figure 9.** Global maps of averaged magnetic field residuals relative to IGRF-11 in geographic spherical coordinates from all Iridium Block 1 satellite observations in  $9^\circ$  by  $9^\circ$  latitude-longitude bins. Left panels show results for the 24-hour quiet period starting at 12:00 UT on 22 May 2010 and the right panels show results for the 24-hour quiet period immediately following, starting at 21:00 UT on 23 May 2010.

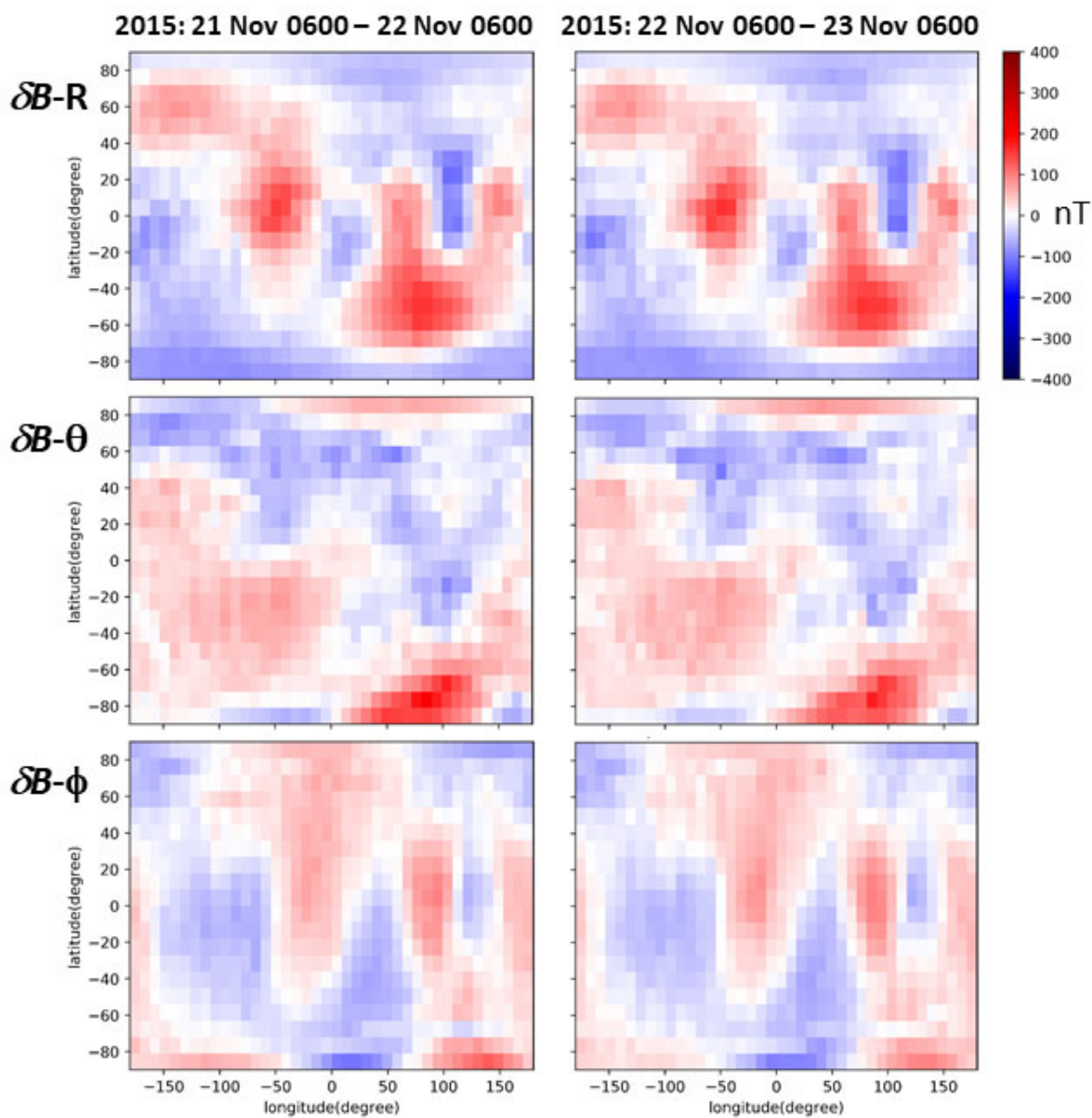


**Figure 10.** Global maps of averaged magnetic field residuals in the same format as Figure 9. Left panels show results for the 24-hour quiet period starting at 06:00 UT on 21 November 2015 and the right panels show results for the next 24-hour quiet period, starting at 06:00 UT on 22 November 2015.

2015: 21 Nov 0600 - 22 Nov 0600

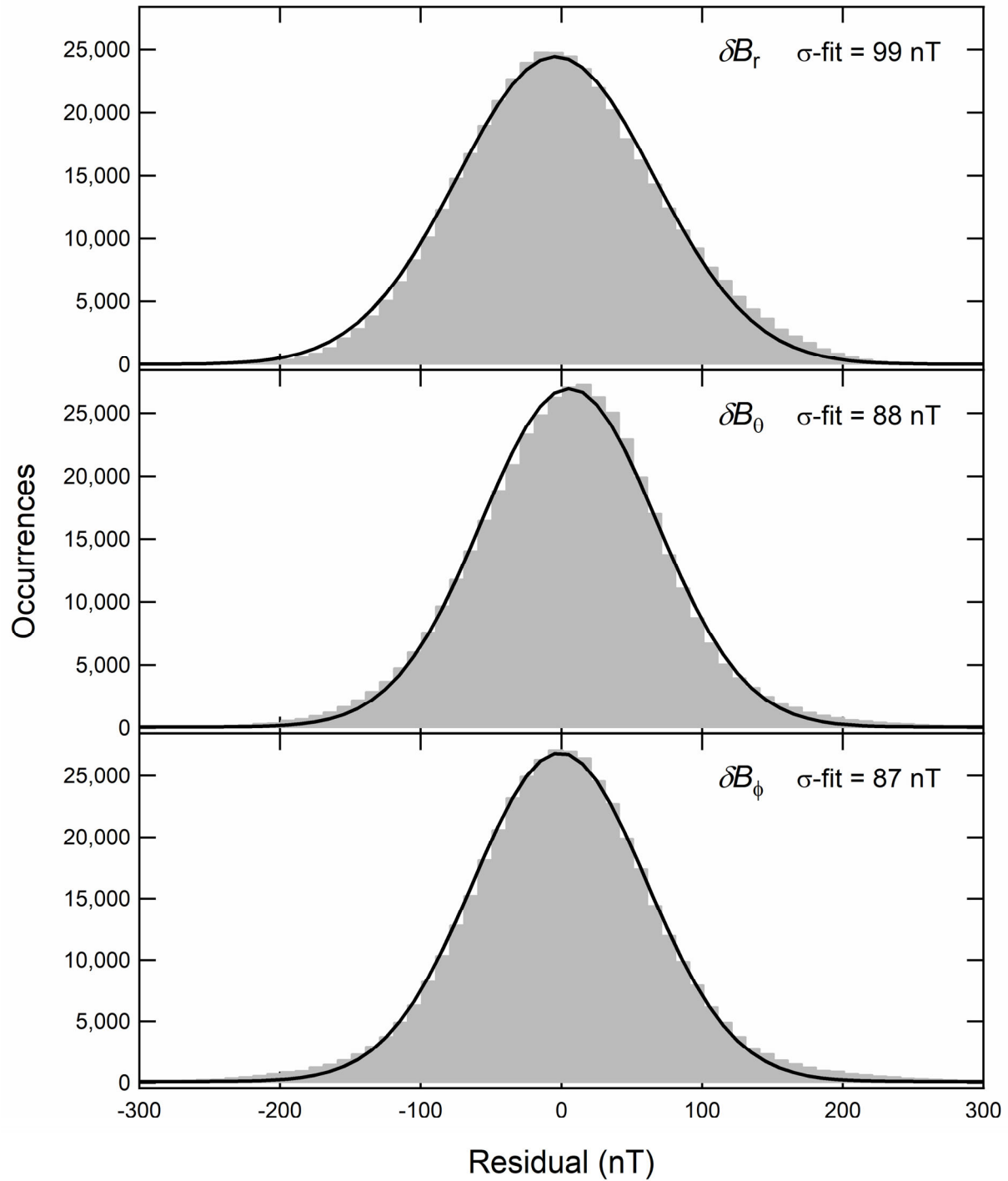


**Figure 11.** Histogram distributions of residuals for  $\delta B_r$ ,  $\delta B_0$ , and  $\delta B_\phi$  for the geomagnetically quiet period from 2015-11-21/06:00 to 2015-11-22/06:00. The probability distribution for each component (gray bars) is fit with a Gaussian distribution (black line). The standard deviation of each fits is given in each panel.

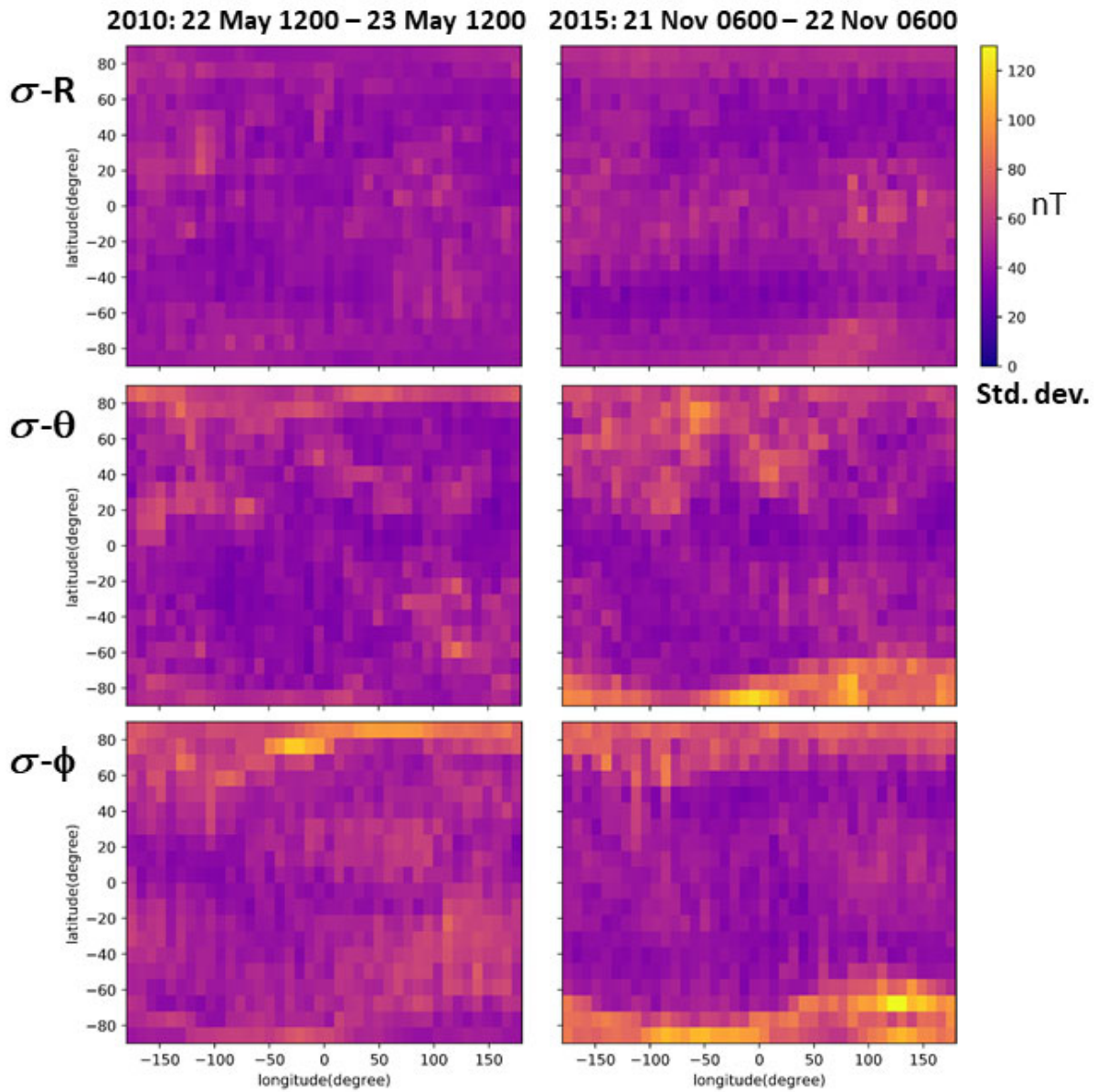


**Figure 12.** Standard deviations,  $\sigma$ , of the magnetic field residuals within each latitude-longitude bin for the 2010-05-22/12:00 – 2010-05-23/12:00 (left panels) and 2015-11-21/06:00 – 2015-11-22/06:00 quiet intervals (right panels). The standard deviation value for each component for both quiet periods is indicated by the color scale.

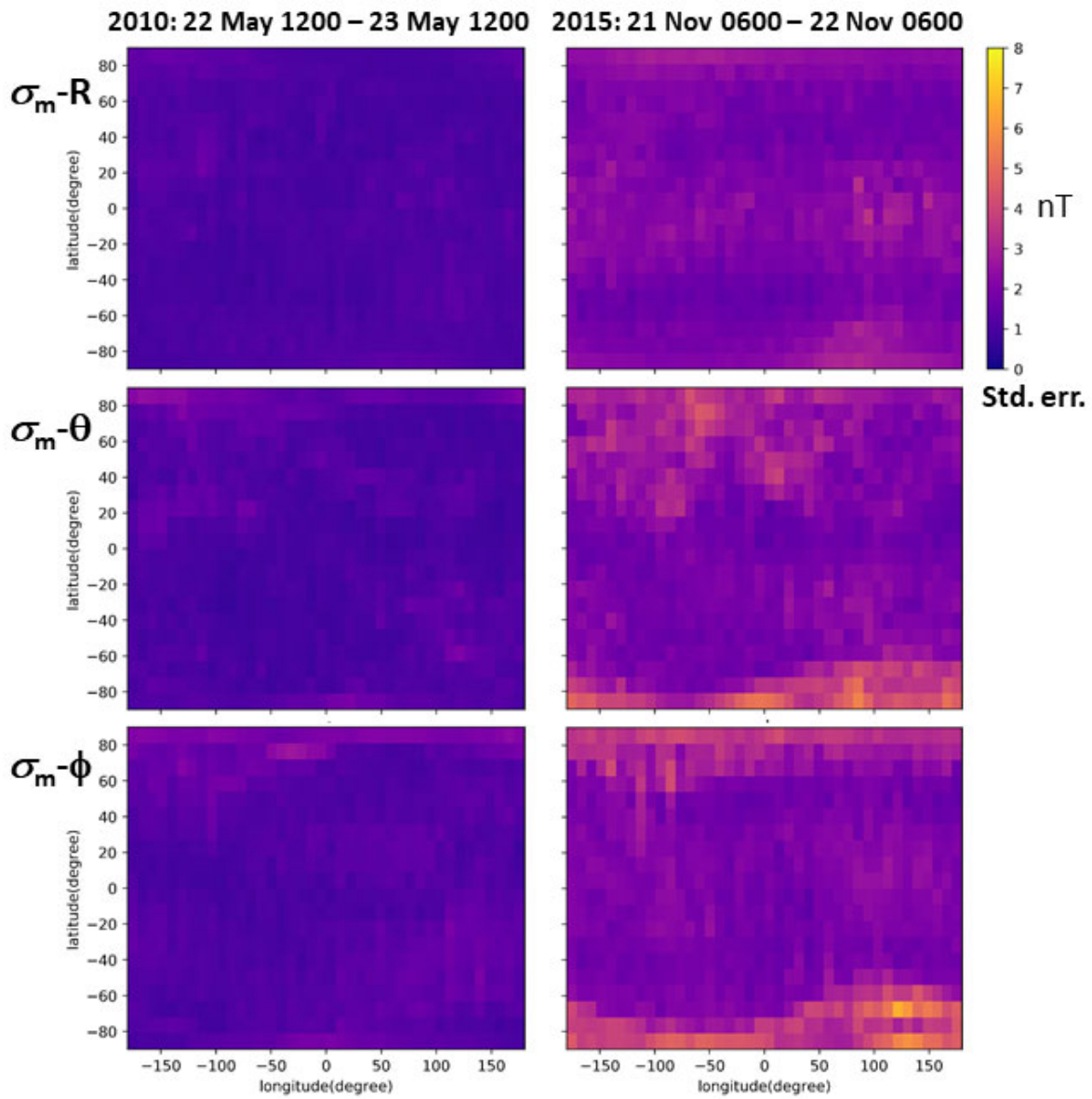


**Figure 13.** Standard error of the mean,  $\sigma_m$ , of the averaged magnetic field residuals within each latitude-longitude bin for the 2010-05-22/12:00 – 2010-05-23/12:00 (left panels) and 2015-11-21/06:00 – 2015-11-22/06:00 quiet intervals (right panels). The standard error value for each component for both quiet periods is indicated by the color scale.

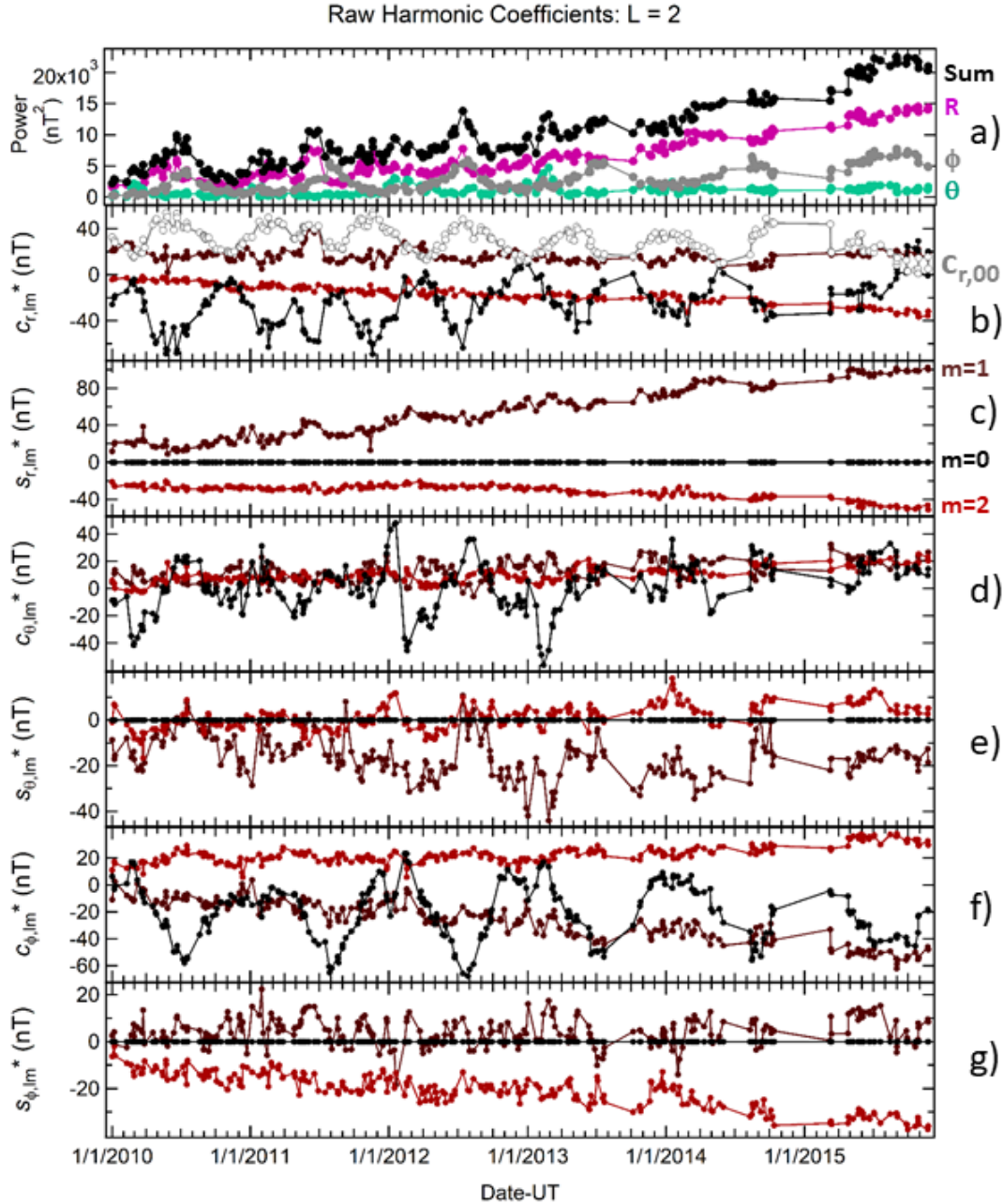


**Figure 14.** Time series of the spherical harmonic coefficients  $c_{lm}(t_i)$  and  $s_{lm}(t_i)$  for  $l = 2$ . Top panel (a) shows the total power in  $nT^2$  summed over  $m = 0, 1,$  and  $2$  for all components (black),  $r$  only (magenta),  $\theta$  only (turquoise), and  $\phi$  only (gray). The bottom six panels show in order from top:  $C_{r,lm}$ ,  $S_{r,lm}$  (b and c),  $C_{0,lm}$ ,  $S_{0,lm}$  (d and e), and  $C_{\phi,lm}$ ,  $S_{\phi,lm}$  (f and g). The color coding in the bottom six panels are black for  $m = 0$ , dark red for  $m = 1$ , and lighter red for  $m = 2$ . Panel 2 also shows the  $l = 0$  cosine coefficient,  $c_{r00}$ , in gray, which is an unphysical signal.

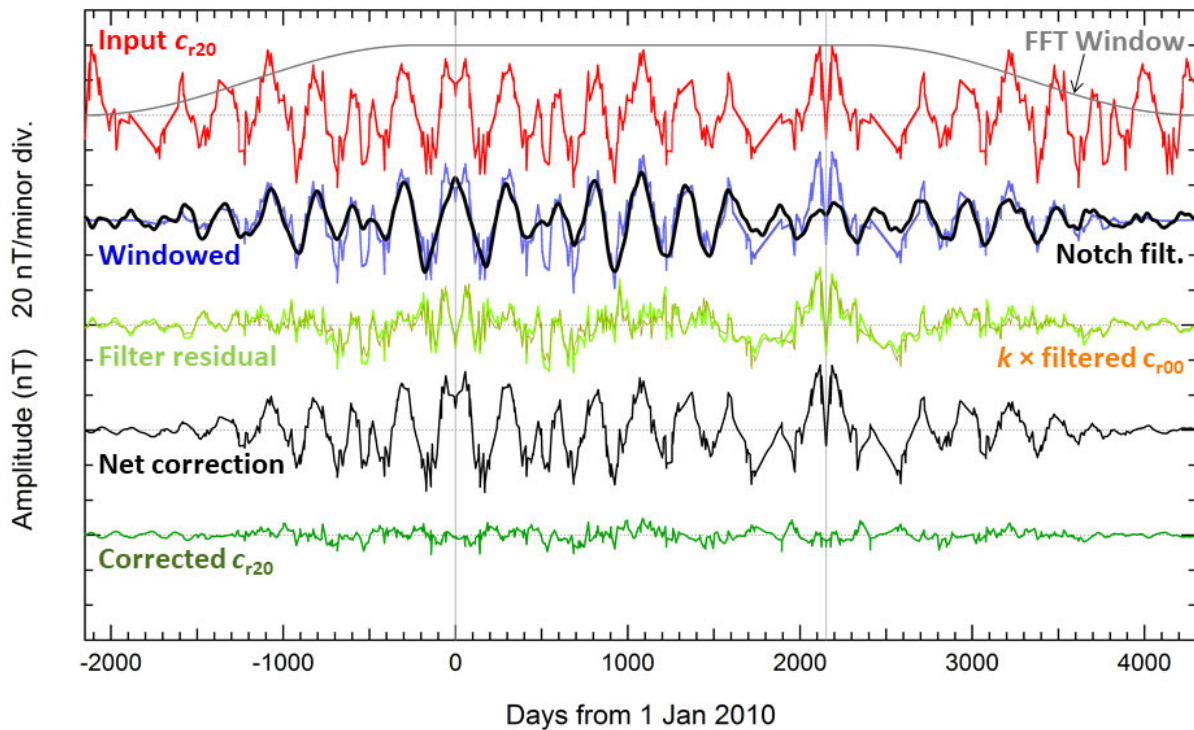


**Figure 15.** Correction analysis sequence for  $c_{r,20}$ . Vertical grey lines indicate the time span of the original input data (i.e., 0 to 2190 days from 1 January 2010). From top to bottom the traces show: detrended and mirrored time series (red, ‘Input  $c_{r,20}$ ’) together with the custom time window function (grey, ‘FFT Window’); windowed extended time series data (blue, ‘Windowed’) and notch filter signal (black, ‘Notch filt.’); time series with notch filtering applied, i.e., the residual between the blue and black traces (light green, ‘Filter residual’) and the linear correlation with the  $c_{r,00}$  time series where  $k$  is the slope fit coefficient (orange, ‘ $k \times$  filtered  $c_{r,00}$ ’); net correction for the input time series (thin black line, ‘Net correction’); and the net signal with identified artifacts removed (dark green, ‘Corrected  $c_{r,20}$ ’).

Filtered Harmonic Coefficients: L = 2

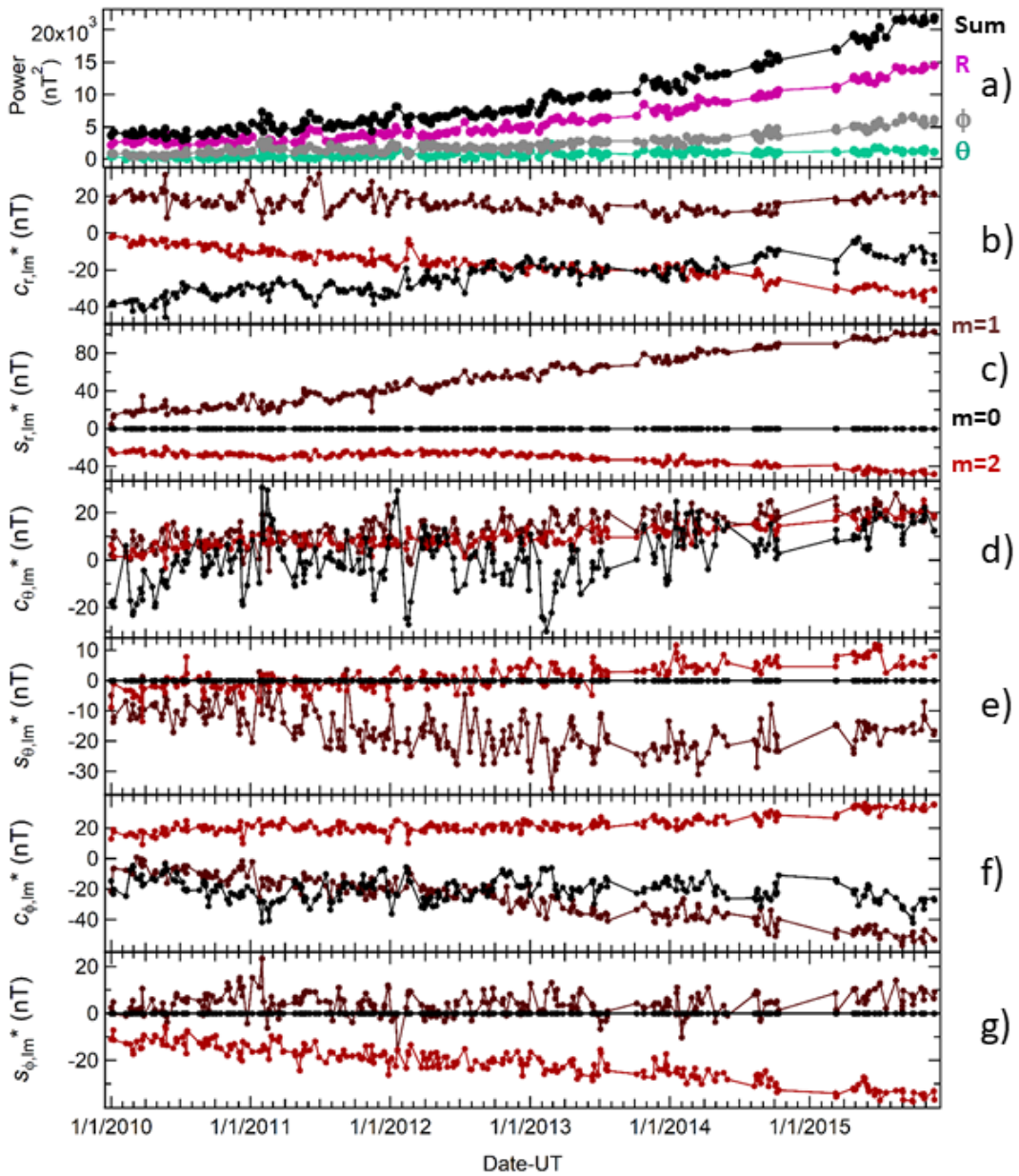


**Figure 16.** Time series of the filtered spherical harmonic coefficients  $c_{lm}'(t_i)$  and  $s_{lm}'(t_i)$  for  $l = 2$  after applying the notch and  $c_{r,00}'$  correlation corrections, in the same format as **Figure 14**.

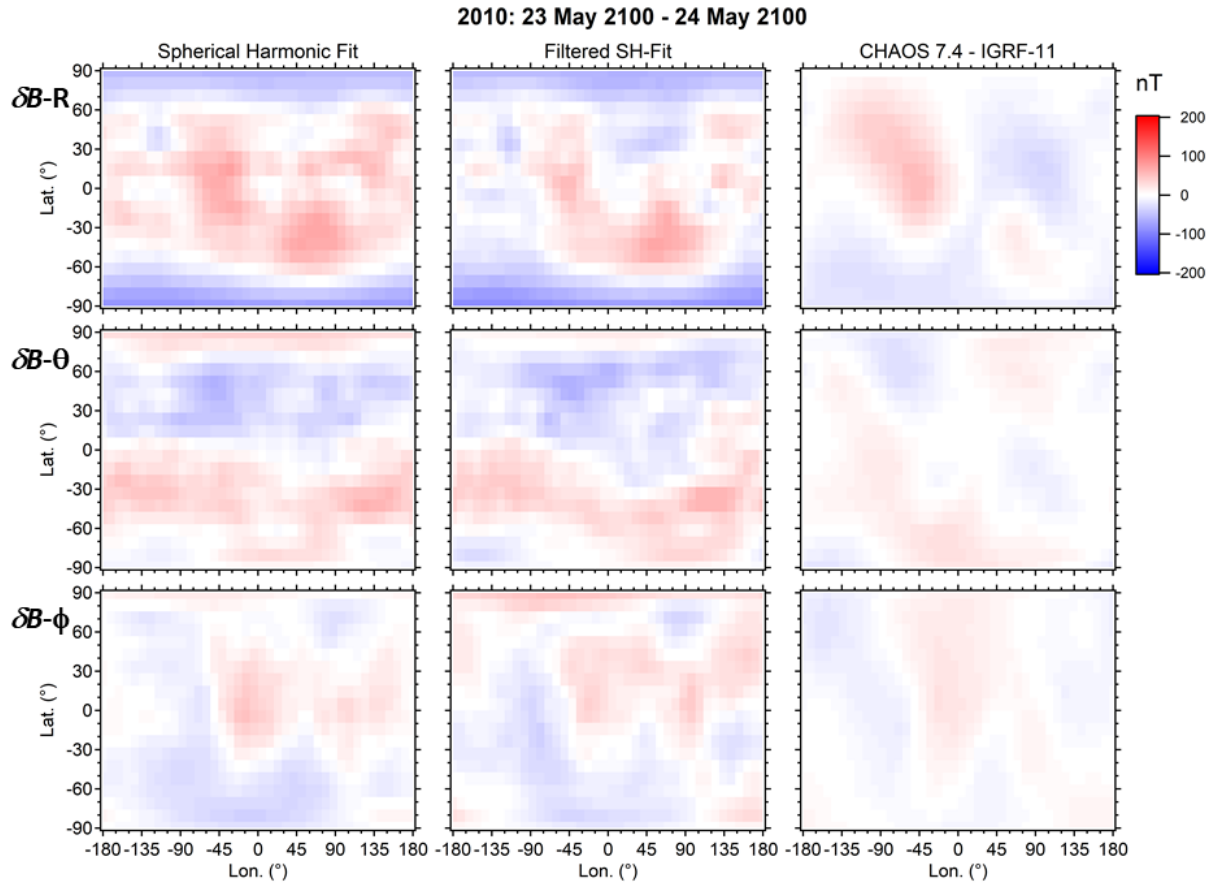


**Figure 17.** Magnetic field residuals relative to IGRF-11 reconstructed from the spherical harmonic coefficient time series and of the CHAOS 7.4 model relative to IGRF-11 versus geographic latitude and longitude for the quiet period of 2010-05-23/21:00 UT to 2010-05-24/21:00 UT. The columns show the original spherical harmonic fit on the left, the filtered spherical harmonic results in the center, and the residual of CHAOS 7.4 relative to IGRF-11 on the right. From top to bottom the rows show maps for the  $\delta B_r$ ,  $\delta B_\theta$ , and  $\delta B_\phi$  magnetic field components.

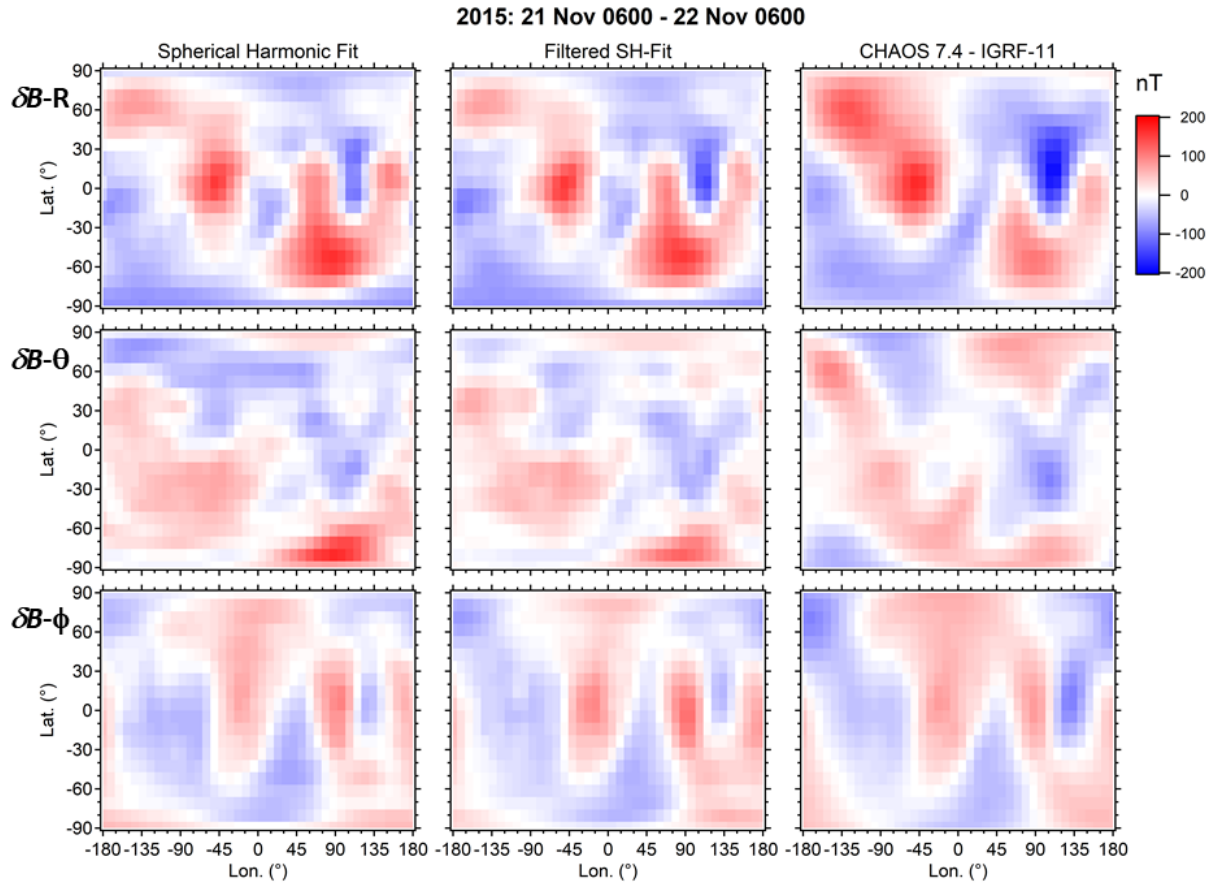


**Figure 18.** Magnetic field residuals relative to IGRF-11 reconstructed from the spherical harmonic coefficient time series and of CHAOS 7.4 for 2015-11-21/06:00 UT to 2015-11-22/06:00 UT in the same format as **Figure 17**.

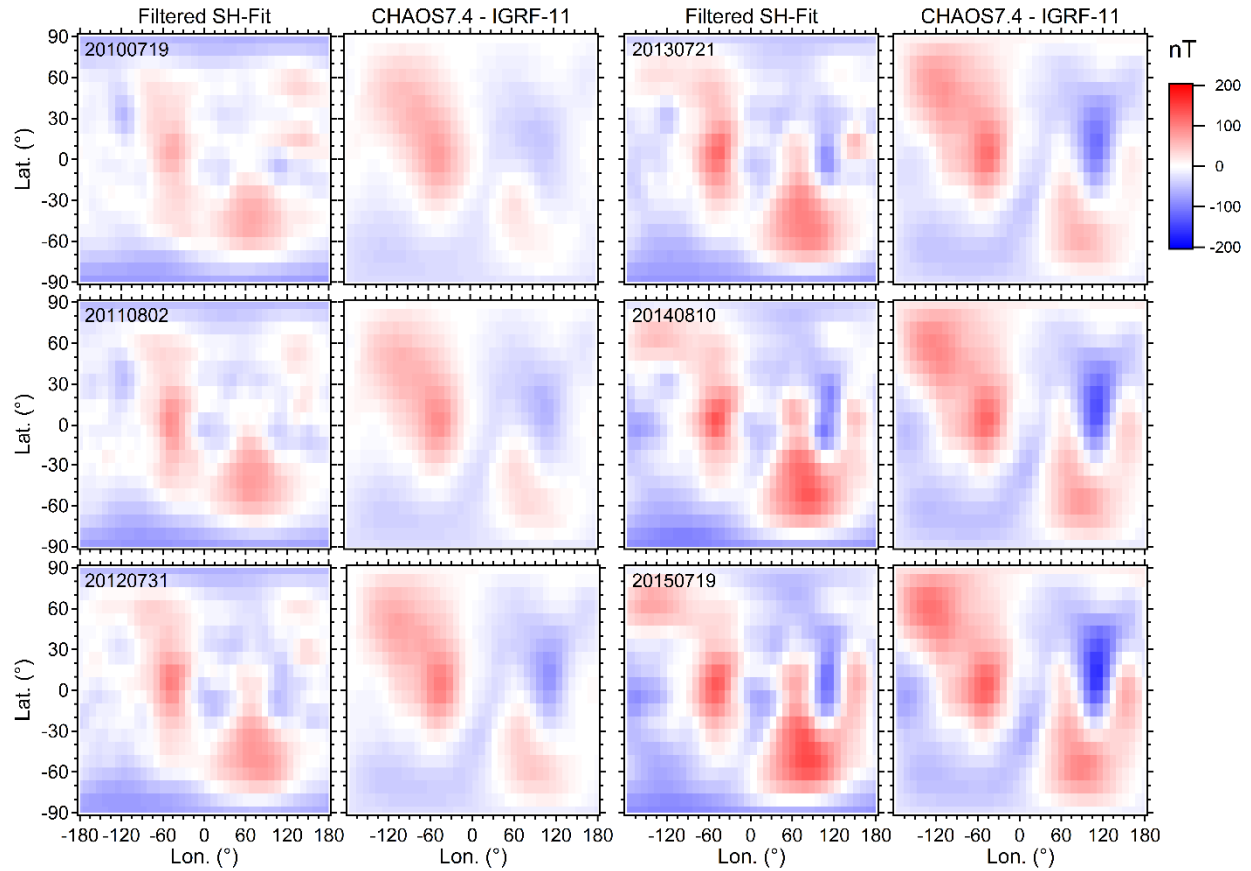


**Figure 19.** Maps of the radial component magnetic residuals,  $\delta B_r$ , relative to IGRF-11 from the filtered spherical harmonic coefficient time series and of CHAOS 7.4 minus IGRF-11 for six different quiet days, one for each year from 2010 through 2015. Dates were chosen to be close to 1 August of each year so the interval between successive maps is approximately one year. The Iridium results are shown in the first and third columns ('Filtered SH-Fit') and the CHAOS 7.4 results in the second and fourth columns ('CHAOS 7.4 - IGRF 11'). The Iridium and CHAOS 7.4 results are shown side-by-side for each date in columns one and two for 19 July 2010, 2 August 2011, and 31 July 2012, and in columns three and four for 21 July 2013, 10 August 2014, and 19 July 2015. Corresponding figures for the polar and azimuthal components,  $\delta B_\theta$  and  $\delta B_\phi$ , are provided in the supplementary material.

**Iridium Communications Satellite Constellation Data for Study of Earth's Magnetic Field**

Brian J. Anderson<sup>1</sup>, Regupathi Angappan<sup>2</sup>, Ankit Barik<sup>2</sup>, Sarah K. Vines<sup>1</sup>, Sabine Stanley<sup>2</sup>, Pietro N. Bernasconi<sup>1</sup>, Haje Korth<sup>1</sup>, and Robin J. Barnes<sup>1</sup>

1. The Johns Hopkins University Applied Physics Laboratory, Laurel, MD.

2. Department of Earth and Planetary Sciences, The Johns Hopkins University, Baltimore, MD.

**Contents of this file**

Figures S1 and S2

**Additional Supporting Information (Files uploaded separately)**

Caption for Table S1

**Introduction**

The two Supporting Information figures are in the same format as Figure 19 and compare differences between the IGRF-11 magnetic field model to the Iridium data and CHAOS 7.4 model for the polar angle,  $\delta B_{\theta}$ , and azimuthal,  $\delta B_{\phi}$ , components. The Supporting Information Table S1 is the list of the 262 24-hour quiet intervals used for the analysis. The table includes the date and time range of each interval together with the geomagnetic activity measures and the derived activity indices (z-scores) used to rank and select the quietest intervals.

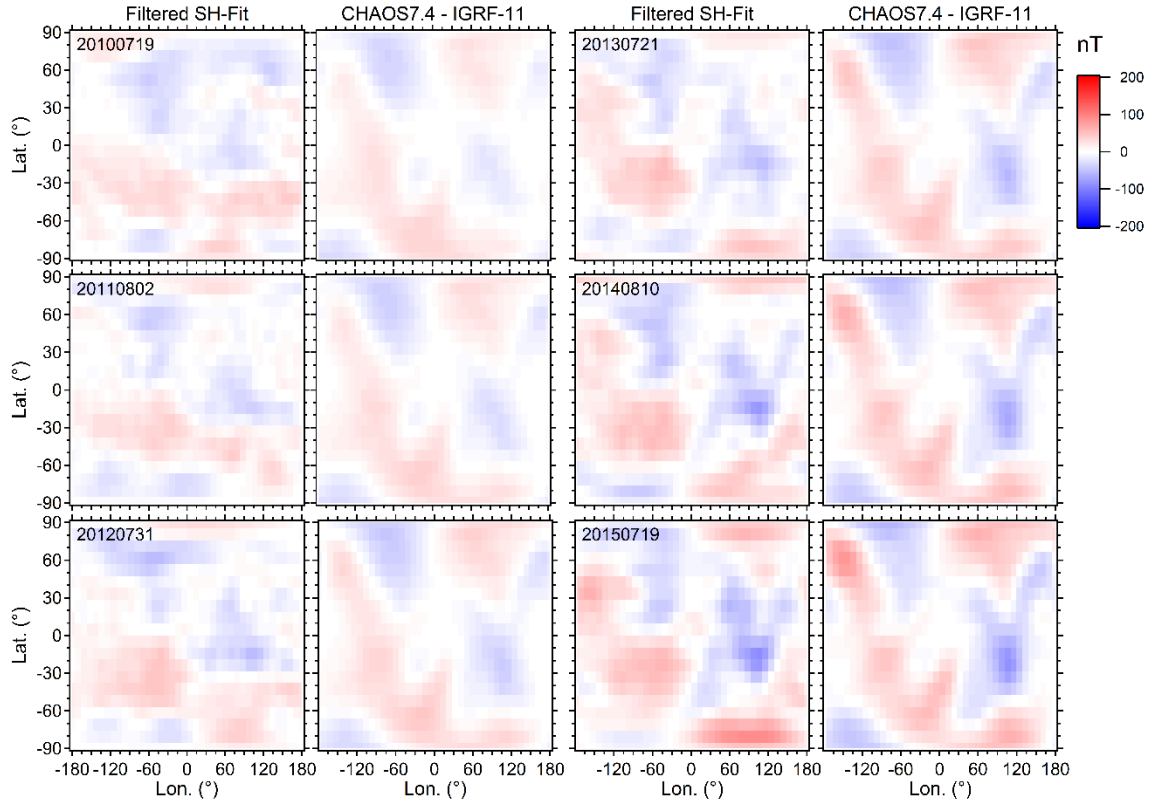


**Figure S1.** Maps of the polar angle component magnetic residuals,  $\delta B_{\theta}$ , relative to IGRF-11 from the filtered spherical harmonic coefficient time series and of CHAOS 7.4 minus IGRF-11 for six different quiet days, one for each year from 2010 through 2015. The Iridium results are shown in the first and third columns ('Filtered SH-Fit') and the CHAOS 7.4 results in the second and fourth columns ('CHAOS 7.4 - IGRF 11'). The Iridium and CHAOS 7.4 results are shown side-by-side for each date in columns one and two for 19 July 2010, 2 August 2011, and 31 July 2012, and in columns three and four for 21 July 2013, 10 August 2014, and 19 July 2015.

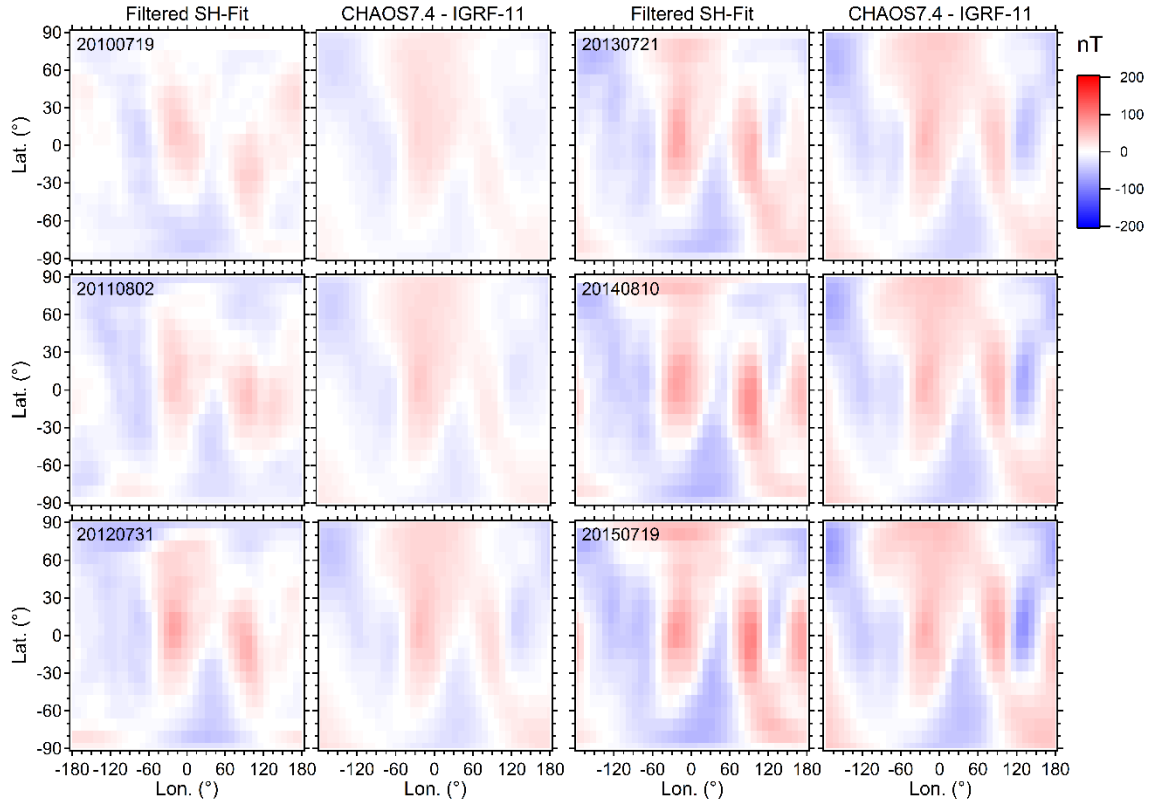


**Figure S2.** Maps of the azimuthal component magnetic residuals,  $\delta B_\phi$ , relative to IGRF-11 from the filtered spherical harmonic coefficient time series and of CHAOS 7.4 minus IGRF-11 for six different quiet days, in the same format as Figure S1.

**Table S1.** Table lists all 262 24-hour quiet intervals selected for the main field analysis. Table columns are as follows: start date and time of interval, 'Quiet 24-hr begin'; end date and time of interval, 'Quiet 24-hr end'; average AE index, 'avg\_AE'; average northern hemisphere Birkeland current from AMPERE, 'avg\_iN'; average southern hemisphere Birkeland current from AMPERE, 'avg\_iS'; average symH index, avg\_sH; average asyH index, avg\_aH; average over the month for the interval of the sum of northern and southern hemisphere total Birkeland currents from AMPERE, mon\_i; standard deviation of sum of northern plus southern hemisphere total Birkeland current for the month of the interval, sd\_i; monthly average of the sum of the absolute values of symH and asyH, monH; standard deviation of the sum of the absolute values of symH and asyH for the month, sd\_H; monthly averaged AE index, monAE; standard deviation of AE index for the month of the interval, sd\_AE; z-score of the interval averaged AE for the month, V\_AE; z-score of the interval averaged total Birkeland current, V\_i; z-score of the interval averaged sum of the absolute values of symH and asyH, V\_H; the net activity index computed as the average of the AE, Birkeland current, and sym/asyH z-scores, Q\_indx. All values for the AE, symH, and asyH indices are in nT. All values for total Birkeland currents are in mega-Amperes (MA).

Quiet 24-hr begin	Quiet 24-hr end	avg_AE	avg_iN	avg_iS	avg_sH	avg_aH	mon_i	sd_i	monH	sd_H	monAE	sd_AE	V_AE	V_i	V_H	Q_indx
01/01/2010 00:00	01/02/2010 00:00	9.2	0.459	0.352	1.4	10.9	1.109	0.843	14.1	9.2	21.7	38.7	-0.323	-0.353	-0.198	-0.292
01/06/2010 18:00	01/07/2010 18:00	12.2	0.374	0.446	-0.5	8.1	1.109	0.843	14.1	9.2	21.7	38.7	-0.245	-0.343	-0.611	-0.400
01/08/2010 09:00	01/09/2010 09:00	13.3	0.513	0.334	-3.3	8.7	1.109	0.843	14.1	9.2	21.7	38.7	-0.217	-0.311	-0.233	-0.253
02/08/2010 15:00	02/09/2010 15:00	26.0	0.335	0.798	-0.4	16.0	1.208	1.162	17.9	10.9	41.1	63.4	-0.239	-0.065	-0.140	-0.148
02/20/2010 06:00	02/21/2010 06:00	17.8	0.163	0.452	-3.2	9.4	1.208	1.162	17.9	10.9	41.1	63.4	-0.368	-0.510	-0.491	-0.457
02/26/2010 15:00	02/27/2010 15:00	28.1	0.138	0.301	-4.3	12.5	1.208	1.162	17.9	10.9	41.1	63.4	-0.206	-0.662	-0.107	-0.325
02/27/2010 21:00	02/28/2010 21:00	36.4	0.316	0.433	4.2	10.3	1.208	1.162	17.9	10.9	41.1	63.4	-0.075	-0.395	-0.308	-0.259
03/08/2010 21:00	03/09/2010 21:00	34.4	0.484	0.530	0.7	8.9	1.335	0.761	13.9	5.7	56.3	45.6	-0.481	-0.422	-0.747	-0.550
03/18/2010 06:00	03/19/2010 06:00	37.6	0.536	0.573	-0.7	14.0	1.335	0.761	13.9	5.7	56.3	45.6	-0.411	-0.297	0.142	-0.189
03/21/2010 15:00	03/22/2010 15:00	30.2	0.259	0.332	-1.2	5.5	1.335	0.761	13.9	5.7	56.3	45.6	-0.573	-0.978	-1.263	-0.938
03/23/2010 12:00	03/24/2010 12:00	35.7	0.326	0.340	2.5	8.5	1.335	0.761	13.9	5.7	56.3	45.6	-0.452	-0.879	-0.489	-0.607
03/27/2010 03:00	03/28/2010 03:00	43.8	0.558	0.482	4.2	10.3	1.335	0.761	13.9	5.7	56.3	45.6	-0.274	-0.388	0.110	-0.184
04/16/2010 18:00	04/17/2010 18:00	36.9	0.520	0.356	-6.7	10.8	1.237	2.124	16.9	24.1	57.6	172.4	-0.120	-0.170	0.026	-0.088
04/18/2010 06:00	04/19/2010 06:00	50.0	0.657	0.448	-2.0	12.0	1.237	2.124	16.9	24.1	57.6	172.4	-0.044	-0.062	-0.120	-0.076
04/25/2010 09:00	04/26/2010 09:00	38.3	0.479	0.295	-1.1	8.6	1.237	2.124	16.9	24.1	57.6	172.4	-0.112	-0.218	-0.302	-0.210
04/27/2010 06:00	04/28/2010 06:00	49.2	0.703	0.326	1.6	6.9	1.237	2.124	16.9	24.1	57.6	172.4	-0.049	-0.098	-0.350	-0.166
05/13/2010 15:00	05/14/2010 15:00	39.7	0.675	0.259	-1.6	10.5	1.208	2.231	14.3	21.9	60.5	151.2	-0.138	-0.123	-0.098	-0.120
05/15/2010 15:00	05/16/2010 15:00	44.3	0.617	0.355	-1.6	9.5	1.208	2.231	14.3	21.9	60.5	151.2	-0.108	-0.106	-0.144	-0.119
05/22/2010 12:00	05/23/2010 12:00	37.4	0.825	0.261	-0.2	7.4	1.208	2.231	14.3	21.9	60.5	151.2	-0.153	-0.055	-0.300	-0.169
05/23/2010 21:00	05/24/2010 21:00	39.3	0.625	0.190	1.4	10.3	1.208	2.231	14.3	21.9	60.5	151.2	-0.140	-0.176	-0.114	-0.143
05/27/2010 03:00	05/28/2010 03:00	59.4	0.744	0.276	-1.7	8.8	1.208	2.231	14.3	21.9	60.5	151.2	-0.007	-0.084	-0.169	-0.087
06/12/2010 06:00	06/13/2010 06:00	49.8	0.933	0.379	-1.1	10.2	1.673	1.345	16.1	14.4	75.3	102.2	-0.249	-0.268	-0.327	-0.281
06/19/2010 21:00	06/20/2010 21:00	45.2	0.974	0.303	-3.9	10.3	1.673	1.345	16.1	14.4	75.3	102.2	-0.295	-0.294	-0.129	-0.239
06/21/2010 09:00	06/22/2010 09:00	40.7	1.234	0.196	0.3	13.8	1.673	1.345	16.1	14.4	75.3	102.2	-0.338	-0.181	-0.136	-0.218
07/06/2010 12:00	07/07/2010 12:00	42.5	0.778	0.325	-3.6	10.2	1.360	1.045	16.1	7.1	59.4	73.7	-0.229	-0.246	-0.322	-0.266
07/10/2010 12:00	07/11/2010 12:00	42.3	0.879	0.364	0.5	11.4	1.360	1.045	16.1	7.1	59.4	73.7	-0.232	-0.112	-0.576	-0.307
07/16/2010 15:00	07/17/2010 15:00	43.1	0.647	0.243	-4.8	9.3	1.360	1.045	16.1	7.1	59.4	73.7	-0.222	-0.450	-0.283	-0.318
07/17/2010 15:00	07/18/2010 15:00	42.5	0.818	0.302	-2.4	8.3	1.360	1.045	16.1	7.1	59.4	73.7	-0.229	-0.230	-0.757	-0.405
07/18/2010 15:00	07/19/2010 15:00	40.0	0.671	0.301	-0.7	12.0	1.360	1.045	16.1	7.1	59.4	73.7	-0.264	-0.371	-0.480	-0.372
08/19/2010 12:00	08/20/2010 12:00	34.9	0.886	0.405	-4.7	11.6	1.732	1.826	17.7	17.9	67.7	107.3	-0.307	-0.242	-0.075	-0.208
08/29/2010 15:00	08/30/2010 15:00	33.2	0.488	0.293	-5.0	8.8	1.732	1.826	17.7	17.9	67.7	107.3	-0.322	-0.521	-0.218	-0.354
08/30/2010 18:00	08/31/2010 18:00	34.8	0.487	0.344	-1.3	10.0	1.732	1.826	17.7	17.9	67.7	107.3	-0.307	-0.493	-0.355	-0.385
08/31/2010 12:00	09/01/2010 12:00	35.3	0.760	0.414	-0.6	10.3	0.937	1.089	13.6	8.5	41.4	65.8	-0.093	0.218	-0.312	-0.062
09/03/2010 21:00	09/04/2010 21:00	36.9	0.466	0.228	-3.8	11.0	0.937	1.089	13.6	8.5	41.4	65.8	-0.067	-0.223	0.144	-0.049

09/04/2010 21:00	09/05/2010 21:00	43.5	0.635	0.332	-0.6	9.5	0.937	1.089	13.6	8.5	41.4	65.8	0.032	0.028	-0.413	-0.118
09/11/2010 06:00	09/12/2010 06:00	31.8	0.326	0.208	-3.5	7.4	0.937	1.089	13.6	8.5	41.4	65.8	-0.146	-0.370	-0.322	-0.279
09/12/2010 09:00	09/13/2010 09:00	34.0	0.497	0.290	0.1	11.1	0.937	1.089	13.6	8.5	41.4	65.8	-0.112	-0.138	-0.283	-0.178
09/22/2010 06:00	09/23/2010 06:00	34.5	0.455	0.414	-1.2	6.9	0.937	1.089	13.6	8.5	41.4	65.8	-0.105	-0.062	-0.645	-0.271
10/01/2010 18:00	10/02/2010 18:00	20.8	0.250	0.271	-5.0	7.2	1.142	1.525	15.7	16.4	33.3	94.4	-0.133	-0.407	-0.214	-0.251
10/03/2010 12:00	10/04/2010 12:00	25.4	0.359	0.323	-0.9	3.9	1.142	1.525	15.7	16.4	33.3	94.4	-0.084	-0.302	-0.665	-0.350
10/14/2010 09:00	10/15/2010 09:00	23.7	0.283	0.354	0.6	7.0	1.142	1.525	15.7	16.4	33.3	94.4	-0.102	-0.331	-0.494	-0.309
10/31/2010 12:00	11/01/2010 12:00	24.3	0.348	0.687	1.8	12.0	1.380	1.000	14.5	11.2	44.4	63.7	-0.315	-0.345	-0.063	-0.241
11/01/2010 06:00	11/02/2010 06:00	26.4	0.336	0.643	1.6	9.2	1.380	1.000	14.5	11.2	44.4	63.7	-0.283	-0.401	-0.335	-0.340
11/06/2010 15:00	11/07/2010 15:00	28.1	0.296	0.548	-0.4	10.1	1.380	1.000	14.5	11.2	44.4	63.7	-0.257	-0.536	-0.362	-0.385
11/09/2010 15:00	11/10/2010 15:00	34.6	0.420	0.755	-4.7	7.6	1.380	1.000	14.5	11.2	44.4	63.7	-0.155	-0.205	-0.196	-0.185
11/19/2010 06:00	11/20/2010 06:00	25.8	0.329	0.848	-1.9	8.2	1.380	1.000	14.5	11.2	44.4	63.7	-0.292	-0.203	-0.404	-0.300
12/02/2010 06:00	12/03/2010 06:00	23.2	0.406	0.659	-2.6	10.9	1.162	1.038	12.8	10.1	34.5	61.3	-0.184	-0.093	0.067	-0.070
12/03/2010 06:00	12/04/2010 06:00	19.2	0.359	0.645	3.2	6.2	1.162	1.038	12.8	10.1	34.5	61.3	-0.249	-0.152	-0.331	-0.244
12/04/2010 21:00	12/05/2010 21:00	35.3	0.271	0.678	0.0	9.1	1.162	1.038	12.8	10.1	34.5	61.3	0.013	-0.205	-0.365	-0.186
12/09/2010 09:00	12/10/2010 09:00	28.3	0.307	0.607	-1.5	7.9	1.162	1.038	12.8	10.1	34.5	61.3	-0.102	-0.239	-0.337	-0.226
12/11/2010 00:00	12/12/2010 00:00	14.0	0.368	0.674	0.4	5.2	1.162	1.038	12.8	10.1	34.5	61.3	-0.334	-0.116	-0.721	-0.390
12/22/2010 09:00	12/23/2010 09:00	24.0	0.323	0.618	-4.7	8.9	1.162	1.038	12.8	10.1	34.5	61.3	-0.171	-0.213	0.078	-0.102
01/04/2011 21:00	01/05/2011 21:00	44.6	0.699	0.861	-0.5	8.3	1.689	0.845	13.5	7.9	59.8	41.9	-0.364	-0.153	-0.585	-0.367
01/23/2011 15:00	01/24/2011 15:00	37.4	0.444	0.743	4.9	11.1	1.689	0.845	13.5	7.9	59.8	41.9	-0.537	-0.594	0.321	-0.270
01/30/2011 03:00	01/31/2011 03:00	16.1	0.365	0.378	2.3	9.0	1.689	0.845	13.5	7.9	59.8	41.9	-1.045	-1.120	-0.279	-0.814
02/03/2011 03:00	02/04/2011 03:00	29.5	0.400	0.448	-4.8	12.5	1.321	1.436	15.5	11.9	41.4	77.5	-0.154	-0.329	0.150	-0.111
02/13/2011 09:00	02/14/2011 09:00	25.4	0.513	0.424	3.3	11.0	1.321	1.436	15.5	11.9	41.4	77.5	-0.207	-0.267	-0.099	-0.191
02/17/2011 03:00	02/18/2011 03:00	35.0	0.436	0.404	-1.0	12.1	1.321	1.436	15.5	11.9	41.4	77.5	-0.083	-0.335	-0.204	-0.207
02/24/2011 00:00	02/25/2011 00:00	33.8	0.511	0.408	0.2	12.7	1.321	1.436	15.5	11.9	41.4	77.5	-0.099	-0.280	-0.217	-0.199
02/27/2011 03:00	02/28/2011 03:00	41.3	0.662	0.419	-0.3	7.1	1.321	1.436	15.5	11.9	41.4	77.5	-0.002	-0.167	-0.682	-0.283
03/14/2011 18:00	03/15/2011 18:00	25.5	0.587	0.294	-7.6	8.7	1.286	2.250	13.8	23.6	40.2	147.0	-0.100	-0.180	0.108	-0.057
03/15/2011 18:00	03/16/2011 18:00	24.9	0.503	0.227	0.4	7.6	1.286	2.250	13.8	23.6	40.2	147.0	-0.104	-0.247	-0.246	-0.199
03/16/2011 18:00	03/17/2011 18:00	29.0	0.767	0.394	4.8	8.4	1.286	2.250	13.8	23.6	40.2	147.0	-0.076	-0.056	-0.023	-0.051
03/26/2011 06:00	03/27/2011 06:00	29.2	0.528	0.139	-0.2	9.3	1.286	2.250	13.8	23.6	40.2	147.0	-0.074	-0.275	-0.179	-0.176
03/27/2011 06:00	03/28/2011 06:00	36.2	0.829	0.310	0.7	10.3	1.286	2.250	13.8	23.6	40.2	147.0	-0.027	-0.065	-0.116	-0.069
04/25/2011 06:00	04/26/2011 06:00	48.9	1.014	0.251	-5.6	9.6	1.533	1.640	16.7	15.6	73.7	112.6	-0.220	-0.163	-0.102	-0.162
04/26/2011 15:00	04/27/2011 15:00	44.4	0.812	0.193	0.0	11.1	1.533	1.640	16.7	15.6	73.7	112.6	-0.260	-0.322	-0.359	-0.313
04/27/2011 18:00	04/28/2011 18:00	44.4	0.971	0.192	5.0	11.4	1.533	1.640	16.7	15.6	73.7	112.6	-0.261	-0.226	-0.024	-0.170
05/09/2011 03:00	05/10/2011 03:00	53.6	0.995	0.302	1.2	11.7	1.710	1.753	16.3	20.0	71.7	141.9	-0.128	-0.236	-0.170	-0.178

05/12/2011 12:00	05/13/2011 12:00	63.8	0.880	0.289	0.2	14.2	1.710	1.753	16.3	20.0	71.7	141.9	-0.056	-0.309	-0.095	-0.153
05/13/2011 21:00	05/14/2011 21:00	57.6	1.177	0.408	6.2	9.7	1.710	1.753	16.3	20.0	71.7	141.9	-0.100	-0.071	-0.023	-0.065
05/19/2011 12:00	05/20/2011 12:00	52.4	1.009	0.271	-0.7	11.2	1.710	1.753	16.3	20.0	71.7	141.9	-0.136	-0.245	-0.222	-0.201
05/20/2011 12:00	05/21/2011 12:00	57.7	1.012	0.377	5.4	13.2	1.710	1.753	16.3	20.0	71.7	141.9	-0.098	-0.183	0.113	-0.056
05/22/2011 09:00	05/23/2011 09:00	52.8	1.061	0.240	2.2	10.6	1.710	1.753	16.3	20.0	71.7	141.9	-0.133	-0.233	-0.177	-0.181
05/25/2011 03:00	05/26/2011 03:00	72.1	1.396	0.384	0.6	11.0	1.710	1.753	16.3	20.0	71.7	141.9	0.003	0.040	-0.238	-0.065
06/03/2011 21:00	06/04/2011 21:00	81.4	1.082	0.458	-2.7	11.9	2.102	1.344	18.4	10.5	106.5	100.1	-0.251	-0.418	-0.364	-0.344
06/18/2011 06:00	06/19/2011 06:00	68.0	1.074	0.486	-2.0	11.0	2.102	1.344	18.4	10.5	106.5	100.1	-0.384	-0.403	-0.512	-0.433
06/28/2011 06:00	06/29/2011 06:00	42.1	0.807	0.335	-0.3	9.3	2.102	1.344	18.4	10.5	106.5	100.1	-0.643	-0.714	-0.838	-0.732
07/16/2011 09:00	07/17/2011 09:00	72.2	0.934	0.620	3.0	11.2	2.211	1.266	18.9	10.8	102.9	93.4	-0.328	-0.519	-0.436	-0.428
07/27/2011 06:00	07/28/2011 06:00	58.0	0.768	0.500	-6.5	8.6	2.211	1.266	18.9	10.8	102.9	93.4	-0.481	-0.745	-0.353	-0.526
07/28/2011 06:00	07/29/2011 06:00	47.9	0.765	0.378	0.6	9.0	2.211	1.266	18.9	10.8	102.9	93.4	-0.588	-0.844	-0.861	-0.764
08/02/2011 18:00	08/03/2011 18:00	50.7	0.601	0.376	-3.2	9.5	1.453	1.448	17.4	19.6	68.9	82.8	-0.220	-0.329	-0.243	-0.264
08/18/2011 21:00	08/19/2011 21:00	37.9	0.516	0.387	-2.1	13.0	1.453	1.448	17.4	19.6	68.9	82.8	-0.375	-0.380	-0.119	-0.291
08/19/2011 21:00	08/20/2011 21:00	60.4	0.777	0.583	-0.5	10.9	1.453	1.448	17.4	19.6	68.9	82.8	-0.103	-0.064	-0.304	-0.157
08/21/2011 00:00	08/22/2011 00:00	43.4	0.675	0.473	-0.1	7.4	1.453	1.448	17.4	19.6	68.9	82.8	-0.308	-0.211	-0.505	-0.341
08/31/2011 03:00	09/01/2011 03:00	51.6	0.485	0.503	-0.9	10.4	1.453	1.448	17.4	19.6	68.9	82.8	-0.208	-0.321	-0.313	-0.281
08/31/2011 12:00	09/01/2011 12:00	49.5	0.522	0.519	0.5	11.6	1.453	1.448	17.4	19.6	68.9	82.8	-0.235	-0.285	-0.270	-0.263
09/08/2011 12:00	09/09/2011 12:00	39.4	0.528	0.531	5.1	12.6	1.644	2.313	20.5	22.8	64.2	144.0	-0.172	-0.253	-0.124	-0.183
09/23/2011 06:00	09/24/2011 06:00	30.9	0.505	0.500	0.0	13.5	1.644	2.313	20.5	22.8	64.2	144.0	-0.231	-0.276	-0.309	-0.272
10/10/2011 12:00	10/11/2011 12:00	34.9	0.472	0.561	-0.2	12.9	1.605	1.793	14.6	20.1	47.0	83.6	-0.145	-0.319	-0.075	-0.180
10/13/2011 21:00	10/14/2011 21:00	33.6	0.524	0.692	2.7	8.8	1.605	1.793	14.6	20.1	47.0	83.6	-0.160	-0.217	-0.159	-0.179
10/18/2011 00:00	10/19/2011 00:00	56.6	0.650	0.782	-0.3	8.3	1.605	1.793	14.6	20.1	47.0	83.6	0.115	-0.096	-0.301	-0.094
10/22/2011 03:00	10/23/2011 03:00	29.1	0.434	0.773	0.4	9.6	1.605	1.793	14.6	20.1	47.0	83.6	-0.214	-0.222	-0.230	-0.222
10/28/2011 12:00	10/29/2011 12:00	25.5	0.354	0.364	-13.4	11.2	1.605	1.793	14.6	20.1	47.0	83.6	-0.257	-0.495	0.496	-0.085
11/06/2011 03:00	11/07/2011 03:00	28.6	0.540	0.684	0.9	10.9	1.651	1.532	13.4	16.7	30.5	90.5	-0.021	-0.279	-0.094	-0.131
11/09/2011 15:00	11/10/2011 15:00	27.9	0.440	0.481	-5.0	10.3	1.651	1.532	13.4	16.7	30.5	90.5	-0.029	-0.477	0.115	-0.130
11/12/2011 18:00	11/13/2011 18:00	28.9	0.482	0.552	-4.5	9.4	1.651	1.532	13.4	16.7	30.5	90.5	-0.017	-0.403	0.034	-0.129
11/18/2011 09:00	11/19/2011 09:00	24.4	0.515	0.761	0.1	10.4	1.651	1.532	13.4	16.7	30.5	90.5	-0.068	-0.245	-0.172	-0.161
11/19/2011 09:00	11/20/2011 09:00	19.0	0.325	0.482	2.2	7.3	1.651	1.532	13.4	16.7	30.5	90.5	-0.128	-0.551	-0.233	-0.304
12/06/2011 00:00	12/07/2011 00:00	18.7	0.453	0.448	-4.0	8.7	1.253	0.994	15.1	8.5	24.7	43.7	-0.137	-0.354	-0.295	-0.262
12/15/2011 12:00	12/16/2011 12:00	19.9	0.504	0.724	-4.5	11.3	1.253	0.994	15.1	8.5	24.7	43.7	-0.108	-0.025	0.080	-0.018
12/16/2011 12:00	12/17/2011 12:00	14.6	0.373	0.339	0.2	9.5	1.253	0.994	15.1	8.5	24.7	43.7	-0.231	-0.544	-0.642	-0.472
12/25/2011 12:00	12/26/2011 12:00	17.2	0.561	0.499	-4.6	8.5	1.253	0.994	15.1	8.5	24.7	43.7	-0.171	-0.194	-0.250	-0.205
12/26/2011 21:00	12/27/2011 21:00	17.0	0.512	0.326	0.9	13.1	1.253	0.994	15.1	8.5	24.7	43.7	-0.175	-0.418	-0.140	-0.244

01/04/2012 06:00	01/05/2012 06:00	24.7	0.532	0.541	-7.6	13.5	1.971	1.645	17.7	17.9	59.5	91.4	-0.381	-0.546	0.191	-0.245
01/14/2012 15:00	01/15/2012 15:00	22.4	0.699	0.599	0.6	13.5	1.971	1.645	17.7	17.9	59.5	91.4	-0.407	-0.409	-0.199	-0.338
01/19/2012 00:00	01/20/2012 00:00	45.6	0.851	0.956	-0.6	12.4	1.971	1.645	17.7	17.9	59.5	91.4	-0.152	-0.100	-0.258	-0.170
02/11/2012 03:00	02/12/2012 03:00	59.2	0.929	0.839	4.4	11.6	2.075	1.730	17.0	15.6	77.2	105.4	-0.171	-0.177	-0.066	-0.138
02/16/2012 09:00	02/17/2012 09:00	45.6	0.626	0.642	-8.4	11.3	2.075	1.730	17.0	15.6	77.2	105.4	-0.300	-0.466	0.173	-0.198
02/17/2012 09:00	02/18/2012 09:00	21.1	0.341	0.347	3.3	8.0	2.075	1.730	17.0	15.6	77.2	105.4	-0.532	-0.802	-0.371	-0.568
02/22/2012 21:00	02/23/2012 21:00	35.9	0.494	0.516	-3.6	13.5	2.075	1.730	17.0	15.6	77.2	105.4	-0.392	-0.616	-0.003	-0.337
03/21/2012 21:00	03/22/2012 21:00	57.4	0.725	0.716	-2.9	13.1	2.343	2.830	21.1	30.3	108.7	167.8	-0.306	-0.319	-0.167	-0.264
03/25/2012 12:00	03/26/2012 12:00	54.4	0.705	0.584	0.2	9.2	2.343	2.830	21.1	30.3	108.7	167.8	-0.324	-0.372	-0.386	-0.361
03/28/2012 21:00	03/29/2012 21:00	45.6	0.673	0.538	-5.5	11.7	2.343	2.830	21.1	30.3	108.7	167.8	-0.376	-0.400	-0.127	-0.301
03/30/2012 12:00	03/31/2012 12:00	40.5	0.566	0.549	3.3	14.6	2.343	2.830	21.1	30.3	108.7	167.8	-0.406	-0.434	-0.108	-0.316
04/05/2012 21:00	04/06/2012 21:00	37.4	0.758	0.479	-4.8	10.4	1.820	2.103	17.6	21.4	92.3	131.7	-0.418	-0.277	-0.115	-0.270
04/08/2012 18:00	04/09/2012 18:00	45.7	0.495	0.394	-0.3	14.6	1.820	2.103	17.6	21.4	92.3	131.7	-0.354	-0.443	-0.127	-0.308
04/15/2012 21:00	04/16/2012 21:00	69.7	0.683	0.521	-0.8	11.4	1.820	2.103	17.6	21.4	92.3	131.7	-0.172	-0.293	-0.251	-0.239
04/20/2012 15:00	04/21/2012 15:00	58.2	1.005	0.645	-0.1	12.7	1.820	2.103	17.6	21.4	92.3	131.7	-0.260	-0.081	-0.224	-0.188
04/29/2012 21:00	04/30/2012 21:00	62.5	0.960	0.570	-3.4	13.2	1.820	2.103	17.6	21.4	92.3	131.7	-0.227	-0.138	-0.045	-0.137
05/04/2012 03:00	05/05/2012 03:00	39.0	0.803	0.318	-8.9	9.3	1.728	1.733	18.8	14.1	75.4	116.6	-0.312	-0.350	-0.042	-0.235
05/05/2012 03:00	05/06/2012 03:00	62.9	1.057	0.520	-4.8	10.0	1.728	1.733	18.8	14.1	75.4	116.6	-0.108	-0.087	-0.280	-0.158
05/06/2012 21:00	05/07/2012 21:00	45.9	0.758	0.316	2.4	14.0	1.728	1.733	18.8	14.1	75.4	116.6	-0.254	-0.377	-0.174	-0.268
05/21/2012 03:00	05/22/2012 03:00	69.4	0.871	0.491	-3.0	9.8	1.728	1.733	18.8	14.1	75.4	116.6	-0.052	-0.211	-0.421	-0.228
05/27/2012 06:00	05/28/2012 06:00	61.5	0.684	0.347	-7.0	11.8	1.728	1.733	18.8	14.1	75.4	116.6	-0.120	-0.402	0.002	-0.173
05/28/2012 18:00	05/29/2012 18:00	76.3	1.296	0.589	-0.3	11.6	1.728	1.733	18.8	14.1	75.4	116.6	0.008	0.091	-0.490	-0.131
06/13/2012 09:00	06/14/2012 09:00	77.2	1.308	0.452	0.3	16.3	1.754	2.456	20.6	16.7	81.0	160.2	-0.024	0.002	-0.239	-0.087
06/14/2012 12:00	06/15/2012 12:00	61.0	1.117	0.357	6.5	12.3	1.754	2.456	20.6	16.7	81.0	160.2	-0.125	-0.114	-0.109	-0.116
06/21/2012 06:00	06/22/2012 06:00	56.9	1.092	0.471	-1.0	12.1	1.754	2.456	20.6	16.7	81.0	160.2	-0.150	-0.078	-0.447	-0.225
06/22/2012 15:00	06/23/2012 15:00	69.2	1.060	0.438	0.8	14.0	1.754	2.456	20.6	16.7	81.0	160.2	-0.073	-0.104	-0.348	-0.175
07/13/2012 09:00	07/14/2012 09:00	79.0	1.058	0.496	-0.5	14.6	2.264	3.377	21.7	29.9	109.4	217.3	-0.140	-0.210	-0.220	-0.190
07/26/2012 12:00	07/27/2012 12:00	38.3	0.892	0.266	5.6	11.2	2.264	3.377	21.7	29.9	109.4	217.3	-0.327	-0.328	-0.163	-0.273
07/31/2012 03:00	08/01/2012 03:00	84.3	1.215	0.433	-9.3	11.8	2.264	3.377	21.7	29.9	109.4	217.3	-0.116	-0.182	-0.021	-0.106
08/10/2012 09:00	08/11/2012 09:00	44.6	1.035	0.282	-1.0	13.0	1.835	1.169	21.0	8.6	86.9	81.0	-0.522	-0.443	-0.816	-0.594
08/29/2012 18:00	08/30/2012 18:00	43.9	0.742	0.379	-4.8	15.8	1.835	1.169	21.0	8.6	86.9	81.0	-0.530	-0.611	-0.053	-0.398
08/30/2012 21:00	08/31/2012 21:00	42.1	0.593	0.271	-1.2	9.8	1.835	1.169	21.0	8.6	86.9	81.0	-0.553	-0.831	-1.166	-0.850
09/10/2012 15:00	09/11/2012 15:00	37.2	0.742	0.229	-5.1	14.9	1.355	2.608	16.5	24.4	47.0	159.6	-0.062	-0.147	0.146	-0.021
09/13/2012 21:00	09/14/2012 21:00	43.6	0.986	0.517	1.8	14.6	1.355	2.608	16.5	24.4	47.0	159.6	-0.022	0.057	-0.002	0.011
09/23/2012 03:00	09/24/2012 03:00	29.9	0.484	0.274	-3.4	8.8	1.355	2.608	16.5	24.4	47.0	159.6	-0.107	-0.229	-0.173	-0.170

09/24/2012 06:00	09/25/2012 06:00	35.2	0.827	0.443	0.1	12.6	1.355	2.608	16.5	24.4	47.0	159.6	-0.074	-0.033	-0.151	-0.086
09/25/2012 06:00	09/26/2012 06:00	38.9	0.749	0.408	0.2	11.2	1.355	2.608	16.5	24.4	47.0	159.6	-0.051	-0.076	-0.208	-0.111
09/28/2012 00:00	09/29/2012 00:00	38.7	0.499	0.328	-0.1	13.3	1.355	2.608	16.5	24.4	47.0	159.6	-0.052	-0.202	-0.126	-0.127
10/19/2012 18:00	10/20/2012 18:00	36.1	0.378	0.356	-4.9	10.4	1.410	2.661	16.9	31.9	52.2	147.9	-0.109	-0.254	-0.049	-0.137
10/20/2012 18:00	10/21/2012 18:00	36.8	0.682	0.669	-3.9	10.9	1.410	2.661	16.9	31.9	52.2	147.9	-0.104	-0.022	-0.067	-0.064
10/22/2012 03:00	10/23/2012 03:00	33.4	0.529	0.559	3.0	7.2	1.410	2.661	16.9	31.9	52.2	147.9	-0.127	-0.121	-0.211	-0.153
10/30/2012 06:00	10/31/2012 06:00	34.9	0.631	0.523	4.1	8.9	1.410	2.661	16.9	31.9	52.2	147.9	-0.117	-0.096	-0.122	-0.112
11/08/2012 03:00	11/09/2012 03:00	31.9	0.480	0.532	-0.1	9.6	1.400	2.336	15.7	22.0	39.7	120.9	-0.064	-0.166	-0.272	-0.168
11/09/2012 09:00	11/10/2012 09:00	25.3	0.373	0.307	3.7	13.6	1.400	2.336	15.7	22.0	39.7	120.9	-0.119	-0.308	0.069	-0.119
11/27/2012 21:00	11/28/2012 21:00	30.3	0.491	0.843	-0.4	8.1	1.400	2.336	15.7	22.0	39.7	120.9	-0.078	-0.028	-0.332	-0.146
12/06/2012 06:00	12/07/2012 06:00	16.6	0.270	0.594	-4.5	11.3	1.135	1.019	15.2	6.4	23.7	54.2	-0.131	-0.266	0.074	-0.108
12/07/2012 06:00	12/08/2012 06:00	18.3	0.234	0.580	0.7	12.2	1.135	1.019	15.2	6.4	23.7	54.2	-0.099	-0.315	-0.374	-0.263
12/10/2012 21:00	12/11/2012 21:00	24.2	0.339	0.778	0.2	13.2	1.135	1.019	15.2	6.4	23.7	54.2	0.009	-0.018	-0.290	-0.100
12/13/2012 18:00	12/14/2012 18:00	30.6	0.578	0.933	0.6	9.7	1.135	1.019	15.2	6.4	23.7	54.2	0.127	0.369	-0.780	-0.095
12/22/2012 12:00	12/23/2012 12:00	22.0	0.329	0.499	-3.4	12.7	1.135	1.019	15.2	6.4	23.7	54.2	-0.031	-0.301	0.129	-0.068
12/27/2012 12:00	12/28/2012 12:00	19.4	0.356	0.697	-0.4	12.9	1.135	1.019	15.2	6.4	23.7	54.2	-0.079	-0.080	-0.303	-0.154
01/01/2013 00:00	01/02/2013 00:00	15.7	0.435	0.527	-0.1	13.4	1.332	1.452	18.6	11.7	26.2	71.5	-0.147	-0.255	-0.432	-0.278
01/22/2013 18:00	01/23/2013 18:00	21.9	0.225	0.694	-3.4	12.5	1.332	1.452	18.6	11.7	26.2	71.5	-0.061	-0.284	-0.228	-0.191
01/30/2013 21:00	01/31/2013 21:00	19.8	0.293	0.603	-0.2	12.8	1.332	1.452	18.6	11.7	26.2	71.5	-0.090	-0.300	-0.478	-0.289
02/05/2013 18:00	02/06/2013 18:00	22.9	0.268	0.627	1.8	10.0	1.889	1.094	16.4	10.2	68.0	67.3	-0.669	-0.909	-0.445	-0.674
02/11/2013 06:00	02/12/2013 06:00	57.4	0.608	0.881	-1.7	9.9	1.889	1.094	16.4	10.2	68.0	67.3	-0.157	-0.366	-0.466	-0.330
02/24/2013 21:00	02/25/2013 21:00	35.0	0.529	0.689	1.7	16.1	1.889	1.094	16.4	10.2	68.0	67.3	-0.490	-0.613	0.140	-0.321
03/06/2013 06:00	03/07/2013 06:00	28.9	0.397	0.325	0.6	14.6	1.406	2.173	17.4	27.5	58.4	138.2	-0.213	-0.315	-0.084	-0.204
03/07/2013 18:00	03/08/2013 18:00	32.1	0.512	0.421	0.0	8.7	1.406	2.173	17.4	27.5	58.4	138.2	-0.190	-0.218	-0.318	-0.242
03/11/2013 09:00	03/12/2013 09:00	44.9	0.545	0.515	4.3	10.9	1.406	2.173	17.4	27.5	58.4	138.2	-0.098	-0.159	-0.082	-0.113
03/13/2013 09:00	03/14/2013 09:00	50.3	0.554	0.486	5.1	11.7	1.406	2.173	17.4	27.5	58.4	138.2	-0.059	-0.168	-0.023	-0.083
03/26/2013 03:00	03/27/2013 03:00	38.7	0.478	0.273	-2.2	13.1	1.406	2.173	17.4	27.5	58.4	138.2	-0.143	-0.301	-0.078	-0.174
04/15/2013 15:00	04/16/2013 15:00	37.9	0.733	0.238	-2.3	13.8	1.316	1.536	16.4	12.3	51.9	93.3	-0.150	-0.225	-0.031	-0.135
04/17/2013 15:00	04/18/2013 15:00	48.0	0.853	0.304	-3.5	9.5	1.316	1.536	16.4	12.3	51.9	93.3	-0.041	-0.104	-0.278	-0.141
04/18/2013 21:00	04/19/2013 21:00	31.7	0.749	0.184	-1.6	10.4	1.316	1.536	16.4	12.3	51.9	93.3	-0.216	-0.249	-0.356	-0.274
04/20/2013 18:00	04/21/2013 18:00	37.2	0.687	0.125	2.6	11.0	1.316	1.536	16.4	12.3	51.9	93.3	-0.158	-0.328	-0.224	-0.237
04/22/2013 06:00	04/23/2013 06:00	45.1	0.884	0.229	5.6	11.2	1.316	1.536	16.4	12.3	51.9	93.3	-0.072	-0.132	0.033	-0.057
05/03/2013 03:00	05/04/2013 03:00	89.8	1.193	0.381	-12.1	13.4	3.015	2.155	24.6	17.9	152.7	160.8	-0.392	-0.669	0.051	-0.336
05/08/2013 21:00	05/09/2013 21:00	97.1	1.612	0.626	2.0	11.8	3.015	2.155	24.6	17.9	152.7	160.8	-0.346	-0.361	-0.598	-0.435
05/12/2013 06:00	05/13/2013 06:00	78.2	1.104	0.391	4.9	19.4	3.015	2.155	24.6	17.9	152.7	160.8	-0.464	-0.705	-0.018	-0.396

06/10/2013 12:00	06/11/2013 12:00	83.0	1.688	0.524	-5.1	12.6	2.355	2.714	18.0	29.0	106.5	177.6	-0.132	-0.053	-0.007	-0.064
06/12/2013 09:00	06/13/2013 09:00	67.8	1.216	0.345	-6.4	12.7	2.355	2.714	18.0	29.0	106.5	177.6	-0.218	-0.293	0.038	-0.158
06/13/2013 18:00	06/14/2013 18:00	57.4	1.260	0.321	0.7	10.0	2.355	2.714	18.0	29.0	106.5	177.6	-0.277	-0.285	-0.248	-0.270
06/16/2013 00:00	06/17/2013 00:00	53.6	1.209	0.356	2.5	7.9	2.355	2.714	18.0	29.0	106.5	177.6	-0.298	-0.291	-0.262	-0.284
06/25/2013 21:00	06/26/2013 21:00	75.0	1.052	0.445	-10.1	14.7	2.355	2.714	18.0	29.0	106.5	177.6	-0.177	-0.316	0.237	-0.086
07/02/2013 12:00	07/03/2013 12:00	68.8	1.178	0.412	-6.2	12.0	2.046	2.760	19.0	23.4	106.0	209.0	-0.178	-0.165	-0.034	-0.126
07/03/2013 15:00	07/04/2013 15:00	78.7	1.372	0.361	-0.8	12.7	2.046	2.760	19.0	23.4	106.0	209.0	-0.131	-0.113	-0.237	-0.160
07/16/2013 21:00	07/17/2013 21:00	78.1	1.236	0.517	-0.3	13.6	2.046	2.760	19.0	23.4	106.0	209.0	-0.134	-0.106	-0.217	-0.152
07/20/2013 09:00	07/21/2013 09:00	69.1	0.946	0.490	-4.3	10.2	2.046	2.760	19.0	23.4	106.0	209.0	-0.177	-0.221	-0.192	-0.197
07/21/2013 09:00	07/22/2013 09:00	98.8	1.321	0.614	0.5	13.3	2.046	2.760	19.0	23.4	106.0	209.0	-0.034	-0.040	-0.218	-0.098
10/05/2013 12:06	10/06/2013 12:06	35.1	0.230	0.309	-5.7	8.7	1.075	2.216	17.1	19.0	36.1	116.6	-0.008	-0.242	-0.141	-0.130
10/23/2013 15:06	10/24/2013 15:06	31.3	0.333	0.646	3.7	11.2	1.075	2.216	17.1	19.0	36.1	116.6	-0.041	-0.043	-0.117	-0.067
10/24/2013 21:06	10/25/2013 21:06	29.8	0.352	0.728	3.8	8.1	1.075	2.216	17.1	19.0	36.1	116.6	-0.054	0.002	-0.275	-0.109
11/18/2013 12:00	11/19/2013 12:00	28.7	0.332	0.671	0.3	10.0	1.728	1.768	18.5	14.8	63.0	93.7	-0.367	-0.410	-0.558	-0.445
11/20/2013 21:00	11/21/2013 21:00	26.7	0.268	0.627	0.9	11.4	1.728	1.768	18.5	14.8	63.0	93.7	-0.387	-0.471	-0.422	-0.427
11/22/2013 03:00	11/23/2013 03:00	27.0	0.275	0.725	3.5	9.8	1.728	1.768	18.5	14.8	63.0	93.7	-0.385	-0.412	-0.351	-0.382
12/02/2013 03:00	12/03/2013 03:00	22.6	0.376	0.905	-5.6	13.2	1.346	1.261	15.0	10.7	35.7	54.1	-0.242	-0.052	0.359	0.022
12/12/2013 12:00	12/13/2013 12:00	34.1	0.467	0.700	-0.5	14.2	1.346	1.261	15.0	10.7	35.7	54.1	-0.029	-0.142	-0.033	-0.068
12/21/2013 15:00	12/22/2013 15:00	18.7	0.306	0.570	-0.1	8.8	1.346	1.261	15.0	10.7	35.7	54.1	-0.314	-0.373	-0.570	-0.419
12/22/2013 15:00	12/23/2013 15:00	25.7	0.407	0.674	2.7	7.2	1.346	1.261	15.0	10.7	35.7	54.1	-0.185	-0.210	-0.478	-0.291
12/23/2013 15:00	12/24/2013 15:00	26.4	0.431	0.538	4.3	8.9	1.346	1.261	15.0	10.7	35.7	54.1	-0.171	-0.299	-0.174	-0.215
12/26/2013 15:00	12/27/2013 15:00	18.9	0.327	0.581	0.1	7.2	1.346	1.261	15.0	10.7	35.7	54.1	-0.310	-0.347	-0.720	-0.459
12/28/2013 06:00	12/29/2013 06:00	40.3	0.661	1.011	2.5	11.8	1.346	1.261	15.0	10.7	35.7	54.1	0.086	0.259	-0.059	0.095
01/16/2014 18:00	01/17/2014 18:00	33.6	0.654	0.761	-0.8	10.0	1.578	1.340	19.6	9.7	44.0	77.7	-0.133	-0.122	-0.900	-0.385
01/18/2014 06:00	01/19/2014 06:00	24.7	0.516	0.452	0.9	11.0	1.578	1.340	19.6	9.7	44.0	77.7	-0.248	-0.455	-0.791	-0.498
01/19/2014 06:00	01/20/2014 06:00	31.7	0.389	0.306	-0.6	14.6	1.578	1.340	19.6	9.7	44.0	77.7	-0.158	-0.659	-0.449	-0.422
01/31/2014 12:00	02/01/2014 12:00	36.2	0.670	0.616	0.8	12.4	1.578	1.340	19.6	9.7	44.0	77.7	-0.100	-0.218	-0.654	-0.324
02/04/2014 12:00	02/05/2014 12:00	27.9	0.704	0.679	5.9	13.9	1.604	2.286	18.9	27.5	47.6	130.2	-0.152	-0.097	0.034	-0.072
02/12/2014 18:00	02/13/2014 18:00	32.1	0.642	0.766	1.6	12.3	1.604	2.286	18.9	27.5	47.6	130.2	-0.120	-0.086	-0.183	-0.129
02/13/2014 18:00	02/14/2014 18:00	20.3	0.430	0.408	5.2	9.5	1.604	2.286	18.9	27.5	47.6	130.2	-0.210	-0.335	-0.150	-0.232
02/26/2014 03:00	02/27/2014 03:00	33.8	0.704	0.477	-3.8	12.6	1.604	2.286	18.9	27.5	47.6	130.2	-0.106	-0.185	-0.091	-0.127
03/07/2014 03:00	03/08/2014 03:00	39.8	0.524	0.364	-3.4	10.3	1.421	0.878	15.3	9.3	56.2	39.6	-0.414	-0.607	-0.173	-0.398
03/09/2014 00:00	03/10/2014 00:00	33.2	0.530	0.399	2.8	10.5	1.421	0.878	15.3	9.3	56.2	39.6	-0.580	-0.560	-0.217	-0.452
03/15/2014 09:00	03/16/2014 09:00	54.2	0.746	0.454	-3.2	11.7	1.421	0.878	15.3	9.3	56.2	39.6	-0.050	-0.252	-0.044	-0.115
03/16/2014 09:00	03/17/2014 09:00	39.8	0.434	0.209	0.2	12.9	1.421	0.878	15.3	9.3	56.2	39.6	-0.415	-0.886	-0.224	-0.508

03/24/2014 00:00	03/25/2014 00:00	51.6	0.671	0.411	0.3	16.5	1.421	0.878	15.3	9.3	56.2	39.6	-0.115	-0.386	0.169	-0.111
04/10/2014 06:00	04/11/2014 06:00	47.8	0.793	0.382	-1.8	12.6	1.942	2.123	19.3	21.3	82.2	113.8	-0.303	-0.361	-0.227	-0.297
04/27/2014 03:00	04/28/2014 03:00	61.7	0.829	0.427	-2.7	12.6	1.942	2.123	19.3	21.3	82.2	113.8	-0.180	-0.323	-0.190	-0.231
04/28/2014 21:00	04/29/2014 21:00	64.4	0.723	0.445	0.1	15.9	1.942	2.123	19.3	21.3	82.2	113.8	-0.157	-0.365	-0.156	-0.226
05/02/2014 18:00	05/03/2014 18:00	43.3	0.506	0.264	-0.2	18.4	1.692	1.501	16.8	12.9	75.3	94.6	-0.339	-0.614	0.145	-0.269
05/20/2014 18:00	05/21/2014 18:00	46.9	0.922	0.401	0.9	11.4	1.692	1.501	16.8	12.9	75.3	94.6	-0.300	-0.246	-0.354	-0.300
05/30/2014 21:00	05/31/2014 21:00	53.8	1.234	0.441	0.1	12.8	1.692	1.501	16.8	12.9	75.3	94.6	-0.228	-0.011	-0.305	-0.181
08/09/2014 09:00	08/10/2014 09:00	72.4	1.107	0.454	-0.5	14.6	1.870	2.078	19.5	20.6	80.7	122.8	-0.068	-0.149	-0.219	-0.145
08/14/2014 09:00	08/15/2014 09:00	71.9	0.886	0.488	-4.4	12.9	1.870	2.078	19.5	20.6	80.7	122.8	-0.071	-0.239	-0.112	-0.141
08/15/2014 21:00	08/16/2014 21:00	50.8	0.657	0.394	-4.7	10.8	1.870	2.078	19.5	20.6	80.7	122.8	-0.244	-0.394	-0.195	-0.278
08/17/2014 15:00	08/18/2014 15:00	65.0	1.033	0.474	4.2	17.5	1.870	2.078	19.5	20.6	80.7	122.8	-0.128	-0.175	0.104	-0.066
08/24/2014 12:00	08/25/2014 12:00	50.5	0.674	0.390	-1.3	13.3	1.870	2.078	19.5	20.6	80.7	122.8	-0.246	-0.388	-0.235	-0.290
08/25/2014 15:00	08/26/2014 15:00	61.7	0.939	0.627	-0.7	12.0	1.870	2.078	19.5	20.6	80.7	122.8	-0.155	-0.146	-0.333	-0.211
09/07/2014 06:00	09/08/2014 06:00	52.4	0.942	0.499	1.8	13.7	2.174	1.487	21.3	10.4	86.7	102.0	-0.337	-0.493	-0.561	-0.464
09/15/2014 03:00	09/16/2014 03:00	31.2	0.667	0.313	-2.6	12.7	2.174	1.487	21.3	10.4	86.7	102.0	-0.545	-0.803	-0.576	-0.641
09/20/2014 21:00	09/21/2014 21:00	64.5	1.126	0.731	0.9	14.0	2.174	1.487	21.3	10.4	86.7	102.0	-0.218	-0.213	-0.613	-0.348
10/03/2014 03:00	10/04/2014 03:00	70.0	1.255	0.792	-3.1	11.7	2.441	1.416	22.1	14.7	94.9	98.8	-0.252	-0.278	-0.498	-0.343
10/04/2014 15:00	10/05/2014 15:00	44.2	1.086	1.005	6.2	10.8	2.441	1.416	22.1	14.7	94.9	98.8	-0.513	-0.247	-0.347	-0.369
10/07/2014 06:00	10/08/2014 06:00	39.4	0.755	0.567	-1.0	13.4	2.441	1.416	22.1	14.7	94.9	98.8	-0.562	-0.790	-0.527	-0.627
10/11/2014 15:00	10/12/2014 15:00	79.3	1.091	0.697	-3.0	12.6	2.441	1.416	22.1	14.7	94.9	98.8	-0.158	-0.461	-0.442	-0.354
03/09/2015 06:00	03/10/2015 06:00	40.9	0.578	0.800	0.9	15.5	2.757	3.028	19.4	41.6	106.6	130.0	-0.505	-0.455	-0.074	-0.345
03/10/2015 12:00	03/11/2015 12:00	66.2	0.892	1.059	6.7	10.7	2.757	3.028	19.4	41.6	106.6	130.0	-0.311	-0.266	-0.049	-0.208
03/12/2015 12:00	03/13/2015 12:00	69.3	0.871	0.863	-0.3	14.6	2.757	3.028	19.4	41.6	106.6	130.0	-0.287	-0.338	-0.109	-0.245
04/25/2015 00:00	04/26/2015 00:00	43.6	0.524	0.169	-0.2	10.4	1.780	2.333	21.7	22.1	79.9	135.5	-0.268	-0.466	-0.504	-0.413
04/26/2015 03:00	04/27/2015 03:00	52.4	0.787	0.316	5.1	9.3	1.780	2.333	21.7	22.1	79.9	135.5	-0.203	-0.290	-0.331	-0.275
04/30/2015 03:00	05/01/2015 03:00	67.1	1.328	0.463	3.7	12.0	1.780	2.333	21.7	22.1	79.9	135.5	-0.095	0.005	-0.277	-0.122
05/07/2015 00:00	05/08/2015 00:00	47.9	1.424	0.372	-6.5	14.4	2.107	2.109	17.3	17.6	77.8	128.1	-0.234	-0.147	0.205	-0.059
05/21/2015 18:00	05/22/2015 18:00	62.4	1.356	0.316	-6.6	9.5	2.107	2.109	17.3	17.6	77.8	128.1	-0.121	-0.206	-0.067	-0.131
05/22/2015 18:00	05/23/2015 18:00	56.5	1.119	0.279	-0.9	9.1	2.107	2.109	17.3	17.6	77.8	128.1	-0.167	-0.336	-0.415	-0.306
05/25/2015 00:00	05/26/2015 00:00	57.4	0.965	0.221	3.3	10.0	2.107	2.109	17.3	17.6	77.8	128.1	-0.159	-0.437	-0.227	-0.274
05/30/2015 15:00	05/31/2015 15:00	75.9	1.471	0.417	3.1	15.0	2.107	2.109	17.3	17.6	77.8	128.1	-0.015	-0.104	0.043	-0.025
06/02/2015 03:00	06/03/2015 03:00	50.4	1.164	0.220	1.1	12.6	1.977	2.728	23.0	39.6	73.1	162.2	-0.140	-0.217	-0.236	-0.198
06/03/2015 15:00	06/04/2015 15:00	54.0	0.804	0.172	0.7	10.6	1.977	2.728	23.0	39.6	73.1	162.2	-0.118	-0.367	-0.297	-0.261
06/04/2015 21:00	06/05/2015 21:00	51.2	0.915	0.180	3.0	12.4	1.977	2.728	23.0	39.6	73.1	162.2	-0.135	-0.323	-0.192	-0.217
06/19/2015 15:00	06/20/2015 15:00	50.3	1.299	0.407	-11.0	10.0	1.977	2.728	23.0	39.6	73.1	162.2	-0.140	-0.099	-0.051	-0.097

06/20/2015 15:00	06/21/2015 15:00	55.8	1.009	0.411	-1.9	12.9	1.977	2.728	23.0	39.6	73.1	162.2	-0.107	-0.204	-0.209	-0.173
07/02/2015 03:00	07/03/2015 03:00	71.1	1.045	0.358	-12.8	12.0	2.225	1.827	23.9	18.2	98.6	119.8	-0.229	-0.450	0.048	-0.210
07/03/2015 03:00	07/04/2015 03:00	62.7	1.078	0.283	-3.1	12.6	2.225	1.827	23.9	18.2	98.6	119.8	-0.300	-0.473	-0.455	-0.409
07/19/2015 06:00	07/20/2015 06:00	63.1	1.171	0.497	0.6	10.5	2.225	1.827	23.9	18.2	98.6	119.8	-0.296	-0.305	-0.705	-0.435
08/14/2015 00:00	08/15/2015 00:00	63.1	1.399	0.463	-2.6	19.3	2.794	3.047	25.9	31.2	149.0	176.5	-0.487	-0.306	-0.127	-0.307
08/30/2015 00:00	08/31/2015 00:00	78.3	1.092	0.726	-12.2	13.8	2.794	3.047	25.9	31.2	149.0	176.5	-0.401	-0.320	0.003	-0.239
08/31/2015 06:00	09/01/2015 06:00	84.7	1.207	0.730	-6.0	13.6	2.794	3.047	25.9	31.2	149.0	176.5	-0.365	-0.281	-0.200	-0.282
08/31/2015 12:00	09/01/2015 12:00	99.2	1.367	0.828	-4.8	14.9	2.794	3.047	25.9	31.2	149.0	176.5	-0.282	-0.197	-0.197	-0.225
09/01/2015 15:00	09/02/2015 15:00	75.5	1.089	0.681	-1.7	17.0	2.361	2.499	23.6	27.9	99.5	161.4	-0.149	-0.236	-0.173	-0.186
09/25/2015 15:00	09/26/2015 15:00	38.2	0.792	0.771	-5.1	17.3	2.361	2.499	23.6	27.9	99.5	161.4	-0.380	-0.319	-0.044	-0.248
09/26/2015 15:00	09/27/2015 15:00	74.6	1.163	1.018	-1.2	11.3	2.361	2.499	23.6	27.9	99.5	161.4	-0.154	-0.072	-0.398	-0.208
09/27/2015 15:00	09/28/2015 15:00	34.9	0.801	0.714	-0.8	10.4	2.361	2.499	23.6	27.9	99.5	161.4	-0.400	-0.339	-0.443	-0.394
09/29/2015 12:00	09/30/2015 12:00	33.7	0.439	0.547	0.5	9.9	2.361	2.499	23.6	27.9	99.5	161.4	-0.408	-0.550	-0.472	-0.477
10/19/2015 03:00	10/20/2015 03:00	59.3	0.669	0.860	-4.5	14.1	2.604	2.530	21.0	25.9	109.7	170.9	-0.295	-0.425	-0.093	-0.271
10/26/2015 00:00	10/27/2015 00:00	27.2	0.404	0.633	5.6	12.9	2.604	2.530	21.0	25.9	109.7	170.9	-0.483	-0.619	-0.093	-0.398
10/27/2015 00:00	10/28/2015 00:00	72.4	0.831	1.109	4.7	11.8	2.604	2.530	21.0	25.9	109.7	170.9	-0.218	-0.262	-0.171	-0.217
10/28/2015 00:00	10/29/2015 00:00	29.4	0.355	0.691	12.6	16.5	2.604	2.530	21.0	25.9	109.7	170.9	-0.470	-0.616	0.317	-0.256
11/21/2015 06:00	11/22/2015 06:00	38.4	0.623	1.313	-6.3	9.6	2.020	2.448	16.1	25.9	57.5	163.8	-0.117	-0.034	-0.006	-0.053
11/22/2015 06:00	11/23/2015 06:00	36.9	0.478	1.131	-3.6	8.4	2.020	2.448	16.1	25.9	57.5	163.8	-0.126	-0.168	-0.158	-0.151